November 2016

A Quantitative Measurement of Structural changes of RNA kissing complexes using Fluorescence Resonance Energy Transfer

Sheema Rahmanseresht
University of Massachusetts Amherst

A QUANTITATIVE MEASUREMENT OF STRUCTURAL CHANGES OF RNA KISSING COMPLEXES USING FLUORESCENCE RESONANCE ENERGY TRANSFER

A Dissertation Presented

by

SHEEMA RAHMANSERESHT

Submitted to the Graduate School of the
University of Massachusetts Amherst in partial fulfillment
of the requirements for the degree of

DOCTOR OF PHILOSOPHY

September 2016

Physics

A QUANTITATIVE MEASUREMENT OF STRUCTURAL CHANGES OF RNA KISSING COMPLEXES USING FLUORESCENCE RESONANCE ENERGY TRANSFER

A Dissertation Presented

by

SHEEMA RAHMANSERESHT

Approved as to style and content by:

Lori Goldner, Chair

Jennifer Ross, Member

Adrain Parsegian, Member

Craig T Martin, Member

Rory Miskimen, Department Chair
Physics

To my Loving Mom and Dad
inspiring brother Raed
and
my best friend and love Soroush

ACKNOWLEDGMENTS

I would like to thank my advisor Prof. Lori Goldner for her continuous support of my research, and for her motivation and knowledge. I would also like to thank the rest of my thesis committee: Prof. Craig Martin, Prof. Adrian Parsegian and Dr. Jennifer Ross, for their insightful comments and encouragement.

I would like to express my very sincere gratitude to Prof. Carlo Dallapiccola for his unconditional support and Dr. Jennifer Ross and Dr. Maria Kilfoil for their support to make this thesis possible. Special thanks to Dr. Juan Daniel Diaz-Valencia, Dr. Leslie Conway and Dr. Megan Bailey from Ross Lab.

I would like to express my deepest sense of gratitude to my friend and Colleague Dr. Peker Milas for all his help and encouragement. I would like to thank my colleagues at Goldner lab and all my wonderful friends for their absolute support to this thesis.

A special thanks to my amazing family: my mother and father for their support during my education and the sacrifices they made on my behalf, my brother for his infinite kindness and support, and my love and best friend, Soroush, for always standing by my side and believing in me.

ABSTRACT

A QUANTITATIVE MEASUREMENT OF STRUCTURAL CHANGES OF RNA KISSING COMPLEXES USING FLUORESCENCE RESONANCE ENERGY TRANSFER

SEPTEMBER 2016

SHEEMA RAHMANSERESHT

Ph.D., UNIVERSITY OF MASSACHUSETTS AMHERST

Directed by: Professor Lori Goldner

Many RNA interactions in cells occur in the form of loop-loop interactions, also known as a "kissing complex". In the bacterial and viral systems discussed here, there are transiently bound proteins involved that modulate the function of kissing complex. These proteins either stabilize the kissing complex or facilitate its conversion to extended duplex. I studied R1inv-R2inv kissing complex (KC), derivatived from RNAI-RNAII complex of *E.Coli*. Rop protein is known to stabilize the bent R1inv-R2inv KC against dissociation. The goal was to study structural change of this kissing complex after binding of the stabilizing Rop protein.

In this work for the first time I used the orientation sensitivity of Fluorescence Resonance energy transfer (FRET) to measure an angular change in the structure of R1inv-R2inv kissing complex upon binding of Rop protein. Single-molecular-pair-FRET (spFRET) is often used to study distance fluctuations of single molecules, it is harder to capture angular changes using FRET, because rotational motion of the dyes tends to wash out the angular sensitivity.

The effect of Rop protein on the conformation of the kissing complex is not known. Using fluorescence microscopy techniques we observe a change in twist angle of the KC with protein binding. The eight minimized energy structures reported for R1inv-R2inv KC show a small difference in end-to-end distance and a larger difference in twist and bend angles. From MD simulations I modeled FRET for these eight structures, also for these structures with addition of twist. By comparing the spFRET data with results of this first-principle model, I found the result is consistent with a -25° change in twist angle.

My preliminary work on another kissing complex, Dimerization initiation site (DIS) of HIV-1 retrovirus, is also discussed. Nucleocapsid protein (NCp7) plays an important role in facilitating the kissing complex to extended duplex transition for DIS. My work on DIS kissing complex, was aimed at studying possible intermediates in kissing complex to duplex transition, and investigating the effect of proteins like Rop and NCp7. The construction of the TIRF-FRET instrument, methods for surface passivation, and the RNA sequence design are discussed.

TABLE OF CONTENTS

LIST OF TABLES

Table **Page**

LIST OF FIGURES

Figure **Page**

INTRODUCTION

RNA loop-loop interactions, known as kissing interactions are ubiquitous in biological processes. In these interactions two stem-loops which are complementary in their loop form Watson-Crick base pairs. Kissing interactions are common in prokaryotic cells in the form of antisense-sense interactions [89]; these often have a regulatory function. Small non-coding RNAs in eukaryotes also often have a regulatory function [8]. For example, complementary small RNAs known as microRNA (miRNA) interfere with protein expression by binding to target mRNA transcripts [46, 16]; it is also reported that recognition of microRNAs and their target can be mediated by kissing interactions [18]. Another example of kissing complexes is in the dimerization initiation site (DIS) of HIV-1 genome which is responsible for encapsidation of genome. A similar DIS is seen in other retroviruses such as HIV-2, MuLV, HFV, BLV [17].

Loop-loop interactions are part of a larger class of RNA interactions referred to as "Antisense" because they involve complementary strands (sense and antisense) binding. Antisense RNA refers to a short (65-110 nt), untranslated transcript which can bind to the complementary regions on the sense RNA and control its biology [30]. These small RNAs commonly have one or more stem-loops, and the sense RNA usually has complementary stem-loops. The loops, which are usually 5-8 nucleotide long, are the initial RNA recognition sites. Kinetic studies on many antisense- sense RNA complexes gives an association rate of about 10^6 $M^{-1}s^{-1}$, independent of sequence. Dissociation rate of these complexes depends on the loop sequence suggesting the importance of base stacking. Stems do not have an effect on the association rate of hairpins, but they are important to the stability of the complex. The model proposed for high stability of kissing complexes considers Watson-Crick base paring

between complementary nucleotides of the loop region in stem-loop RNAs and their further rearrangement to stacking between stem helices, as the main reason for high stability. The overall structure resembles an A-form double-stranded RNA [30]. In this work two important examples of kissing interactions will be studied: (I) R1inv-R2inv kissing complex (KC) derived from RNA I-RNA II complex in *E. coli* which is important in control of replication of ColE1 plasmid [64] and is the longest known naturally occurring antisense RNA, and (II) loop-loop interaction in Dimerization Initiation Site (DIS) in the HIV-1 retrovirus which initiates dimerization of genomic RNA [90]. In both complexes transiently bound proteins are involved in modulating the structure and function of the RNA. Stability and flexibility of the initial loop-loop "kissing" complex, and structural transformations that often ensue from this intermediate state, modulate the function of RNA.

The challenge is to identify and control the underlying physical principles that guide RNA function. The aim of this work is to use single-molecule FRET (Fluorescence Resonance Energy Transfer), time-resolved fluorescence lifetime measurement, and other fluorescent techniques such as FCS (Fluorescent Correlation Spectroscopy), to study conformation of these kissing complexes before, during and after binding of proteins. This will give a better insight into the relationship between conformation and function of kissing complexes. For R1inv-R2inv KC, our specific aim is to understand effect of protein binding on the structure of the KC.

Chapters 1-4 include my work on R1inv-R2inv kissing complex system, and its conformational change upon binding of Rop protein. Chapter 1 provides a summary of the work done by other researchers on R1inv-R2inv KC. Using a dye labeling scheme that minimizes the rotational motion of the dyes with respect to the RNA, I use spFRET to measure an angular change in structure of RNA KC upon protein binding. Chapter 2 introduces different fluorescence techniques we used to study this system. In chapter 3, the results of the measurements are discussed. Finally,

in chapter 4 the result of modeling FRET from Molecular Dynamics simulation is discussed.

Chapters 5, 6 and 7 includes my preliminary work on the DIS KC dynamics project. These chapters summarize my setup of TIRF-FRET microscope, preparation of DIS samples and sample chamber, and passivation of the surface. Images and movies of DIS KC labeled with Cy3B and Cy5 were taken to evaluate the performance of the setup and efficiency of the samples. I also discuss the problems with our measurements and make suggestions for modifying the system.

PART 1: R1INV-R2INV KISSING COMPLEX

CHAPTER 1

BACKGROUND: R1INV-R2INV COMPLEX

In *E. coli*, replication of ColE1 plasmid requires an RNA primer (RNA II) whose function is modified by interaction with an antisense strand (RNAI) that is also encoded by the plasmid. Binding of antisense RNAI to RNAII prevents it from forming the complex required for its hybridization with the template DNA [64]. Secondary structure of RNA I-RNA II complex [32] is shown in Fig. 1.1(b), and secondary structure of complete RNA II is shown in Fig. 1.1(a) [94]. The color code on stem-loops of RNA II (Fig. 1.1(b)) is analogous to the color code shown in Fig. 1.1(a). Stability of this complex and therefore the function of primer is modulated by protein binding. Rop (RNA one repressor) also known as Rom (RNA one modulator) [7] is a plasmid encoded protein which binds to the kissing complex and decreases its equilibrium dissociation constant. Rop acts to suppress replication of the plasmid by stabilizing the intermediate RNA I-RNA II complex [33].

The model system often used in the study of this kissing complex is a short derivative (RI- I_{18} and RII- I_{18} with 18 nucleotides) of a single stem-loop (RI-I and RII-I) of the RNAI-RNAII antisense complex (Fig. 1.1 (c)). Stability of complex has been studied using stem-loop pairs with different size loops, loop complemetarity and stem sequence. Loop complementarity, loop closing base pair at position one and seven of the loop, sequence of the first base pair in the stem adjacent to the loop, and orientation of the loop highly affects kissing complex stability [33, 43]. The dissociation constant for a complex with only five complementary bases in the loop is 100-fold larger than fully complementary loop sequences; furthermore a complex with only

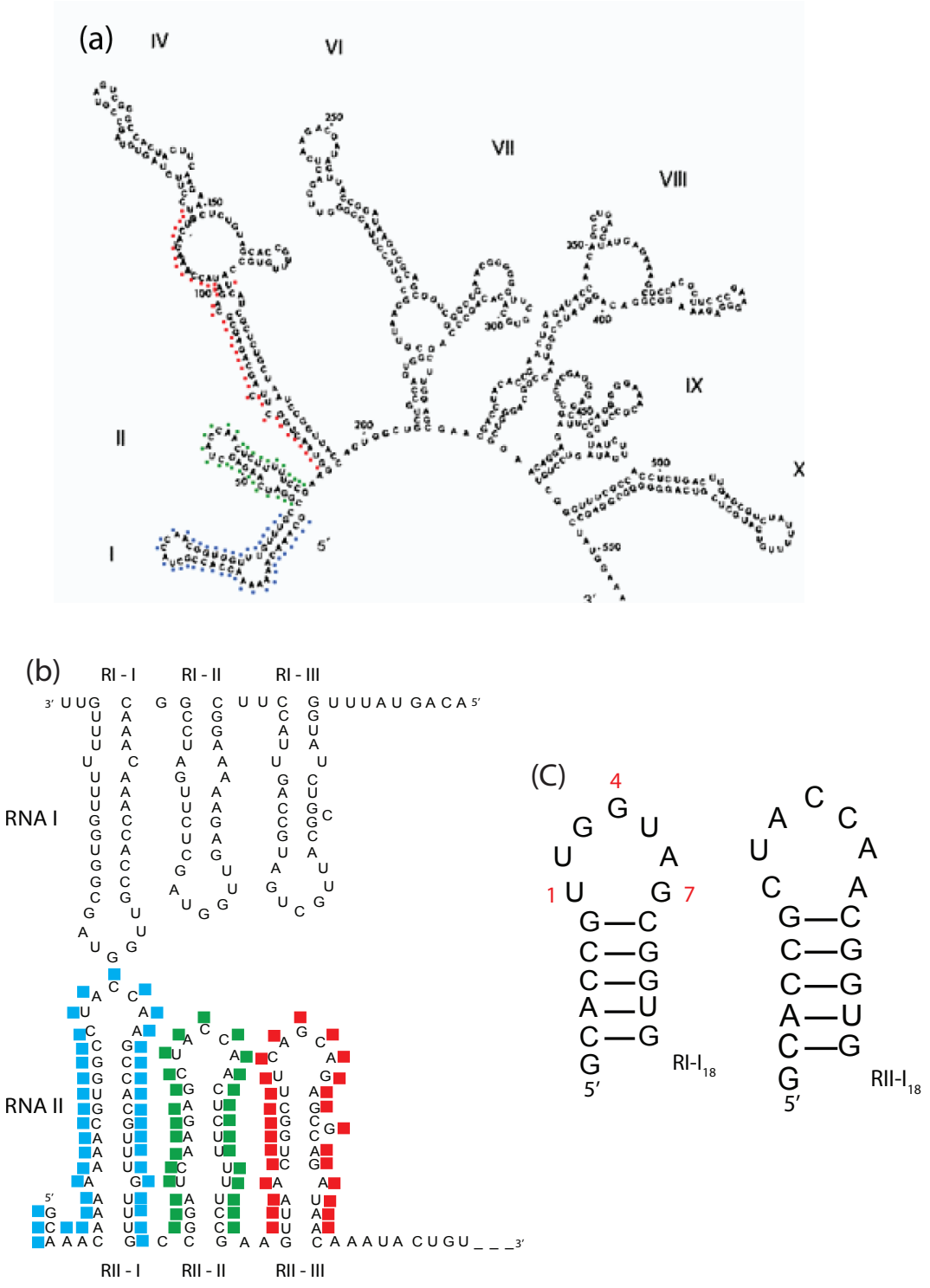

Figure 1.1. (a) Secondary structure of complete RNA II [94]. (b) Secondary structure of RNA I-RNA II complex [32]. The color code on RNAII in part b corresponds to the same sequence in part a. (c) RI- I_{18} and RII- I_{18} with 18 nucleotides are short derivative of RI-I and RII-I stem-loops from RNAI-RNAII. Loop closing base pairs (positions 1 and 7) are important in stability of complex.

three complementary bases is unstable. Inverting the loop of wild type RNA hairpins $5'$ to $3'$ significantly improves the stability of kissing complex without changing equilibrium constant for Rop binding, this complex has a dissociation constant of 0.6 nM which is 10000 times smaller than wild type [43, 31]; this enhanced stability is convenient in structural studies [43, 61, 59]. These inverted loop structures are called R1inv and R2inv (Fig. 1.2(a)). Structural studies of R1inv-R2inv kissing complex using NMR, shows all seven bases in the loop participate in Watson-Crick base pairing and they are continuously stacked on the $3'$ side of respective stem helices. From the local constraints provided by NMR, eight minimized energy R1inv-R2inv structures (Fig.1.2(b)) were identified; these structures are bent at the loop-loop junction with bend angles ranging from 49° to 96°. The average structure has a bend angle of approximately 80° [59]; its tertiary structure along with the curvilinear helical axis is shown in Fig. 1.2(c). The bend in structure can facilitate stem exchange and extended duplex formation by putting the stems in closer vicinity. Rist and Marino [83] propose a two step mechanism for formation of kissing complex. First, a loop-loop helix is formed by Watson-Crick base pairing between the two complementary loops. Second, the formed complex rearranges until the loop-loop helix is stacked between the two stem helices.

Rop is a homodimer of 63 residues [6] forming a four-helix bundle, Fig. 1.2(d): it binds at the loop-loop junction to complexes with 6, 7, or 8 nucleotides in their loops, [79] but does not bind linear duplex RNA or RNA hairpins [43, 31]. The binding site of Rop protein is identified using mutational analysis and NMR [92, 23]. It is known that residues Lys3, Asn10, Phe14, Gln18, and Lys25 which are located on helix I and I$'$ of the protein are the main residues contributing to binding. Phe14 is identified as the key element in binding and it is proposed that this residue stacks on RNA bases of the kissing complex or intercalates between them [79, 19]. Crystal structure for Rop protein shows Phe14 and Phe14$'$ residues on the helices to be

partially stacked; this suggests formation of a hydrophobic surface with a specific geometry that complements the protein binding site on R1inv-R2inv kissing complex [92]. The bend angle of the kissing complex was thought to play a role in Rop binding. However, the effect of Rop binding on the global structure of a bound complex has previously been observed only indirectly, through circular permutation assays [101] that rely on the different gel mobilities of bent RNA. The result of these assays appeared consistent with an increase in the bend angle of the kissing complex upon Rop binding from 45° to 60°[61].

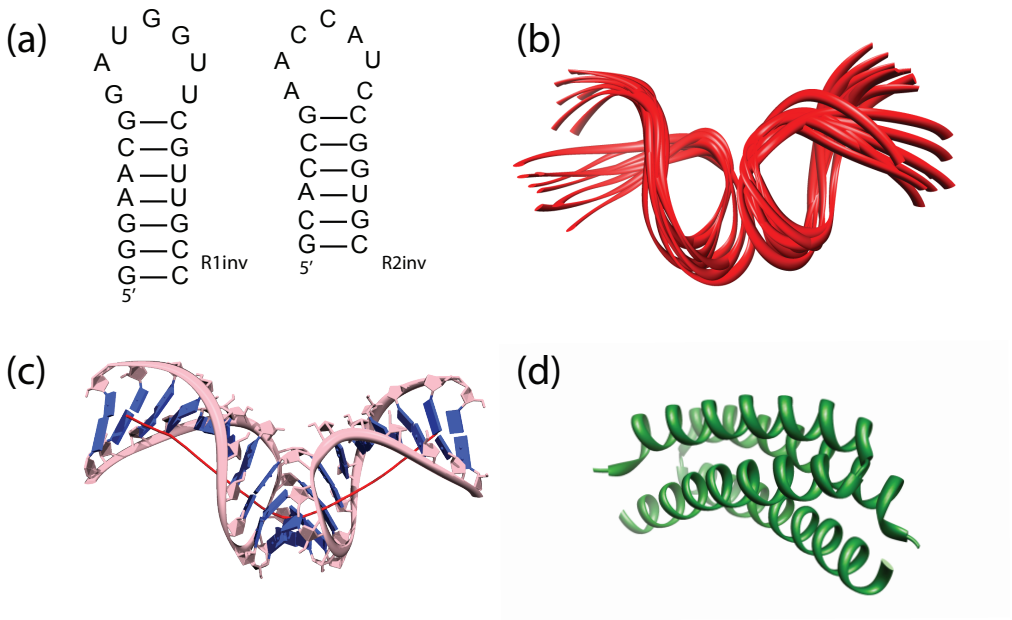

Figure 1.2. (a) Secondary structure for R1inv and R2inv. For the R1inv-R2inv-C structure the terminal base pairs were swapped so that there is a 5′ terminal C, instead of a 5′ terminal G, on each hairpin. (b) Tertiary structure for the eight minimized-energy R1inv-R2inv complexes (PDB 1bj2) with bend angles ranging from 65° to 90° [59]. (c) Average structure for R1inv-R2inv (PDB 2bj2) with bend angle of 80° [59], helical axis obtained by Curves+ package [58] is shown with a red curved line.(d) Tertiary structure for Rop protein(PDB 2ijk) [7].

We use single-molecular-pair fluorescence resonance energy transfer (spFRET) to show that there is indeed a change in the structure of the R1inv-R2inv complex upon

Rop binding. Moreover, by using time-resolved lifetime measurements and sensitivity of Cyanine dyes to their environment, we have been able to seperate distance changes in structure from angular changes using FRET. Rather than a change in bend, we found that twist angle of R1inv-R2inv kissing complex plays an important role in binding of Rop protein. Presumably, Rop protein recognizes and stabilizes relatively untwisted complexes.

We base our conclusion on a direct model of FRET from each of the eight minimized energy states [59]. This model includes the full structural fluctuations of the dye on the RNA as predicted from MD simulations. The method used to calculate FRET from the MD trajectories is exact [14, 42, 48, 66]: There are no adjustable parameters and no assumptions made regarding the behavior of the dyes. In addition, the method we introduce for investigating the change in twist is generalizable to any change in structure, so long as a set of proposed or possible structures exist or can be generated. Here the eight minimized energy states [59] for unbound R1inv-R2inv as determined from the NMR constraints serve this purpose; these structures differ primarily in twist and bend angle.

CHAPTER 2

SINGLE MOLECULE FLUORESCENT TECHNIQUES

2.1 Förster Resonance Energy Transfer (FRET)

2.1.1 Theory of FRET

FRET is non-radiative transfer of energy from a donor fluorophore to an acceptor fluorophore. If we consider a weak Coulomb interaction between two particles, expansion of this energy gives terms resulting from charge-charge, charge-dipole, dipole-dipole and higher order quadrupole interactions. For particles with no net charge the charge-charge and charge-dipole terms can be ignored, and in our case the quadrupole terms, which are of much shorter range than considered her, will be ignored. The dipole-dipole interaction gives rise to Förster energy transfer. The potential decays as R^{-3} and depends on dipole orientations (Fig. 2.1(d)) [54]. Förster Energy Transfer is a photophysical phenomenon, Fig. 2.1(c) shows a simplified kinetic scheme for FRET. Donor molecule can be excited with the rate of k_{ex} to the first singlet state. The excited donor molecule can either decay radiatively with decay rate of k_D, or can transfer its energy to the acceptor molecule with a rate of k_{ET} [42]:

$$k_{ET} = k_D \, (\frac{R_F}{R})^6, \tag{2.1}$$

The effiecieny of this energy transfer decreases as the fluoropores become farther apart:

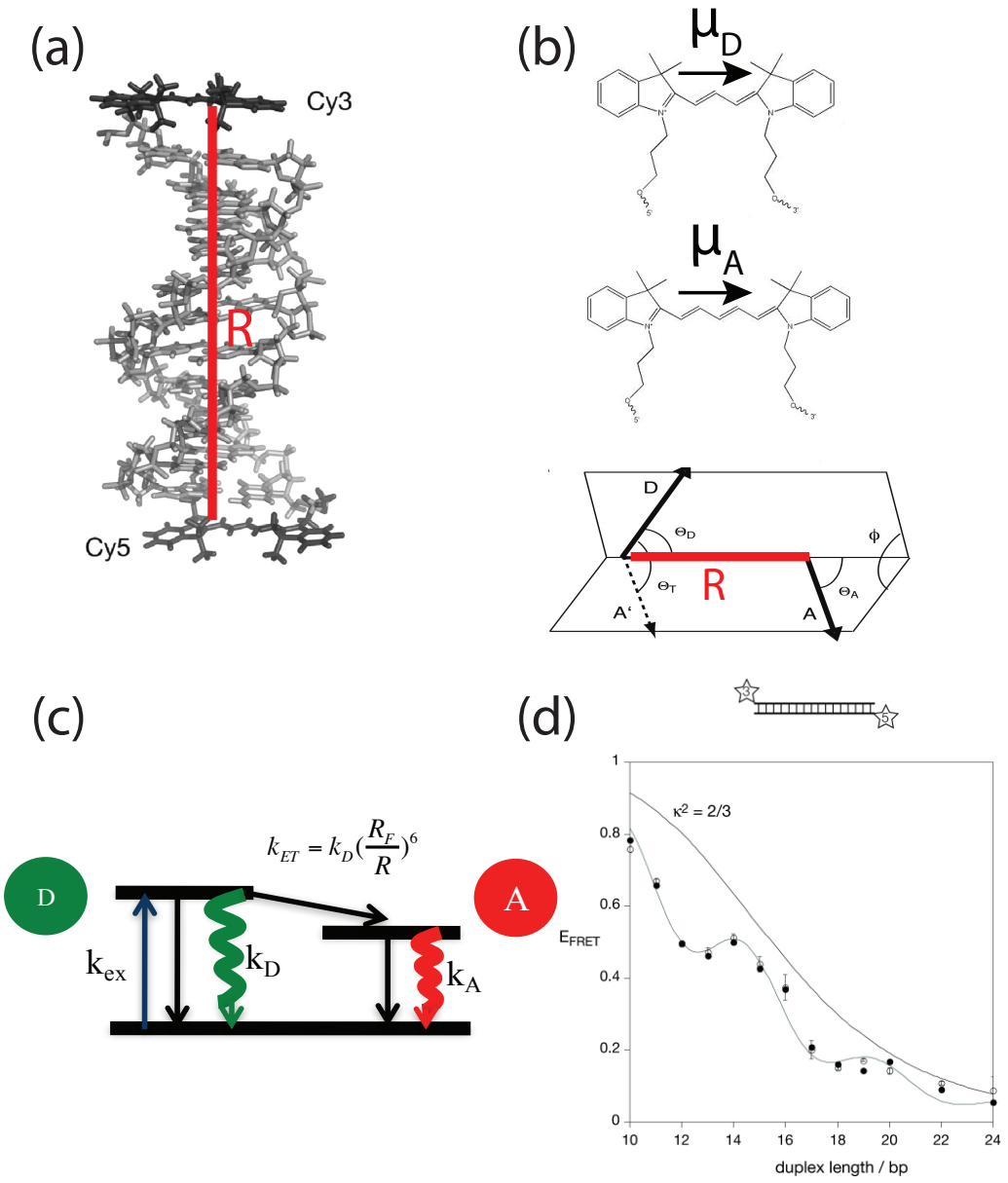

Figure 2.1. (a) double stranded DNA labeled with Cy3 and Cy5 (b) Orientation of the transition dipole moments for Cy3 (D) and Cy5 (A) are along the conjugated chains and are shown with black arrows. The end-to-end distance (R) is the line connecting the two dipoles. (c) Simplest kinetic scheme for FRET, k_{ex} is the excitation rate, k_{ET} is the rate of energy transfer and k_A and k_D are the donor and acceptor emission rates. (d) Dependence of FRET to the distance between the two dyes and relative orientation of dyes. In the extreme case were fluorophores are freely rotating (κ^2= 2/3) FRET decreases smoothly as a function of distance, when dyes are not freely rotating, there will be modulations in FRET as a function of distance [50].

$$E = \frac{1}{1 + (\frac{R}{R_F})^6}, \tag{2.2}$$

R is the distance between the two fluorescent dyes, and R_F is Förster radius which is a function of photophysical properties of dyes and their relative orientation. R_F is typically in the range of 2-9 nm and is defined as:

$$R_F = \frac{AJ\eta_D\kappa^2}{n^4}, \tag{2.3}$$

where J is the spectral overlap of donor emission and acceptor absorption, η_D is the quantum yield of donor in absence of acceptor, κ^2 is the relative orientation of the dyes, n is the refractive index of solvent and A is a constant. The relative orientation of the dyes (κ^2) is described by:

$$\kappa = (\hat{\mu}_1 \cdot \hat{\mu}_2) - 3(\hat{\mu}_1 \cdot \hat{R})(\hat{\mu}_2 \cdot \hat{R}), \tag{2.4}$$

where $\hat{\mu}_1$ and $\hat{\mu}_2$ are the dye transition dipoles and $\hat{R}$ is the displacement from donor dye to acceptor dye.

The spectral overlap, J(λ), is defined as:

$$J = \int_0^{+\infty} F_D(\lambda)\epsilon_A(\lambda)\lambda^4 \, d\lambda, \tag{2.5}$$

where $F_D(\lambda)$ is the normalized emission spectrum of donor molecule and $\epsilon_A(\lambda)$ is the extinction coefficient for acceptor molecule ($M^{-1}cm^{-1}$).

At the condition were the rotational diffusion of dyes happens in a timescale much faster than the lifetime of donor dye, and dyes can freely rotate, the mean value of $\langle\kappa^2\rangle = 2/3$ can be used. For convenience we define R_0 (Eq. 2.6) as the Förster radius calculated with $\kappa^2 = 2/3$. In fact free rotation is generally assumed in the literature

so most authors report on R_0. For Cy3-Cy5 pair R_0 is reported within the range of 5.6 - 6.5 nm in literature [74, 102, 71, 81]. Here I use R_0= 5.8 nm.

$$R_0 = \sqrt[6]{\frac{2}{3\kappa^2}}\, R_F \tag{2.6}$$

The largest problem in calculating FRET from Eq. 2.2 comes from κ^2. Fluorophores used as FRET pairs have different behavior depending on their chemical structure and the site of attachment [91, 76, 74], and this makes assumption of freely rotating dyes not always correct. Iqbal *et al.* [50] measured FRET for a duplex DNA (labeled with Cy3-Cy5 pair) with different lengths and observed modulations in FRET as a function of distance (Fig. 2.1). This is strong evidence that dyes are not freely rotating. Cyanine dyes spend a large fraction of their time stacked on the terminal base pairs, and therefore almost never in the limit of free rotation. In order to make accurate distance measurements using FRET, it is important to consider orientation dependency of FRET. More importantly, the dependency of FRET on κ^2 makes it a great tool not only to study distance changes in structure but also to study angular changes in structure.

2.1.2 Ratiometric FRET measurement technique for diffusing molecules

Single-molecule-sensitive FRET measurements were performed using a homebuilt confocal microscope with 514 nm excitation from an Argon-Krypton laser with 60 μW entering the scope. Emitted donor and acceptor photons were detected using two avalanche photodiodes (MPD τ-SPAD) and homemade photon timing circuitry based on an FPGA [40]. A schematic for the confocal FRET setup and a typical signal detected in donor and acceptor channels are shown in Fig. 2.2(a,b,c).

In single-molecule-sensitive solution FRET experiments, emitted photons from donor and acceptor fluorophores is detected and used for calculating FRET efficiency. The emitted photons arrive in short bursts with duration of 100-1000 μsec correspond-

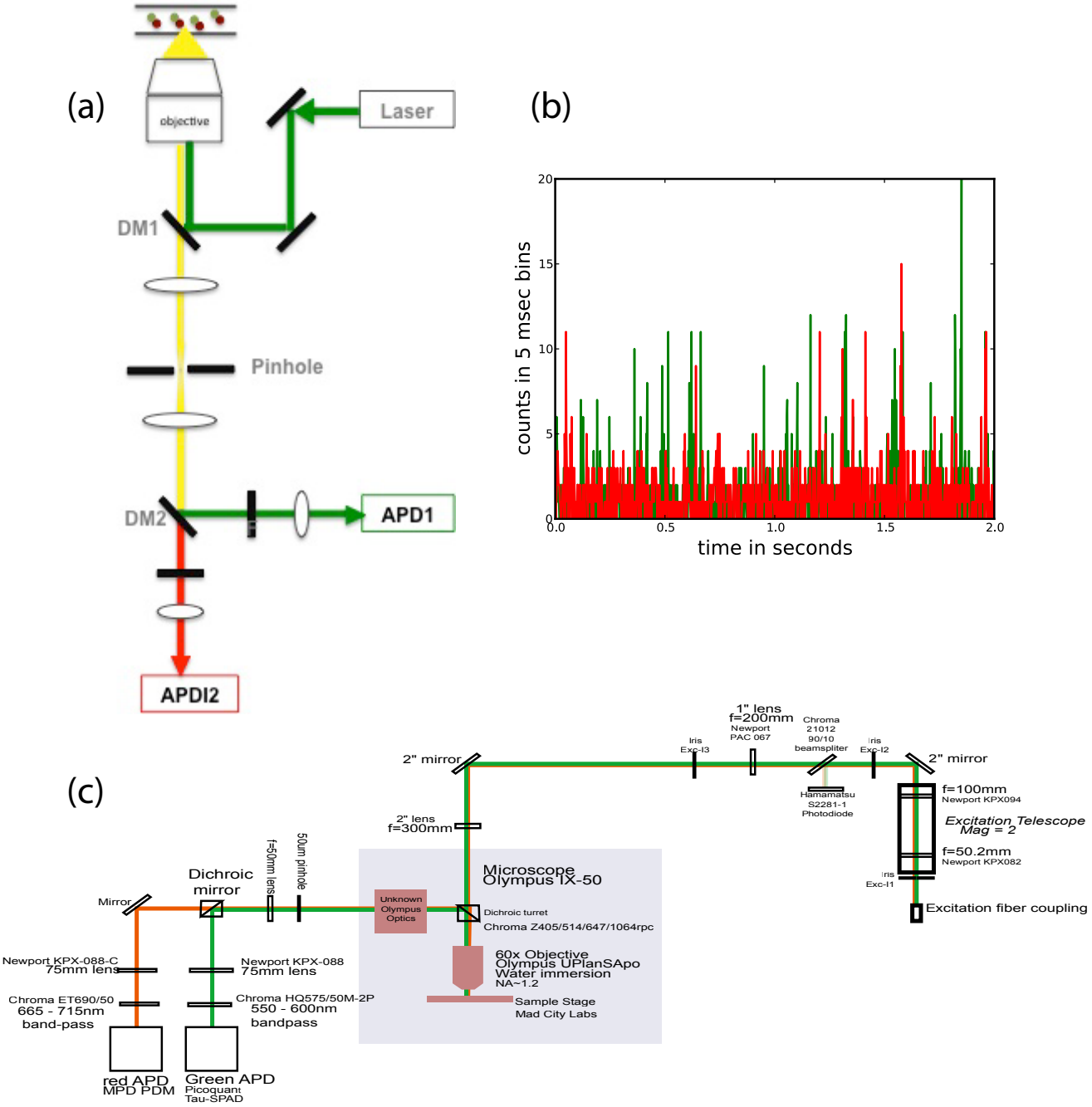

Figure 2.2. (a) Schematic for a confocal FRET setup. (b) Donor (green) and acceptor (red) time traces using 5 ms bins. (c) drawing for FRET setup as been used for ratiometric experiments.

ing to the time a molecule spends diffusing through the confocal detection region. To measure FRET, we bin photons in to 1-5 ms bins and calculate the proximity ratio (P). Many of these bins are noise originating from dark counts of detectors, or any background fluorescence in solution, therefore by applying a threshold (N_{th}) to the sum of acceptor and donor photons the number of these bins can be minimized. Finally proximity ratio (P), also known as apparent FRET efficiency, will be defined as the total number of acceptor photons divided by sum of donor and acceptor photons in each bin (Eq. 2.7).

$$P = \frac{N_a}{N_a + N_d} \tag{2.7}$$

where N_a (N_d) is the number of acceptor (donor) photons in 1- 5 ms bins. To observe the distribution of proximity ratios a histogram will be constructed. For the case were the interdye distance is fixed, we expect this histogram to have two peaks, each with a variance. The first peak with a low FRET value ≤ 0.2 is typically from leakage of donor emission in the acceptor channel. The second peak with higher FRET value is the FRET peak resulting from transfer of energy from the donor molecule to acceptor. The Poissonian nature of photon counts gives a variance [42]:

$${\sigma_s}^2 = \langle P \rangle \left(1 - \langle P \rangle\right) / \langle N_a + N_d \rangle. \tag{2.8}$$

However, the variance of each peak is often larger than that predicted by shot noise. This can be due to existence of a heterogeneous mixture of states with fluctuations faster than bin time but slower than the fluorescent lifetime, or conformational dynamics slower than the inter arrival time of photons. In the case that the molecule has more than one discrete conformational state that can interconvert in the timescale slower than the bin time, separate proximity ratio peaks will be observed. For a thorough understanding of single molecule FRET efficiency histograms, the book chapter by Gopich and Szabo is highly recommended [42].

In constructing the proximity histograms the peak due to donor-only labeled molecules can be removed from the histograms by assigning each data bin to a specific peak using Gibbs sampling. The mean value of the proximity ratio $\langle P \rangle$ and the standard deviation of the distribution σ_p are returned by a nonlinear least-squares fit of a Gaussian with two adjustable parameters to the proximity histograms.

The absolute value of FRET can be calculated by taking the correction factor γ in to account (Eq. 2.9). γ is the relative detection efficiency (χ) and quantum yield (η) of the acceptor and donor dyes, $\gamma = \frac{\eta_A \chi_A}{\eta_D \chi_D}$. Absolute FRET efficiency will be as Eq. 2.9:

$$E_{FRET} = \frac{N_a}{N_a + \gamma\ N_d}. \tag{2.9}$$

The average proximity ratio (P) is related to absolute FRET by [42]:

$$\langle E \rangle = \langle P \rangle / [\langle P \rangle + \gamma(1 - \langle P \rangle)]. \tag{2.10}$$

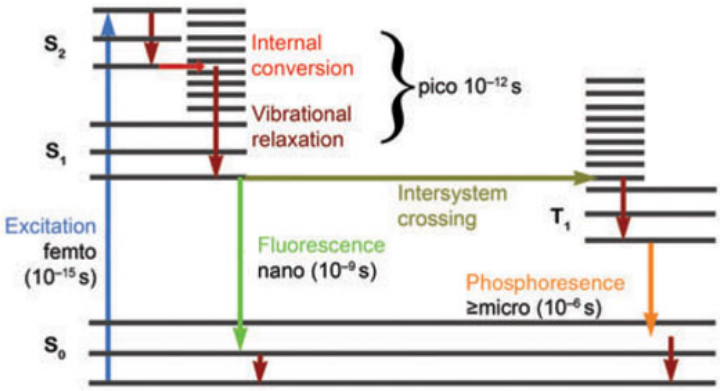

Figure 2.3. Jablonski diagram for a molecule from Ref. [60]. blue arrow shows excitation of molecule from ground state to excited states by absorption of a photon. Red arrows show relaxation through internal conversation, and vibrational relaxation. Green arrow shows relaxation to ground state through fluorescence by emitting a photon.

2.1.3 FRET efficiency using time-resolved fluorescence lifetime measurements

When a fluorophore is excited with light, several photophysical events may happen. As shown in the Jabloski diagram of Fig. 2.3, these photophysical processes include internal conversion, vibration relaxation, intersystem crossing and fluorescence which are each occurring with different rates [10]. One of the quantities that can be measured in time-resolved fluorescence measurements is fluorescence decay time (lifetime) which is basically the reciprocal of the fluorescent decay rate. Fluorescent lifetime is the average time it takes for a fluorophore to decay from its excited state to ground state (Eq. 2.11). Lifetime for organic dyes is in the order of 0.1-10 ns. The fluorescent lifetime τ is given by:

$$\langle \tau \rangle = \frac{1}{k_r + k_{nr}}. \tag{2.11}$$

Here k_r is the radiative decay rate and k_{nr} is the non-radiative decay rate. In the absence of any quenching process (k_{nr}=0), lifetime is called the intrinsic or natural lifetime (τ_0). Fluorescent lifetime is an intrinsic property of fluorphores, and depends on the local environment, refractive index, viscosity, pH and interactions with other molecules [15]. Fluorescent lifetimes can be used to measure FRET and it has the advantage of not needing γ. Förster resonance energy transfer (FRET) causes quenching of the donor molecule, therefore lifetime of donor molecule decreases due to this non-radiative process ($k_{nr} = k_{ET}$). FRET efficiency can be defined in terms of the fluorescent lifetime of donor fluorophore in absence and presence of acceptor fluorophore:

$$E = 1 - \frac{\tau_{DA}}{\tau_D}. \tag{2.12}$$

Fig. 2.4 shows a schematic of the experimental setup we used for data acquisition. Fluorescence lifetime decay of diffusing molecules through a femtoliter focal volume

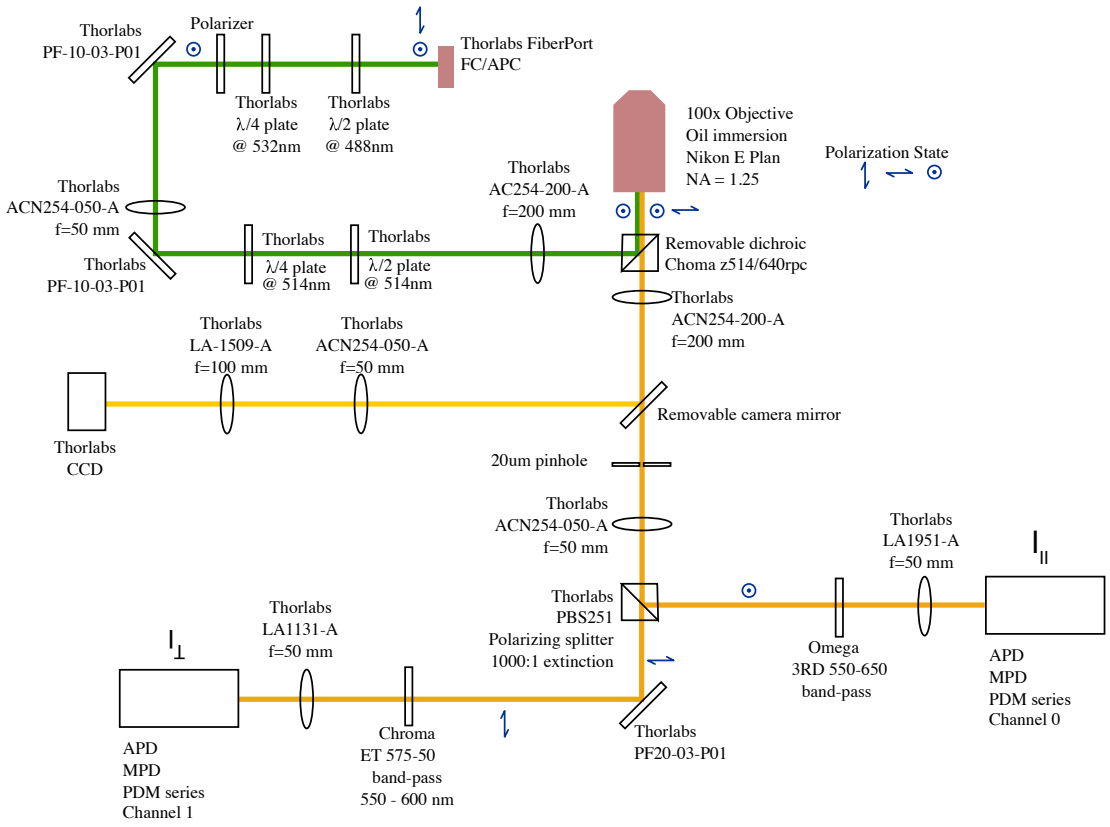

Figure 2.4. Time-resolved polarization anisotropy setup used for lifetime measurements. The first half waveplate and quarter weveplate after the fiber port are for controlling the power. The waveplates before objective are for setting the polarization to minimize the signal in the perpendicular channel. In the emission path the polarizing beam splitter seperates parallel and perpendicular components of emission light and they will be detected using two MPDs. When the emission light is polarized in either parallel or perpendicular direction, it has maximum counts in one channel with respect to the other.

was measured using time-resolved polarization anisotropy. Fluorescence sample was excited using an 80 MHz femtosecond Ti:Sapphire laser (Tsunami, Spectra physics) tuned to a center wavelength of 514 nm and power of 80 μW. Fluorescence photons were acquired in two polarization channels and denoted $I_{\parallel}$ and $I_{\perp}$ respectively. Fast avalanche photodiodes (MPD PDM series) with a timing accuracy of about 25 ps were used for photon detection along with time correlated single photon counting (TCSPC) electronics (Picoquant PicoHarp 300) with 4 ps resolution. TCSPC registers the arrival time of each photon, with respect to the excitation pulse arrival time [9, 96]. By collecting data over many cycles of excitation and emission a histogram of photon arrivals per time bin can be constructed which is representative of the time decay profile. This is only correct when not more than one photon is detected in each cycle. To satisfy this condition the photon count rates should be kept low, so that as a rule of thumb only one photon should be detected at every 20-100 cycles . For example for a 80 MHz repetition rate not more than 4×10^6 cps (counts per second) is expected. For a free fluorophore in solution with one fluorescence lifetime, the decay curves depend on both the fluorescence lifetime (τ), and rotational lifetime (θ) of the dye, and have a functional form [55, 75]:

$$I_{\parallel}(t) = A_{\parallel} exp\left(\frac{-t}{\tau}\right)(1 - r_i(t)) \tag{2.13a}$$

$$I_{\perp}(t) = A_{\perp} exp\left(\frac{-t}{\tau}\right)(1 + 2r_i(t))\,, \tag{2.13b}$$

where r(t) is the time dependent polarization anisotropy. For a simple spherical rotator: $r(t) = r_0\ exp\left(\frac{-t}{\theta}\right)$, where r_0 is the intrinsic anisotropy of the fluorophore. When the dye is attached to a larger, freely rotating molecule, polarization anisotropy will include the rotational lifetime of the large molecule (ϕ) and dye (θ) seperately: $r(t) = r_0\ \left[(1-C)exp\left(\frac{-t}{\theta}\right) + C\right] exp\left(\frac{-t}{\phi}\right)$ [10, 55]; C represents the degree of motional

restriction of the dye. For a fast fluctuating dye with no hinderance from the molecule it is attached to, C will be close to zero. While for a dye stacked on the molecule, C is expected to be close to 1.

Cyanine dyes are well known to have fluorescent lifetimes that depends on the rigidity of their environment [91, 76]. For Cy dyes on RNA, we consistently find three distinct rotational/fluorescence lifetime configurations [66]. We find that Cyanine dyes have multiple lifetimes tied to different rotational anisotropies. We expect short-lifetime components of the fluorescence to arise from relatively free and rapidly rotating dyes, whereas longer-lifetime components arise from dyes that are base-stacked. In a base-stacked configuration, Cyanine have longer lifetimes, while freely-rotating Cyanines have a significantly shorter lifetime. It is therefore possible to separate the rotational motion by fluorescent lifetime. Apart from the rotational lifetime of the fluorophores, there is a rotational lifetime (ϕ) associated with the overall tumbling of the RNA which is expected to be longer that rotational lifetime of dyes [10].

For donor-only data we propose the following model for the decay of the fluorescence intensity components parallel and perpendicular to the polarization of the incident beam:

$$I_{\parallel}(t) = B_1 \left[\sum_{i=1}^{3} F_{iD}\ exp\left(\frac{-t}{\tau_{iD}}\right)(1 + 2r_i(t)) \right] \tag{2.14a}$$

$$I_{\perp}(t) = \sum_{i=1}^{3} F_{iD}\ exp\left(\frac{-t}{\tau_{iD}}\right)(1 - r_i(t)) \tag{2.14b}$$

and the anisotropy for dyes attached to RNA is approximated as:

$$r_i(t) = \alpha \left[(1 - C_i) exp\left(\frac{-t}{\theta_i}\right) + C_i \right] exp\left(\frac{-t}{\phi}\right) \tag{2.15}$$

Here F_{iD}s are the intensity amplitudes, τ_{iD} and θ_i are the fluorescence and rotational lifetimes of dyes, ϕ is the rotational life time of RNA, α is the intrinsic anisotropy

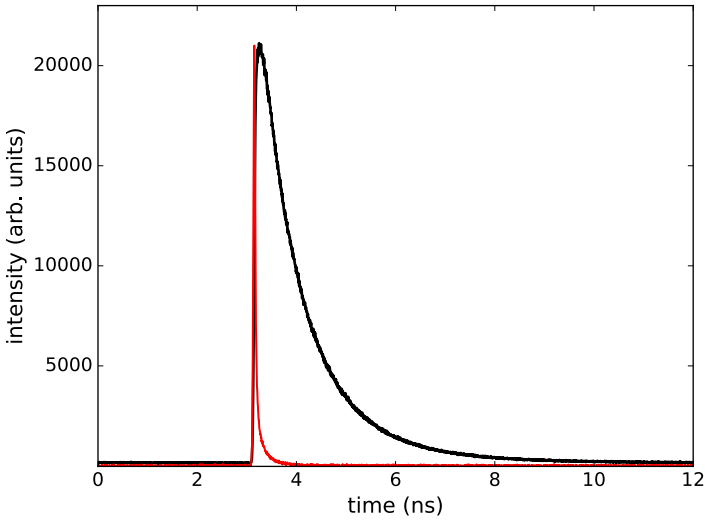

Figure 2.5. An example of instrument response function (Red), and fluorescent signal (Black).

of the fluorophore and is fixed to 0.38, and B_1 is a factor to account for differences in collection efficiency of the two channels and C_i describes the degree of motional restriction of the dye in state i. Therefore for the case were the dye rapidly rotates and doesn't experience any restriction from the RNA we would expect C_i to be zero. Note that F_{iD}s are the same for the parallel and perpendicular channels.

To find FRET from Eq. 2.12 we need to find the fluorescence lifetime of Cy3 (donor) dye in presence of Cy5 (acceptor) dye. For FRET data, the persistent presence of a donor-only population (due to acceptor bleaching and blinking) required that we also include the donor-only terms for each of the three rotational states:

$$I_{\parallel}(t) = B_2 \left[\sum_{i=1}^{3} \left(F_i exp\left[\frac{-t}{\tau_i}\right] + F_{iD} exp\left[\frac{-t}{\tau_{iD}}\right] \right) (1 + 2r_i(t)) \right] \tag{2.16a}$$

$$I_{\perp}(t) = \sum_{i=1}^{3} \left(F_i exp\left[\frac{-t}{\tau_i}\right] + F_{iD} exp\left[\frac{-t}{\tau_{iD}}\right] \right) (1 - r_i(t)) \tag{2.16b}$$

similarly, r(t) is approximated by Eq. 2.15. Here F_i and F_{iD} are FRET and donor-only amplitudes respectively, and τ_i's are the lifetimes associated with FRET from each dye configuration. The relative donor-only population of the three configurations is determined by a separate donor-only measurement, so there are only one additional parameter (F_{3D}) for the FRET data: $F_{1D} = \frac{p_1\tau_3}{p_3\tau_1} F_{3D}$ and $F_{2D} = \frac{p_2\tau_3}{p_3\tau_2} F_{3D}$. p_1, p_2 and p_3 are the donor populations and defined as $p_i = \frac{A_{iD}\tau_{iD}}{\sum_{j=1}^{3} A_{jD}\tau_{jD}}$. There are 8 fitting parameters in this fit, only τ_3 is globally fitted across all Rop concentrations. We don't expect the fluorescence lifetime of the donor-only population change in the FRET measurements, therefore τ_{iD}s are fixed to values given by the donor-only fit results. For FRET data we don't expect a change in θ_i, ϕ, and C_i for Cy3, so the values for these parameters are also fixed to donor-only fit results.

We find adequate fits with the above model and best-fit parameters that are consistent with our expectation that shorter fluorescence lifetimes are correlated with shorter rotational lifetimes. Conversely, extant models that assume a decoupling of the rotational and fluorescence lifetime fail to produce adequate fits.

The models for fluorescene decay curves were convolved with the IRFs (Eq. 2.17) and then fit to $I_{\parallel}$ and $I_{\perp}$ using a nonlinear least-squares fit. Instrument response function (IRF) is the distribution of photons from a non-fluorescent scattering sample excited by the pulsed laser light. In an ideal condition were the excitation pulse is infinitely sharp and detectors and electronics are infinitely accurate, IRF should have a delta function shape. In reality the timing uncertainty introduced by detectors and excitation source causes broadening of the IRF. Width of IRF can be measured experimentally by collecting data from a non-fluorescent medium which scatters some of the laser light. In this work, instrument response functions (IRFs) were determined using the water Raman lines and the same excitation and emission filters used for donor lifetime measurements. Fig. 2.5 shows an example of an instrument response function and compares it with a fluorescent decay curve.

$$F(t,\tau) = IRF(t') \otimes I_{\parallel,\perp}(t) = \int_0^t IRF(t')\ I_{\parallel,\perp}(t)\ dt' \tag{2.17}$$

Donor lifetime measurements were acquired for both donor-only and donor-acceptor labeled samples with 50 nM RNA and various Rop concentrations. To find FRET, donor lifetime measurements were acquired for both donor-only and donor-acceptor labeled samples with 50 nM RNA and various Rop concentrations. A nonlinear least-squares fit to the data that incorporated the IRF into the model was used to distinguish between and evaluate single, double, and triple exponential decays of the fluorescence.

2.2 Fluctuation Correlation Spectroscopy

Fluorescence correlation spectroscopy (FCS) characterizes fluctuations in fluorescence intensity [87]. The fluctuations in fluorescence originates in fluctuations in local concentration, reversible changes in fluorescence due to a chemical reaction or photophysical transitions to triplet state, and conformational changes like reversible isomerization. We used FCS to rule out artifacts that might be associated with Rop-dependent dye photophysics. Also FCS was used in an attempt to measure binding kinetics of Rop to R1inv-R2inv KC.

In FCS it is common to use a confocal microscope were the laser light is focused on to the sample using a high numerical aperture objective. Therefore a very small volume of sample ($\approx$ fL) is excited, and only molecules in this volume can emit fluorescence. Emitted photons are registered using an avalanche photodiode after passing through a pinhole (field aperture) that rejects out of focus light. Fluctuations in fluorescence are induced by chaneges in the number of molecules in the focal volume as molecules diffuse in and out. I take $F_i(t)$ to be the fluorescent signal from photons emitted by fluorophores of species i diffusing in detection volume (V_{eff}). Fluorescent

fluctuations ($\delta F_i \equiv F(t) - \langle F(t) \rangle$) are proportional to intensity of the excitation laser ($I_{ext}(r)$) and local concentration ($C_i(r,t)$) of fluorescent species:

$$\delta F_i = \kappa_i \int_V I_{ex}(r) S_i(r) \delta(\sigma_i \; q_i \; C_i(r,t)) \; dV, \tag{2.18}$$

where κ_i is the detection efficiency, $S_i(r)$ is the optical transfer function of the objective-pinhole combination, and σ_i and q_i are the cross section and quantum yield of the fluorophores respectively [87].

Eq. 2.18 can be simplified by defining the distribution function for emission light as, $W_i(r) = S_i(r) * \frac{I_{ex}(r)}{I_0}$ and defining brightness of each species as $\eta_i = I_0 \kappa_i \sigma_i q_i$. Brightness is the count rate per detected molecule. The simplified form for $\delta F_i(t)$ is as follow:

$$\delta F_i = \int_V W(r) \delta(\eta_i \; C_i(r,t)) \; dV, \tag{2.19}$$

$\delta(\eta_i \; C_i(r,t))$ term shows that source of fluctuation is either concentration or brightness.

$W(r)$ is usually assumed to be a Gaussian with lateral and axial $1/e^2$ distribution of r_0 and z_0:

$$W(r) = exp(\frac{-2(x^2+y^2)}{r_0^2}) exp(\frac{-2z^2}{z_0^2}) \tag{2.20}$$

Fluorescent fluctuations can be quantified by autocorrelating the intensity signal (Eq. 2.21). The autocorrelation function ($G(\tau)$) is a measure of the probably of detecting a photon emission from a molecule at time t+τ, if a photon has already been detected from the same molecule at time t:

$$G(\tau) = \frac{\langle \delta F_i(t) \delta F_i(t+\tau) \rangle}{\langle F_i(t) \rangle^2} \tag{2.21}$$

The brackets represent time averaging over all time t. Eq. 2.21 can be solved by inserting Eq. 2.19 for fluorescent fluctuations. The solution for $G(\tau)$ is different depending on the source of fluctuations [34]. In the simplest case where molecules of

species i are freely diffusing in the 3D focal volume (V_{eff}) with a diffusion constant of D_i, the solution for $G(\tau)$ will be:

$$G_{D,i}(\tau) = \frac{1}{V_{eff}\langle C_i\rangle}\ \frac{1}{1+\frac{\tau_i}{\tau_D}}\ \frac{1}{(1+\frac{\tau}{\tau_{D,i}\omega^2})^{\frac{1}{2}}}, \tag{2.22}$$

where V_{eff}= $\pi^{3/2} r_0 z_0^2$ can be found with a calibration using a dye of known diffusivity. $V_{eff}\langle C_i\rangle$ is the measured amplitude of the autocorrelation function ($(G_{D,i}(0))^{-1}$), and represents the average number of molecules in the focal volume (N). The aspect ratio of the detection volume is, $\omega = \frac{z_0}{r_0}$. The radial diffusion time for species i is: $\tau_{D,i} = \frac{r_0^2}{4D_i}$. Two important quantities that can be found by fitting to this model are the number of molecules in the detection volume and the diffusion time (or as a result diffusion coefficient).

For multiple non-interacting fluorescent species, each with brightness η_n, Eq. 2.22 can be generalized as:

$$G_M(\tau) = \frac{1}{V_{eff}}\frac{\sum_n \eta_n \langle C_n\rangle M_n(\tau)}{(\sum_n \eta_n \langle C_n\rangle)^2}, \tag{2.23}$$

Here,

$$M_n(\tau) = \frac{1}{1+\frac{\tau_i}{\tau_D}}\ \frac{1}{(1+\frac{\tau}{\tau_{D,i}\omega^2})^{\frac{1}{2}}} \tag{2.24}$$

Fluctuations in fluorescence can also be due to fluctuations in brightness ($\delta\eta_i$) either from intermolecular dynamics or intramolecular dynamics. Two common photophysical processes in fluorophores which causes changes in fluorescent are transitions to triplet state [99], and photo-induced isomerization and back isomerization of some dyes [100].

For any fluorescent reaction with fluctuations faster than diffusion time, functional form of autocorrelation function will be as follow:

$$G_x(\tau) = \ 1 - X + X \exp^{(\frac{-\tau}{\tau_x})}, \tag{2.25}$$

where τ_x is the correlation time and X is population of that state. Overall correlation function is multiplication of all the correlation functions involved in the process:

$$G_{tot}(\tau) = \ G_D(\tau) G_x(\tau) \tag{2.26}$$

A fluorescent molecule can have reversible transitions to the first excited triplet state as shown in the Jablonski diagram of Fig. 2.3. This process can be considered as a two state system with transitions between bright (B) and dark (D) states. The autocorrelation function ($G_T(\tau)$) for this process is as in Eq. 2.25. Relaxation time for triplet dynamics is defined as τ_T, and T is defined as the average fraction of molecules in the dark state. When the dark state is not completely dark ($\delta\eta_D \neq \ 0$), $T = \ \frac{k_D k_B (\eta_B - \eta_D)^2}{k_D + k_B}$. k_D and k_B are the rate of transitions to the dark and bright states respectively.

Isomerization is another photophysical process which is common in some fluorophores like Cyanine5. Isomerization and back isomerization involves transitions between the *trans* and *cis* states of the fluorophores. Autocorrelation function resulting from isomerization ($G_I(\tau)$) is as defined in Eq. 2.25, with relaxation time of τ_I and isomerization fraction of I.

Thus, when studying a molecular system with dynamics in the time scale $<$ 1ms, fluctuations due to photophyscial effects on the time scale of one to tens of microsecond, should be taken in to account.

The model I used for describing dynamics of the RNA-protein complex with Cy3-Cy5 as the fluorescent probes, includes diffusion, triplet and isomerization terms. The complete model for $G(\tau)$ that I used for fitting to the experimental data is:

$$G(\tau) = G_D(\tau) \prod_{X=T,I} \frac{1}{1-X} \left(1 - X + X \exp(\frac{-\tau}{\tau_i})\right), \tag{2.27}$$

where $G_D(\tau)$ is defined in Eq. 2.22. If more reactions are involved which cause fluorescent fluctuations, they can be added through multiplication of more terms in the form of $G_x(\tau)$. Obviously the presence of multiple reactions with timescales close to each other makes it difficult to resolve the coherence times.

FCS data were acquired on donor-only, acceptor-only and donor-acceptor labeled RNA, with and without Rop in an attempt to measure binding kinetics of Rop to R1inv-R2inv kissing complex. The same experimental setup as the FRET setup, shown in Fig. 2.2, is used for these measurements. Emitted donor and acceptor photons were detected using two avalanche photodiodes (MPD τ-SPAD) and homemade photon timing circuitry based on an FPGA [40]. Data on a particular sample were typically acquired for 30 minutes. The uncertainty on the correlation function was determined by dividing the data set into 10 sequential runs, calculating the correlation function for each, and taking the standard deviation of the ten functions at each lag time.

2.3 Design and preparation of R1inv-R2inv constructs

The design of the RNA strands was informed by our prior work regarding the behavior of dyes attached to the 5′ terminus of double-stranded RNA [66]. MD simulations performed on dye-labeled RNA had indicated that indocyanine dyes tethered by a short linker to a 5′ terminal guanine visit several sites on the RNA, whereas the same dyes attached to a 5′ cytosine remain nearer a position in which the dye is "stacked" on the end of the RNA duplex. Furthermore, earlier work that demonstrated a dependence of FRET on helical twist, as well as length, of a DNA duplex made use of Cy3 and Cy5 attached at 5′ terminal cytosines [74, 50, 51]. We therefore expected that Cy3-Cy5 dye pair attached at 5′ cytosines would have better sensitivity

to angular changes than Cy3-Cy5 attached at 5′ guanine: this turned out to be the case, but perhaps for a different reason.

Two distinct complexes were used in this study, differing only in the terminal base-pair. The R1inv-R2inv complex, whose constituent hairpins are shown in Fig. 2.6(a), has 5′ guanines to which Cy3 and Cy5 were attached. Cyanine dyes stack best on RNA when attached at terminal 5′ cytosine [66], so we also made use of RNA that was identical to the complex of Fig. 2.6(a), except that the 3′ and 5′ bases were swapped (Fig. 2.6(b)). We refer to this complex as R1inv-R2inv-C.

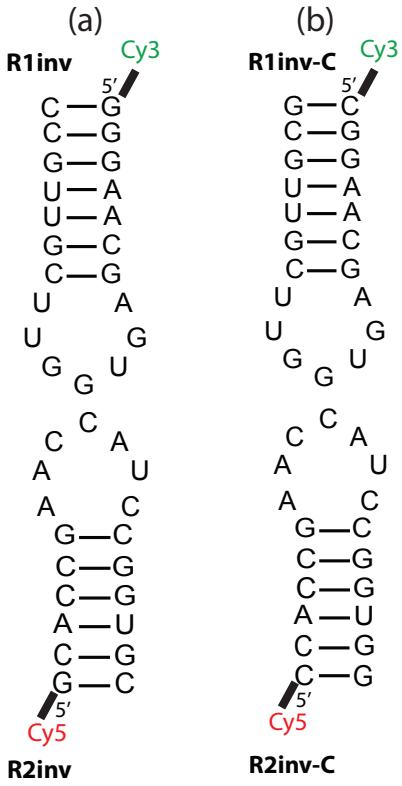

Figure 2.6. R1inv-R2inv kissing complexs, with Cy3 and Cy5 labeled on (a) terminal 5′ Guanine (R1inv-R2inv) and (b) terminal 5′ Cytosine (R1inv-R2inv-C).

RNA and dye-labeled RNA were purchased from Integrated DNA Technologies (IDT). RNA strands at 12 μM were heated for 3 minutes at 93 °C, then snap cooled

on dry ice for 3 minutes to form the hairpins. To form kissing complexes, the R1inv hairpins (2.4 μM) were combined with R2inv hairpins (3 μM) in 20 mM Tris buffer, 100 mM NaCl and 5 mM $MgCl_2$ and then incubated for 30 minutes on ice. For FRET measurements, this solution was diluted again to a final concentration of 100 pM or 200 pM R1inv-R2inv, after which Rop was added. The final solution contained 20 mM Tris buffer (pH 7.8) with 100 mM NaCl and 5 mM $MgCl_2$. To minimize photobleaching and blinking of fluorophores, 15 nM protocatechuate3,4-dioxygenase (PCD) and 5 mM protocatechuic acid (PCA) were added as an enzymatic oxygen scavenger system [2] and methylviologen (MV) was added as part of the reducing and oxidizing system (ROXS) [95].

CHAPTER 3

RESULTS AND ANALYSIS

3.1 Gel shift assay

Binding of Rop to R1inv-R2inv was confirmed using an electrophoretic mobility shift assay, shown in Fig. 3.1. The electrophoretic mobility shift assay was performed using a 15% (0.15 g/mL) polyacrylamide gel as described by Predki *et al.* [79]. Protocol for preparation of gel can be found in Appendix A. The gel was run at 20 mA in a 1x TBM buffer (89 mM Tris at pH 8.3, 89 mM boric acid and 5 mM $MgCl_2$). Ethidium bromide was used for staining the gel and visualizing the bands. Lane 1 contains duplex DNA (10 bp DNA ladder from Promega) from 10 bp to 100 bp. Lanes 8 and 9 contain 2 μM of R1inv-Cy3 and R2inv-Cy5 hairpins separately. All the other lanes contain 1 μM of R1inv-R2inv complex with Rop concentration ranging from 0 μM to 250 μM. A clear shift attributed to Rop binding is evident in lanes 6 and 7 at Rop concentrations of 100 μM and 250 μM respectively. Some evidence of binding is also noted in lane 5 at 10 μM. Note that gel shift assays result in much higher apparent dissociation constants for Rop binding [79] than other assays [83, 31], presumably due to the instability of the complex under electrophoresis, but are still useful to confirm binding.

3.2 Results and Analysis: Solution Ratiometric FRET

Single molecular-pair FRET (spFRET) was used to investigate the structural changes of the R1inv-R2inv complex. To make use of the sensitivity of FRET to changes in dye orientation, we also studied R1inv-R2inv-C, in which the terminal

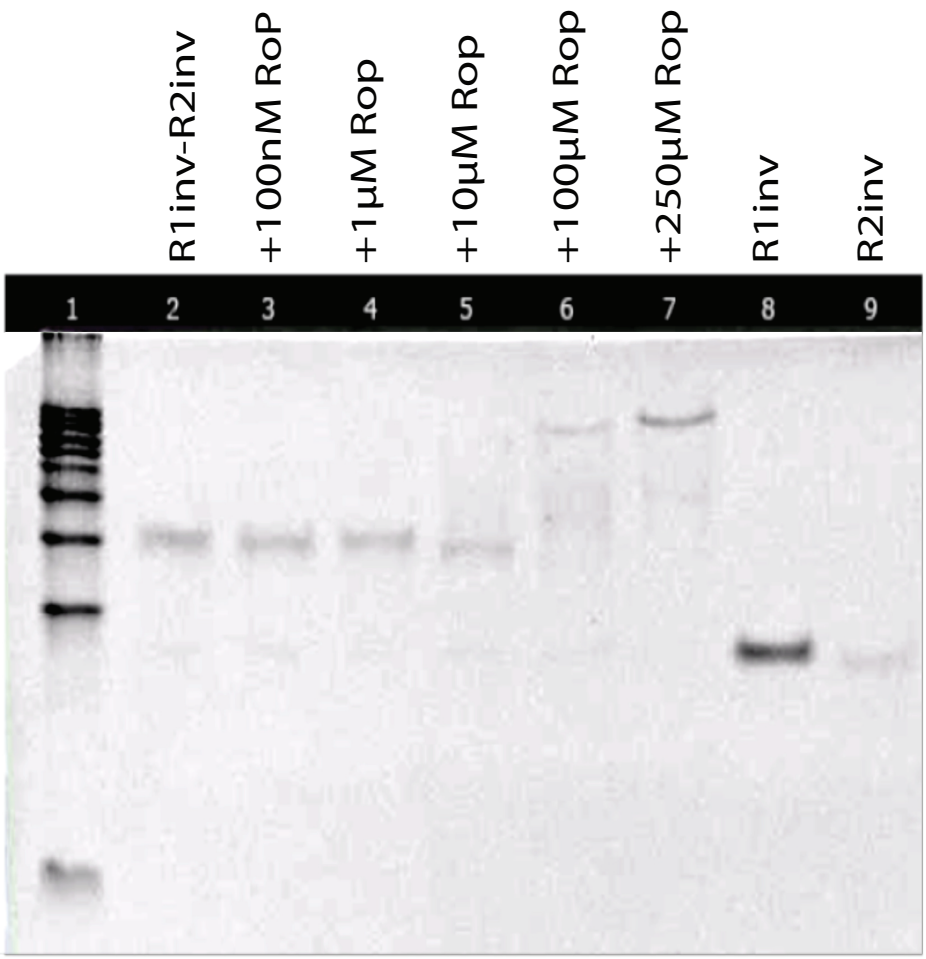

Figure 3.1. Electrophoretic gel demonstrating the binding of Rop to the RNA loop-loop complex. The first lane is a DNA ladder. Note that R1inv is labeled with Cy3 and R2inv with Cy5, and the gel is stained with ethidium bromide, which may account for the apparently brighter signal from R1inv at nominally the same concentration.

base-pair on the stem of each hairpin was flipped, so that the 5′ terminal base in both cases is a cytosine instead of guanine. This change does not affect Rop binding, which is known to depend only on the structure of the kissing interface and nearest bases [31] and is not sensitive to changes in the terminal base pair.

The results of single-molecule-sensitive FRET measurements on freely-diffusing R1inv-R2inv-C show a clear shift in the average proximity ratio with increasing Rop concentration. Typical results are shown in Fig. 3.2(a) and Table 3.1. The maximum shift in the average proximity ratio $\langle P \rangle$ upon addition of Rop is small, but it is approximately an order of magnitude larger than the uncertainty on the average values; see Table 3.1 for a complete reporting of fit parameters. The mean value of the proximity ratio $\langle P \rangle$ and the standard deviation of the distribution σ_p are returned by a nonlinear least-squares fit of a Gaussian with two adjustable parameters to the proximity histograms of Fig. 3.2. The uncertainties on these parameters are returned by the fit; however, it is worth noticing that the uncertainty in the mean of a distribution is also given by $\sigma_p/\sqrt{N}$, where σ_p is the standard deviation of the distribution and N is the total number of FRET measurements (bins) in the measurement. The uncertainty in $\langle P \rangle$ calculated in this way agrees with the uncertainty returned by the fit. Complete fit parameters are given in Table 3.1.

In Fig. 3.2(a) the 5′ C labeled RNA complex is present at a nominal concentration of 100 pM, and Rop when present is at 10 nM, 100 nM, 1 μM, 10 μM and 50 μM. Without Rop present, two separate measurements gave $\langle P \rangle = 0.504 \pm 0.002$ [shown as the grey vertical line in Fig. 3.2] and $\langle P \rangle = 0.492 \pm 0.003$. These two measurements were taken at the beginning and end of data acquisition to check for instrument drift: they show a small drift in the direction opposite the shift with Rop, implying that the observed shift in $\langle P \rangle$ is probably a lower limit. In contrast, for the R1inv-R2inv duplex at 200 pM, with dyes attached to a terminal 5′ G, there was no significant change in the FRET distribution upon the addition of Rop, Fig. 3.2(b). These measurements

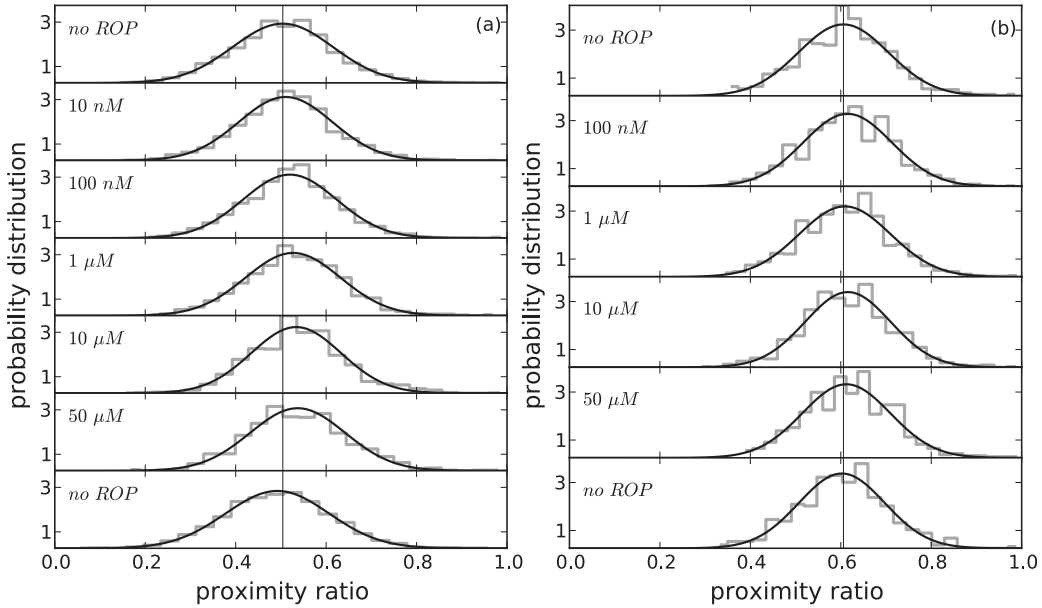

Figure 3.2. Proximity ratio histograms for (a) R1inv-R2inv-C kissing complex and (b) R1inv-R2inv kissing complex at various Rop concentrations from 0 to 50 μM. The threshold for inclusion in the histogram is 25 photons in a 5 ms bin. The black curves are the best fits of a Gaussian to the data. The vertical line represents the $\langle P \rangle$ for the data with no Rop in the top panel. A small but distinct shift in FRET is apparent with the addition of Rop in (a) but not in (b). The data are displayed in the order they were taken: to check for drift, data with no Rop were acquired at the beginning and end of the sequence.

Table 3.1. Results of fits to the data of Fig. 3.2. $\langle P \rangle$ is the mean and σ_p is the standard deviation of the proximity ratio histogram for the R1inv-R2inv-C complex or the R1inv-R2inv complex at different concentrations of Rop. The standard deviation attributable to shot-noise alone, σ_{sn}, and the total number of bins under each peak, N, are also given.

	R1inv-R2inv-C				R1inv-R2inv			
[Rop] (μM)	$\langle P \rangle$	σ_p	σ_{sn}	N	$\langle P \rangle$	σ_p	σ_{sn}	N
0	0.504 ± 0.002	0.111 ± 0.002	0.086	3014	0.606 ± 0.004	0.099 ± 0.003	0.087	839
0.01	0.510 ± 0.003	0.103 ± 0.002	0.086	2321	-	-	-	-
0.1	0.520 ± 0.003	0.103 ± 0.002	0.084	1795	0.614 ± 0.003	0.097 ± 0.002	0.086	1095
1	0.527 ± 0.003	0.105 ± 0.002	0.084	1663	0.610 ± 0.004	0.100 ± 0.003	0.086	977
10	0.534 ± 0.003	0.099 ± 0.002	0.084	1339	0.616 ± 0.004	0.094 ± 0.003	0.086	772
50	0.537 ± 0.004	0.105 ± 0.003	0.084	862	0.616 ± 0.004	0.089 ± 0.003	0.084	619
0	0.492 ± 0.003	0.114 ± 0.002	0.088	1883	0.603 ± 0.006	0.095 ± 0.004	0.084	371

were also repeated later with similar results, giving $\langle P \rangle = 0.598 \pm 0.003$ for R1inv-R2inv without Rop present, and $\langle P \rangle = 0.605 \pm 0.009$ for R1inv-R2inv with 50 μM Rop. Here the small shift observed in average proximity ratio upon binding of protein is negligible in comparison with that of the R1inv-R2inv-C complex.

In Table. 3.1, σ_s denotes the expected shot-noise-limited width of the distributions [42], which is given by ${\sigma_s}^2 = \langle P \rangle (1 - \langle P \rangle)/\langle N_a + N_d \rangle$, where $N_a + N_d$ is the total number of photons in a bin which is typically 34. For R1inv-R2inv with 5′ G attached dyes the width of the proximity distributions in Fig. 3.2(b) is close to shot-noise limited . For R1inv-R2inv-C, the width of the proximity distributions in Fig. 3.2(a) are clearly larger than would be expected from shot-noise. This is not unusual for the Cy3-Cy5 dye pair, and the broadening is usually attributed to the isomerization of Cy5 [52]. This would not, however, explain the apparent difference in width of the proximity distribution for the two RNA kissing construct. There is also weak evidence for a small but systematic reduction in width with the addition of Rop to R1inv-R2inv-C, Table. 3.1. It is therefore possible that at least some of the width observed in the FRET histograms may be due to structural heterogeneities of the RNA kissing complex that are evident in for 5′ C attached dyes but not for 5′ G attached dyes. A broadening of the proximity histogram for the 5′ C complex would require structural sub-species that have lifetimes longer than the interphoton arrival time, typically 20-200 μs here; from the already identified minimized energy structures, we infer that these subspecies probably vary primarily in twist or bend angle. If this is indeed the case, then Rop binding might suppress some structural sub-species, which would be consistent with both a narrowing and a shift in the FRET distribution for the 5′ terminal C labeled complexes. The narrower width of the data for the R1inv-R2inv 5′ G labeled complexes would also seem to support this idea: because the transition dipole moments of dyes attached to 5′ terminal G are oriented parallel to each other and show smaller fluctuations, FRET is almost maximized for this complex

and subtle angular changes in RNA kissing complex structure will not be resolvable by this complex.

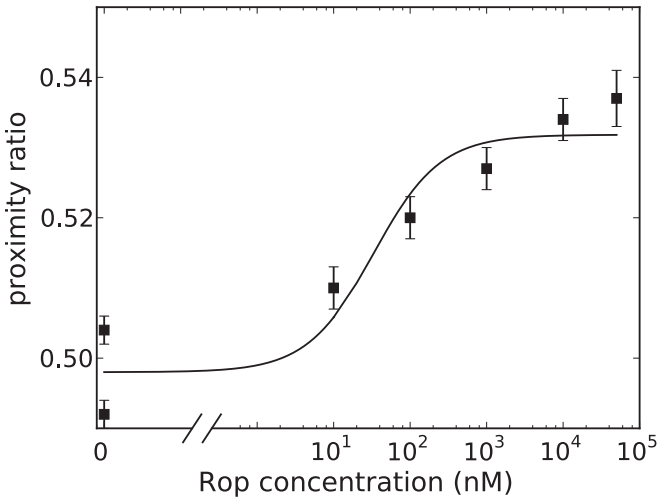

Figure 3.3. Proximity ratio for 100 pM R1inv-R2inv-C at different concentrations of Rop (squares). Solid line shows the best fit binding curve, giving k_d of 33.2±17 nM and a change in $\langle P \rangle$ of 0.034±0.004. For fitting, $\langle P \rangle$ at zero Rop was fixed at the average of the two measurements.

The average proximity ratio as a function of Rop (Fig. 3.3) was used to determine the dissociation constant for Rop binding. We find k_d= 33.2± 17 nM, in agreement with prior measurement of 60 ± 24 nM [83] and 45 nM [31]. The data and resulting fit, using a single site equilibrium binding equation [3, 83] are shown in Fig. 3.3. The fit model was found by considering a reaction as follow for the RNA-protein complex:

$$\text{RNA} + \text{protein} \rightleftharpoons \text{complex}$$

Dissociation constant for this reaction is defined as:

$$K_D = \frac{[RNA][protein]}{[complex]}, \tag{3.1}$$

where [RNA] and [protein] are concentrations of free RNA and protein. Since these quantities are not easy to measure we are going to write K_D in terms of total concen-

tration of RNA and protein ([RNA]$_{tot}$ and [protein]$_{tot}$), these are the concentrations added initially.

$$\begin{aligned} [RNA] &= [RNA]_{tot} - [complex] \\ [protein] &= [protein]_{tot} - [complex] \end{aligned}$$

Substituting them in Eq. 3.1,

$$K_D = \frac{([RNA]_{tot} - [complex])([protein]_{tot} - [complex])}{[complex]} \tag{3.2}$$

Organizing Eq. 3.2 will give a second order polynomial equation, and we are trying to solve for [complex]:

$$[complex]^2 - ([RNA]_{tot} + [protein]_{tot} + K_D)[complex] + [RNA]_{tot}[protein]_{tot} = 0 \tag{3.3}$$

For convenience we are defining $b = [RNA]_{tot} + [protein]_{tot} + K_D$. Solving for concentration of complex ([complex]) results in:

$$[complex] = \frac{-b \pm \sqrt{b^2 - 4[RNA]_{tot}[protein]_{tot}}}{2} \tag{3.4}$$

The probability of being bound (P_b) is the amount of RNA being bound in complex divided by total concentration of RNA:

$$P_{bound} = \frac{[complex]}{[RNA]_{tot}} = \frac{-b \pm \sqrt{b^2 - 4[RNA]_{tot}[protein]_{tot}}}{2[RNA]_{tot}} \tag{3.5}$$

At zero concentration of protein there is no complex formed, therefore P_{bound} is zero. Here our probe for binding is FRET, and even the unbound RNA has nonzero FRET. Therefore to model binding curve derived from FRET results, we need to

scale P_{bound} and consider the initial value of FRET. To express the fluorescent data in terms of binding probability, we assumed a linear relationship between FRET and probability of binding. The model we used for fitting to the binding curve is as follow:

$$PR \;=\; [(PR)_{final} - (PR)_{init}]\; P_{bound} + (PR)_{init} \tag{3.6}$$

For the two-parameter fit, the value of $\langle P \rangle$ measured at zero Rop concentration was fixed at the mean value of the two data points, $\langle P \rangle = 0.498$. A total increase of $6.6 \pm 0.8\%$, to $\langle P \rangle = 0.532 \;\pm\; 0.002$, is observed upon Rop binding for the data of Fig. 3.2(a). The second run with R1inv-R2inv-C at 200 pM gave similar results, with a shift in $\langle P \rangle$ of $8.6 \pm 0.8\%$. The difference can be due to systematic drift.

In summary: Since Rop binding is not sensitive to the terminal base pair, the same structural change should be present for both constructs. However, only R1inv-R2inv-C reports a change in FRET upon Rop binding. This result is consistent with the model we discuss later that Rop induces a change in twist of the complex.

3.3 Results and Analysis: Time-resolved lifetime measurements

To find FRET before and after binding of Rop protein, we first measure the fluorescence polarization anisotropy decay of Cy3 on donor-only labeled R1inv-R2inv-C and R1inv-R2inv as a function of [Rop]. The results are fitted with the model described by Eqs. 2.14a and 2.14b and convolved with IRFs (Eq. 2.17). Fig. 3.4 and Fig. 3.5 shows the fluorescence decay curves in perpendicular and parallel channels ($I_\perp$ and $I_\parallel$) and the corresponding fits to this data for R1inv-R2inv-C KC at different Rop concentrations. Fig. 3.6 and Fig. 3.7 shows the results of a similar fit to the fluorescence decay curves in perpendicular and parallel channels ($I_\perp$ and $I_\parallel$)

for R1inv-R2inv complex at different [Rop]. These figures also include the residuals corresponding to each fit.

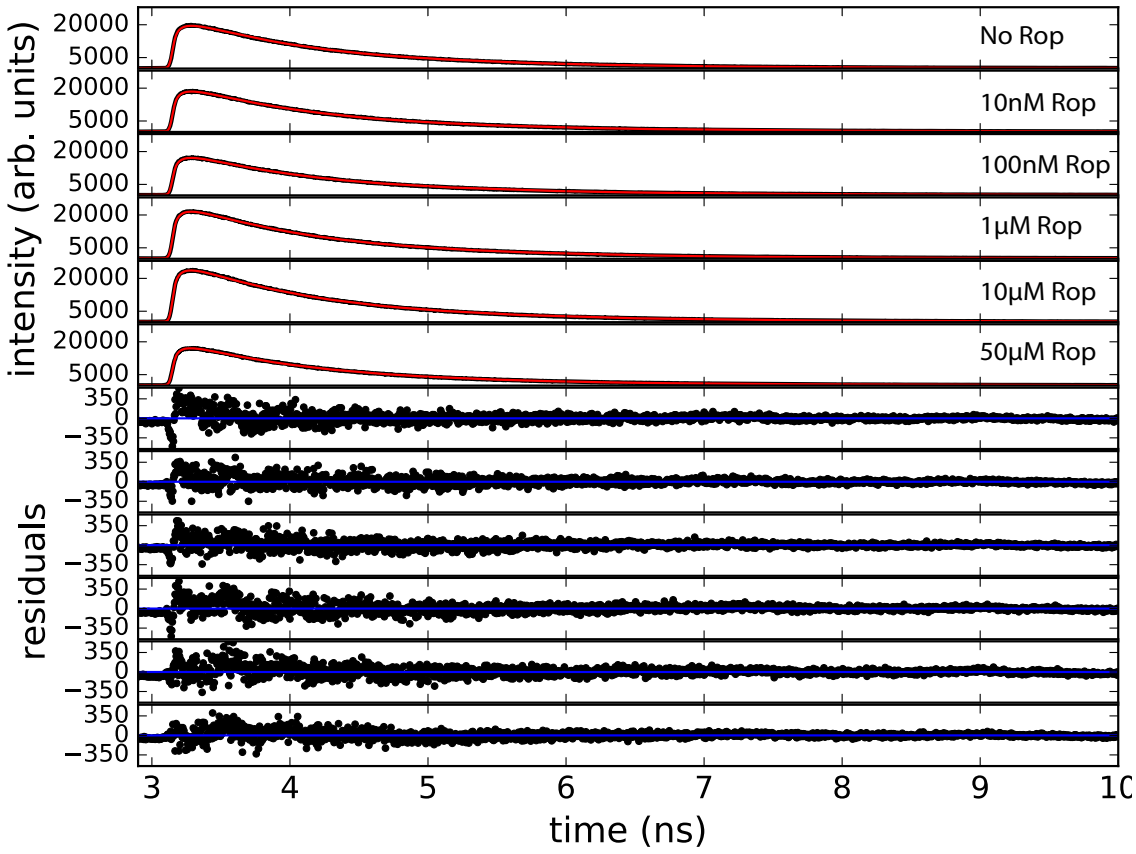

Figure 3.4. Fluorescence lifetime decay curves and the corresponding fits to them for Cy3 on donor-only labeled R1inv-R2inv-C at different [Rop] in perpendicular polarization channel ($I_\perp$). Residuals corresponding to fits are included.

The donor-only fluorescence lifetime for both R1inv-R2inv-C and R1inv-R2inv revealed three fluorescence lifetimes, which had no systematic variation with [Rop]. This would indicate that there is no quenching associate with the addition of Rop alone.

We therefore did a global fit for the τ_{iD} across all Rop concentrations, and found for R1inv-R2inv-C $\tau_1 = 1.315 \pm 0.005$ ns, $\tau_2 = 0.705 \pm 0.008$ ns and $\tau_3 = 0.193 \pm 0.004$ ns. The population associated with each state is given by $A_{iD}\tau_{iD} / \sum_i A_{iD}\tau_{iD}$ and

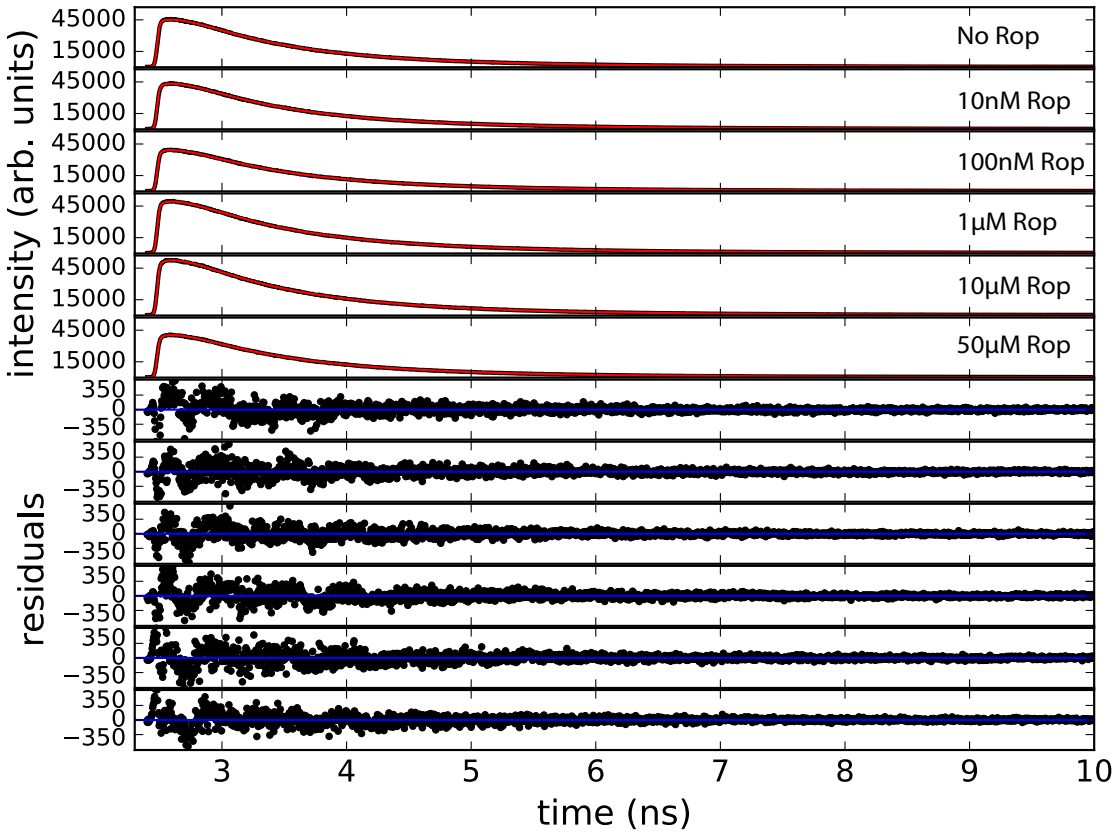

Figure 3.5. Fluorescence lifetime decay curves and the corresponding fits to them for Cy3 on donor-only labeled R1inv-R2inv-C at different [Rop] in parallel polarization channel ($I_{\parallel}$). Residuals corresponding to fits are included.

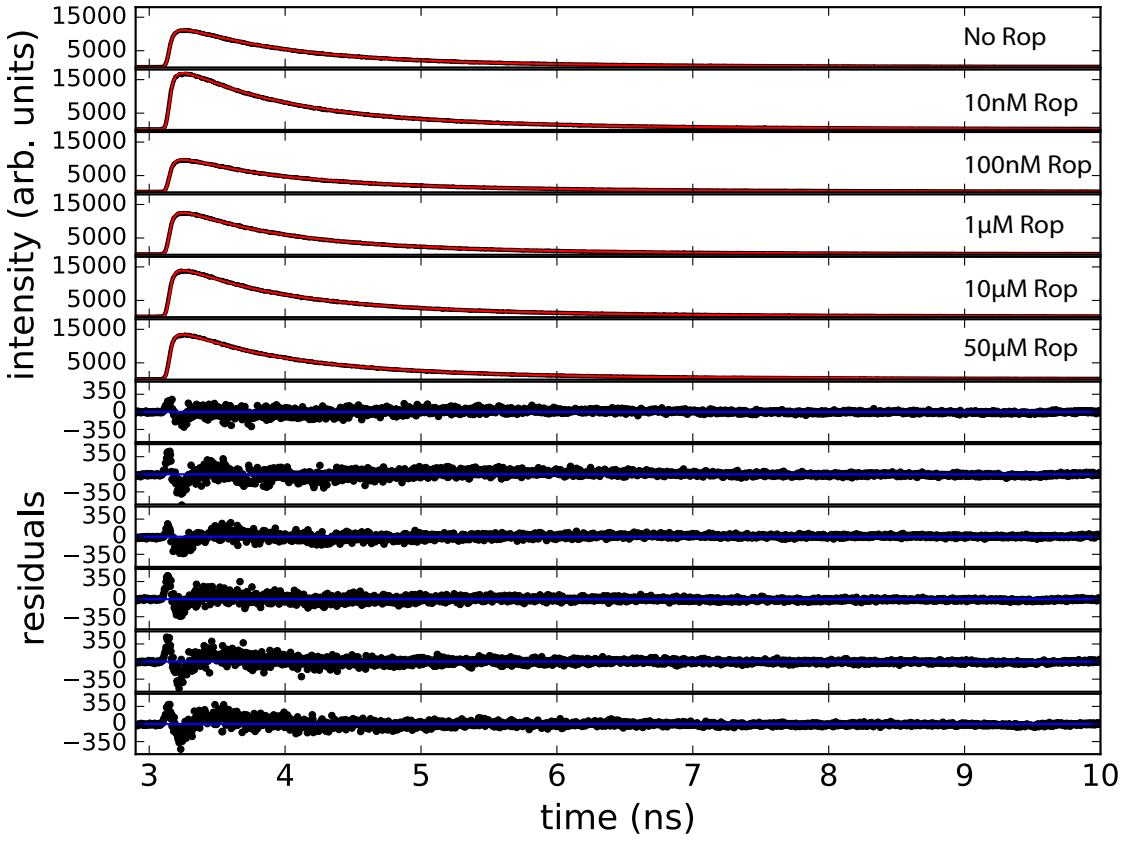

Figure 3.6. Fluorescence lifetime decay curves and the corresponding fits to them for Cy3 on donor-only labeled R1inv-R2inv at different [Rop] in perpendicular polarization channel ($I_{\perp}$). Residuals corresponding to fits are included.

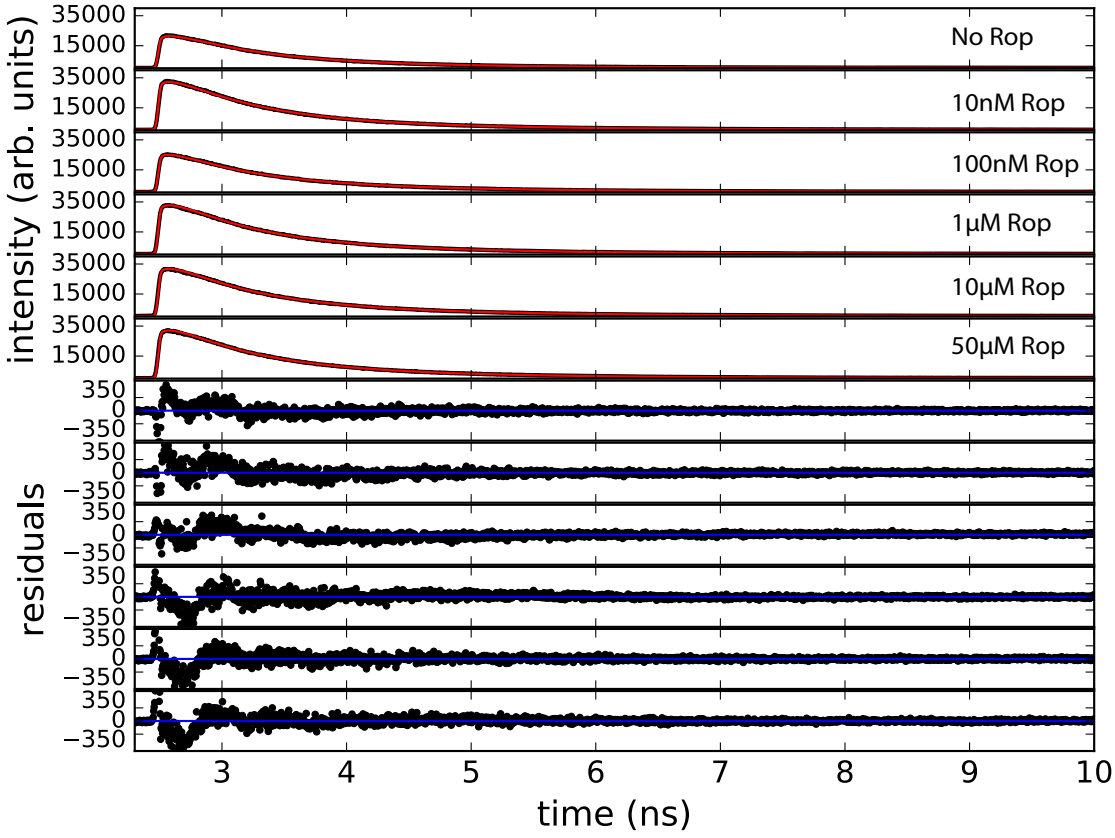

Figure 3.7. Fluorescence lifetime decay curves and the corresponding fits to them for Cy3 on donor-only labeled R1inv-R2inv at different [Rop] in parallel polarization channel ($I_{\parallel}$). Residuals corresponding to fits are included.

found to be about 61%, 33% and 3.5% for $i = 1, 2, 3$ respectively, Fig. 3.8(a). Note that, there is no significant systematic change in the populations with [Rop]. The intensity weighted lifetime, used in calculating average FRET, was calculated using [97] $\langle\tau\rangle = \frac{\sum_i A_i\tau_i^2}{\sum_i A_i\tau_i} = 1.06 \pm 0.005$ ns. The result of the fit to R1inv-R2inv-C lifetime data is reported in Table. 3.2.

For R1inv-R2inv the lifetime results were similar, with $\tau_1 = 1.488 \pm 0.005$ ns, $\tau_2 = 0.689 \pm 0.003$ ns and $\tau_3 = 0.185 \pm 0.002$ ns. The corresponding amplitudes showed no systematic change with [Rop], and the populations were 45%, 46% and 6.5%, respectively, Fig. 3.8(b). Again, there is no significant systematic change in the populations with [Rop]. The intensity weighted lifetime was calculated to be 1.0 ± 0.004 ns. Table. 3.5 summarizes the result of the fits for R1inv-R2inv KC labeled on $5'C$ and $5'C$ with Cy3-only and Cy3-Cy5 pair.

The rotational correlation times for R1inv-R2inv-C were consistent with the notion that shorter fluorescent lifetimes are associated with rotationally freer dyes, we found that the shorter the lifetime, the shorter the rotational correlation time. Individual fits for θ_is indicated no systematic change with [Rop]; this confirms our prediction that binding of Rop doesn't change rotational lifetime of Cy3. We therefore fit θ_i globally across all data sets giving $\theta_1 = 0.461 \pm 0.024$ ns, $\theta_2 = 0.054 \pm 0.005$ ns and $\theta_3 = 0.007 \pm 0.003$ ns. The long-lifetime state (θ_1) represents Cy3 stacked on RNA, and therefore has the longest rotational lifetime. The rotational correlation time of the RNA molecule (ϕ), has the longest lifetime and increases with binding of Rop protein. At different concentrations of Rop there is a population of bound and unbound RNA molecules, therefore what we measure is $\langle\phi\rangle$ for bound and unbound RNA molecules. Using $\langle\phi\rangle$, population of bound RNA was calculated and by fitting a single site equilibrium binding equation to the data (Eq. 3.5), as shown in Fig.3.8(c), K_d= 779.3±191.8 nM was measured. C_is, which are the degree of the motional restriction of the dye, were also globally fitted across all Rop concentrations, giving:

Table 3.2. Results of the fits to the fluorescence lifetime decay curves for R1inv-R2inv-C labeled with Cy3 only (top panel), and labeled with Cy3-Cy5 (bottom panel). For donor-only data, τ_{1D}, τ_{2D}, τ_{3D}, θ_1, θ_2, θ_3, C_1, C_2 are globally fitted. For FRET data, only τ_3 is globally fitted. τ_{1D}, τ_{2D}, τ_{3D}, θ_1, θ_2, θ_3, C_1, C_2, ϕ are fixed to the values found from donor-only fits.

Rop	τ_{1D} (ns)	τ_{2D} (ns)	τ_{3D} (ns)	F_{1D}	F_{2D}	F_{3D}	θ_1 (ns)	θ_2 (ns)	θ_3 (ns)	ϕ (ns)	C_1	C_2	C_3	τ_1 (ns)	τ_2 (ns)	τ_3 (ns)	F_1	F_2	F_3	B_1	α	B_2
0 nM	1.314 (0.005)	0.703 (0.008)	0.192 (0.004)	1.60 (0.03)	1.75 (0.02)	0.61 (0.02)	0.46 (0.02)	0.054 (0.005)	0.007 (0.003)	8.4 (0.55)	0.63 (0.01)	0.52 (0.03)	0	-	-	-	-	-	-	1.16 (0.02)	0.38	-
10 nM	1.314	0.703	0.192	1.58 (0.03)	1.57 (0.02)	0.6 (0.01)	0.46	0.054	0.007	8.98	0.63	0.52	0	-	-	-	-	-	-	1.17 (0.02)	0.38	-
100 nM	1.314	0.703	0.192	1.48 (0.03)	1.42 (0.02)	0.57 (0.01)	0.46	0.054	0.007	10.3	0.63	0.52	0	-	-	-	-	-	-	1.14 (0.02)	0.38	-
1 μM	1.314	0.703	0.192	1.92 (0.04)	1.76 (0.02)	0.7(0.01)	0.46	0.054	0.007	26.5	0.63	0.52	0	-	-	-	-	-	-	1.13 (0.02))	0.38	-
10 μM	1.314	0.703	0.192	2.14 (0.04)	1.87 (0.02)	0.82 (0.02)	0.46	0.054	0.007	29.9	0.63	0.52	0	-	-	-	-	-	-	1.10 (0.02)	0.38	-
50 μM	1.314	0.703	0.192	1.55 (0.03)	1.31 (0.02)	0.63 (0.01)	0.46	0.054	0.007	31.3	0.63	0.52	0	-	-	-	-	-	-	1.18 (0.02)	0.38	-
0 nM	1.314	0.703	0.192	-	-	0.07	0.46	0.054	0.007	8.4	0.63	0.52	0	1.06 (0.03)	0.51 (0.01)	0.136 (0.002)	1.5 (0.1)	1.6 (0.2)	0.62 (0.04)	-	0.38	1.14 (0.002)
10 nM	1.314	0.703	0.192	-	-	0.04	0.46	0.054	0.007	8.98	0.63	0.52	0	1.06 (0.03)	0.50 (0.01)	0.136 (0.002)	1.35 (0.09)	1.38 (0.13)	0.55 (0.04)	-	0.38	1.16 (0.002)
100 nM	1.314	0.703	0.192	-	-	0.12	0.46	0.054	0.007	10.3	0.63	0.52	0	0.99 (0.03)	0.47 (0.01)	0.136 (0.002)	1.17 (0.05)	1.14 (0.09)	0.42 (0.02)	-	0.38	1.15 (0.002)
1 μM	1.314	0.703	0.192	-	-	0.16	0.46	0.054	0.007	26.5	0.63	0.52	0	0.96 (0.02)	0.44 (0.01)	0.136 (0.002)	1.29 (0.03)	1.12 (0.07)	0.42 (0.02)	-	0.38	1.19 (0.002)
10 μM	1.314	0.703	0.192	-	-	0.2	0.46	0.054	0.007	29.9	0.63	0.52	0	0.91 (0.01)	0.43 (0.008)	0.136 (0.002)	1.19 (0.02)	0.95 (0.04)	0.39 (0.02)	-	0.38	1.20 (0.002)
50 μM	1.314	0.703	0.192	-	-	0.26	0.46	0.054	0.007	31.3	0.63	0.52	0	0.91 (0.01)	0.43 (0.008)	0.136 (0.002)	1.31 (0.03)	1.11 (0.05)	0.4 (0.02)	-	0.38	1.18 (0.002)

Table 3.3. Results of the fits to the fluorescence lifetime decay curves for R1inv-R2inv-C (top panel) and R1inv-R2inv-G (bottom panel), labeled with Cy3. τ_{1D}, τ_{2D}, τ_{3D}, θ_1, θ_2, θ_3, C_1, C_2 are globally fitted.

Rop	τ_{D1} (ns)	τ_{D2} (ns)	τ_{D3} (ns)	F_{D1}	F_{D2}	F_{D3}	θ_1 (ns)	θ_2 (ns)	θ_3 (ns)	ϕ (ns)	C_1	C_2	C_3	B
0 nM	1.314 (0.005)	0.703 (0.008)	0.192 (0.004)	1.60 (0.03)	1.75 (0.02)	0.61 (0.02)	0.46 (0.02)	0.054 (0.005)	0.007 (0.003)	8.4 (0.55)	0.63 (0.01)	0.52 (0.03)	0	1.16 (0.02)
10 nM	1.314	0.703	0.192	1.58 (0.03)	1.57 (0.02)	0.6 (0.01)	0.46	0.054	0.007	8.98	0.63	0.52	0	1.17 (0.02)
100 nM	1.314	0.703	0.192	1.48 (0.03)	1.42 (0.02)	0.57 (0.01)	0.46	0.054	0.007	10.3	0.63	0.52	0	1.14 (0.02)
1 μM	1.314	0.703	0.192	1.92 (0.04)	1.76 (0.02)	0.7(0.01)	0.46	0.054	0.007	26.5	0.63	0.52	0	1.13 (0.02))
10 μM	1.314	0.703	0.192	2.14 (0.04)	1.87 (0.02)	0.82 (0.02)	0.46	0.054	0.007	29.9	0.63	0.52	0	1.10 (0.02)
50 μM	1.314	0.703	0.192	1.55 (0.03)	1.31 (0.02)	0.63 (0.01)	0.46	0.054	0.007	31.3	0.63	0.52	0	1.18 (0.02)
0 nM	1.509 (0.006)	0.698 (0.004)	0.186 (0.002)	0.413 (0.006)	1.066 (0.005)	0.509 (0.006)	0.227 (0.006)	0.003 (0.001)	0.008 (0.001)	8.4	0.196 (0.007)	0.396 (0008)	0	1.317 (0.008)
10 nM	1.509	0.698	0.186	0.651 (0.01)	1.549 (0.007)	0.826 (0.008)	0.227	0.003	0.008	8.98	0.196	0.396	0	1.311 (0.007)
100 nM	1.509	0.698	0.186	0.436 (0.006)	0.766 (0.004)	0.545 (0.005)	0.227	0.003	0.008	10.3	0.196	0.396	0	1.78 (0.01)
1 μM	1.509	0.698	0.186	0.495 (0.007)	1.111 (0.005)	0.643 (0.006)	0.227	0.003	0.008	26.5	0.196	0.396	0	1.80 (0.01)
10 μM	1.509	0.698	0.186	0.583 (0.008)	1.188 (0.006)	0.742 (0.006)	0.227	0.003	0.008	29.9	0.196	0.396	0	1.57 (0.01)
50 μM	1.509	0.698	0.186	0.557 (0.008)	1.157 (0.006)	0.710 (0.006)	0.227	0.003	0.008	31.3	0.196	0.396	0	1.64 (0.01)

Table 3.4. Results of the fits to the fluorescence lifetime decay curves for R1inv-R2inv-C (top panel) and R1inv-R2inv-G (bottom panel), labeled with Cy3 and Cy5.

Rop	F_{D1}	F_{D2}	F_{D3}	τ_1 (ns)	τ_2 (ns)	τ_3 (ns)	F_1	F_2	F_3	B
0 nM	0.18	0.20	0.07	1.06 (0.03)	0.51 (0.01)	0.136 (0.002)	1.5 (0.1)	1.6 (0.2)	0.62 (0.04)	1.14 (0.002)
10 nM	0.10	0.10	0.04	1.06 (0.03)	0.50 (0.01)	0.136 (0.002)	1.35 (0.09)	1.38 (0.13)	0.55 (0.04)	1.16 (0.002)
100 nM	0.31	0.30	0.12	0.99 (0.03)	0.47 (0.01)	0.136 (0.002)	1.17 (0.05)	1.14 (0.09)	0.42 (0.02)	1.15 (0.002)
1 μM	0.44	0.41	0.16	0.96 (0.02)	0.44 (0.01)	0.136 (0.002)	1.29 (0.03)	1.12 (0.07)	0.42 (0.02)	1.19 (0.002)
10 μM	0.51	0.45	0.2	0.91 (0.01)	0.43 (0.008)	0.136 (0.002)	1.19 (0.02)	0.95 (0.04)	0.39 (0.02)	1.20 (0.002)
50 μM	0.63	0.53	0.26	0.91 (0.01)	0.43 (0.008)	0.136 (0.002)	1.31 (0.03)	1.11 (0.05)	0.4 (0.02)	1.18 (0.002)
0 nM	0.14	0.36	0.17 (0.01)	0.939 (0.019)	0.472 (0.004)	0.180 (0.002)	0.65 (0.01)	1.43 (0.01)	0.79 (0.02)	1.414 (0.002)
10 nM	0.15	0.36	0.19 (0.02)	0.956 (0.02)	0.467 (0.004)	0.180 (0.002)	0.66 (0.01)	1.56 (0.04)	0.75 (0.02)	1.400 (0.002)
100 nM	0.29	0.50	0.36 (0.01)	0.861 (0.019)	0.469 (0.003)	0.180 (0.002)	0.57 (0.01)	1.52 (0.04)	0.67 (0.02)	1.309 (0.001)
1 μM	0.20	0.45	0.26 (0.02)	0.946 (0.024)	0.483 (0.003)	0.180 (0.002)	0.57 (0.01)	1.58 (0.05)	0.80 (0.02)	1.067 (0.001)
10 μM	0.16	0.33	0.21 (0.02)	0.970 (0.025)	0.488 (0.003)	0.180 (0.002)	0.51 (0.01)	1.49 (0.04)	0.73 (0.02)	1.301 (0.002)
50 μM	0.17	0.36	0.22 (0.02)	1.010 (0.025)	0.501 (0.003)	0.180 (0.002)	0.62 (0.02)	1.88 (0.05)	0.92 (0.02)	1.238 (0.001)

Table 3.5. Results of the fits to the fluorescence lifetime decay curves for R1inv-R2inv-C labeled with Cy3 only (top panel), and labeled with Cy3-Cy5 (bottom panel). For donor-only data, τ_{1D}, τ_{2D}, τ_{3D}, θ_1, θ_2, θ_3, C_1, C_2 are globally fitted. For FRET data, only τ_3 is globally fitted. τ_{1D}, τ_{2D}, τ_{3D}, θ_1, θ_2, θ_3, C_1, C_2, ϕ are fixed to the values found from donor-only fits.

Rop	τ_{1D} (ns)	τ_{2D} (ns)	τ_{3D} (ns)	F_{1D}	F_{2D}	F_{3D}	θ_1 (ns)	θ_2 (ns)	θ_3 (ns)	ϕ (ns)	C_1	C_2	C_3	τ_1 (ns)	τ_2 (ns)	τ_3 (ns)	F_1	F_2	F_3	B_1	α	B_2
0 nM	1.509 (0.006)	0.698 (0.004)	0.186 (0.002)	0.413 (0.006)	1.066 (0.005)	0.509 (0.006)	0.227 (0.006)	0.003 (0.001)	0.008 (0.001)	8.4	0.196 (0.007)	0.396 (0008)	0	-	-	-	-	-	-	1.317 (0.008)	0.38	-
10 nM	1.509	0.698	0.186	0.651 (0.01)	1.549 (0.007)	0.826 (0.008)	0.227	0.003	0.008	8.98	0.196	0.396	0	-	-	-	-	-	-	1.311 (0.007)	0.38	-
100 nM	1.509	0.698	0.186	0.436 (0.006)	0.766 (0.004)	0.545 (0.005)	0.227	0.003	0.008	10.3	0.196	0.396	0	-	-	-	-	-	-	1.78 (0.01)	0.38	-
1 μM	1.509	0.698	0.186	0.495 (0.007)	1.111 (0.005)	0.643 (0.006)	0.227	0.003	0.008	26.5	0.196	0.396	0	-	-	-	-	-	-	1.80 (0.01)	0.38	-
10 μM	1.509	0.698	0.186	0.583 (0.008)	1.188 (0.006)	0.742 (0.006)	0.227	0.003	0.008	29.9	0.196	0.396	0	-	-	-	-	-	-	1.57 (0.01)	0.38	-
50 μM	1.509	0.698	0.186	0.557 (0.008)	1.157 (0.006)	0.710 (0.006)	0.227	0.003	0.008	31.3	0.196	0.396	0	-	-	-	-	-	-	1.64 (0.01)	0.38	-
0 nM	1.509	0.698	0.186	-	-	0.17 (0.01)	0.227	0.003	0.008	8.4	0.196	0.396	0	0.939 (0.019)	0.472 (0.004)	0.180 (0.002)	0.65 (0.01)	1.43 (0.01)	0.79 (0.02)	-	0.38	1.414 (0.002)
10 nM	1.509	0.698	0.186	-	-	0.19 (0.02)	0.227	0.003	0.008	8.98	0.196	0.396	0	0.956 (0.02)	0.467 (0.004)	0.180 (0.002)	0.66 (0.01)	1.56 (0.04)	0.75 (0.02)	-	0.38	1.400 (0.002)
100 nM	1.509	0.698	0.186	-	-	0.36 (0.01)	0.227	0.003	0.008	10.3	0.196	0.396	0	0.861 (0.019)	0.469 (0.003)	0.180 (0.002)	0.57 (0.01)	1.52 (0.04)	0.67 (0.02)	-	0.38	1.309 (0.001)
1 μM	1.509	0.698	0.186	-	-	0.26 (0.02)	0.227	0.003	0.008	26.5	0.196	0.396	0	0.946 (0.024)	0.483 (0.003)	0.180 (0.002)	0.57 (0.01)	1.58 (0.05)	0.80 (0.02)	-	0.38	1.067 (0.001)
10 μM	1.509	0.698	0.186	-	-	0.21 (0.02)	0.227	0.003	0.008	29.9	0.196	0.396	0	0.970 (0.025)	0.488 (0.003)	0.180 (0.002)	0.51 (0.01)	1.49 (0.04)	0.73 (0.02)	-	0.38	1.301 (0.002)
50 μM	1.509	0.698	0.186	-	-	0.22 (0.02)	0.227	0.003	0.008	31.3	0.196	0.396	0	1.010 (0.025)	0.501 (0.003)	0.180 (0.002)	0.62 (0.02)	1.88 (0.05)	0.92 (0.02)	-	0.38	1.238 (0.001)

$C_1 = 0.626 \pm 0.01$, and $C_2 = 0.520 \pm 0.03$. C_3 is associated with the freely rotating state of the dye and is fixed to zero.

For R1inv-R2inv the results for rotational correlation times are similar, here we find a global fit yields $\theta_1 = 0.222 \pm 0.005$ ns, $\theta_2 = 0.002 \pm 0.001$ ns and $\theta_3 = 0.007 \pm 0.001$ ns; individual fits for rotational lifetimes of Cy3 shows no systematic change with [Rop]. In comparison with rotational correlation lifetimes of R1inv-R2inv-C complex, here the lifetimes are shorter which suggests more freedom for the fluorophores. In these fits the rotational lifetime of RNA at different [Rop] are fixed to be same as R1inv-R2inv-C, this is because we do not expect the difference in terminal base pairs to change the overall tumbling of the RNA molecule with Rop binding. C_is were globally fitted across all Rop concentrations, giving: $C_1 = 0.206 \pm 0.007$, and $C_2 = 0.405 \pm 0.007$. C_3 is fixed to zero.

For FRET labeled molecules, FRET efficiency is typically found using [55]

$$\langle E \rangle = 1 - \frac{\tau_{DA}}{\tau_D} \tag{3.7}$$

where τ_{DA} is lifetime of quenched donor in presence of acceptor and τ_D is lifetime of donor in absence of acceptor. We also report here on the apparent change in FRET calculated separately from each of the three dye lifetimes, since this allows us to separate angular changes in structure from distance changes. We also calculated FRET using the change in the average donor lifetime.

The fluorescence polarization anisotropy decay of Cy3 on FRET labeled R1inv-R2inv-C and R1inv-R2inv was measured as a function of [Rop], and the results were fit with the model described by Eqs. 2.16a and 2.16b using the measured IRFs. There are 7 fixed parameters in this fit: τ_{iD}, θ_i, ϕ, C_i, α; the values for these parameters are taken from the donor-only fits. The constraints on the F_{iD}'s, mean that there is only one overall amplitude to fit. Amplitudes and τ_i's are fit separately for every data set.

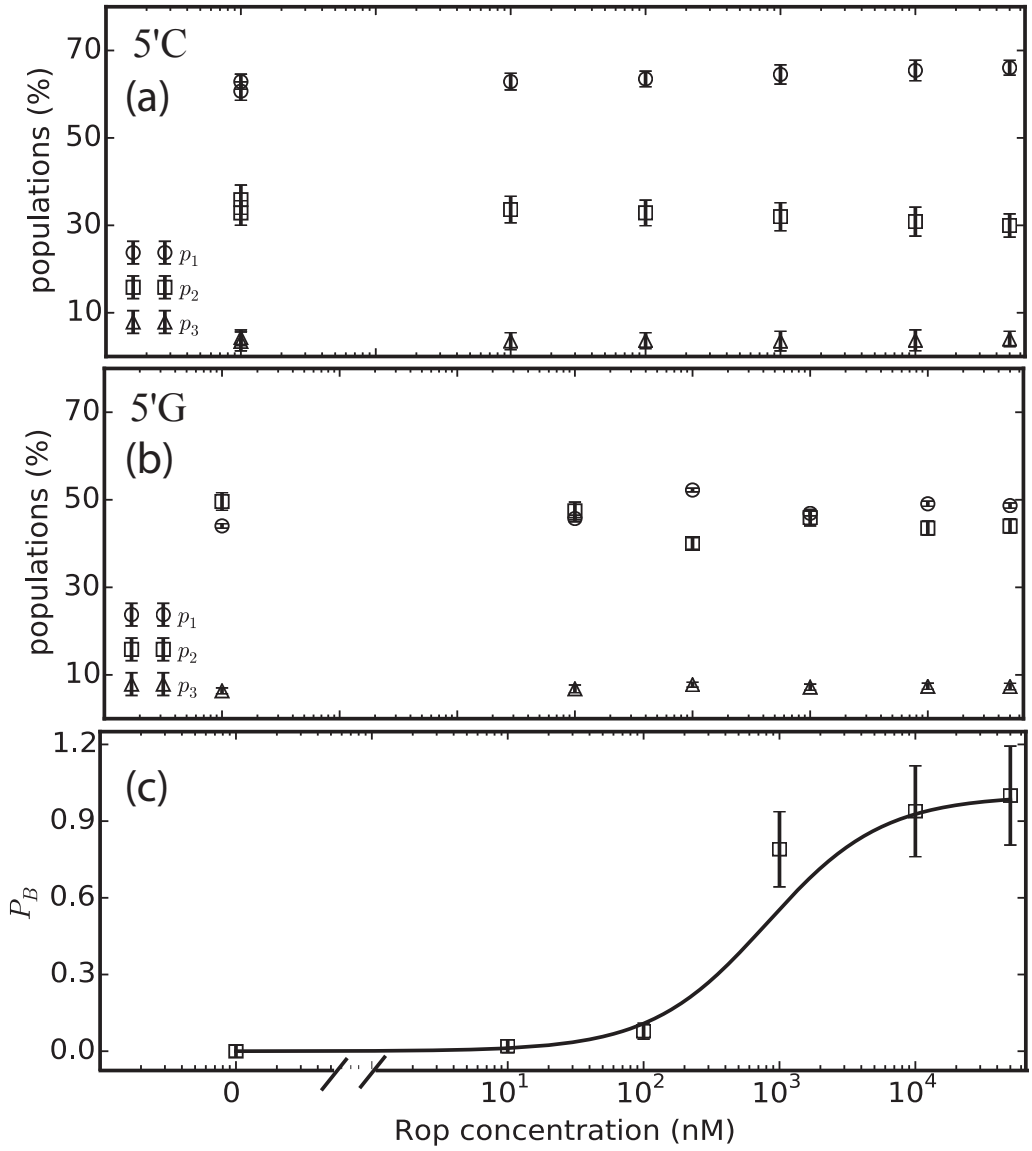

Figure 3.8. Time-resolved fluorescence lifetime fit results for R1inv-R2inv-C and R1inv-R2inv donor only data. Populations (p_1, p_2, p_3) corresponding to the three fluorescence lifetimes of Cy3 on RNA, for (a) R1inv-R2inv-C (b) R1inv-R2inv. (c) Population of bound RNA at different [Rop] for both 5′C and 5′G labeled R1inv-R2inv constructs, and the corresponding fit to it using a single site equilibrium binding equation (Eq. 3.5). The result of fit gives K_d= 779.3±191.8 nM.

The results for R1inv-R2inv-C and R1inv-R2inv are shown in Figs. 3.9(a) and 3.9(b) respectively. The result of the fits is reported in Table. 3.2 and Table. 3.5.

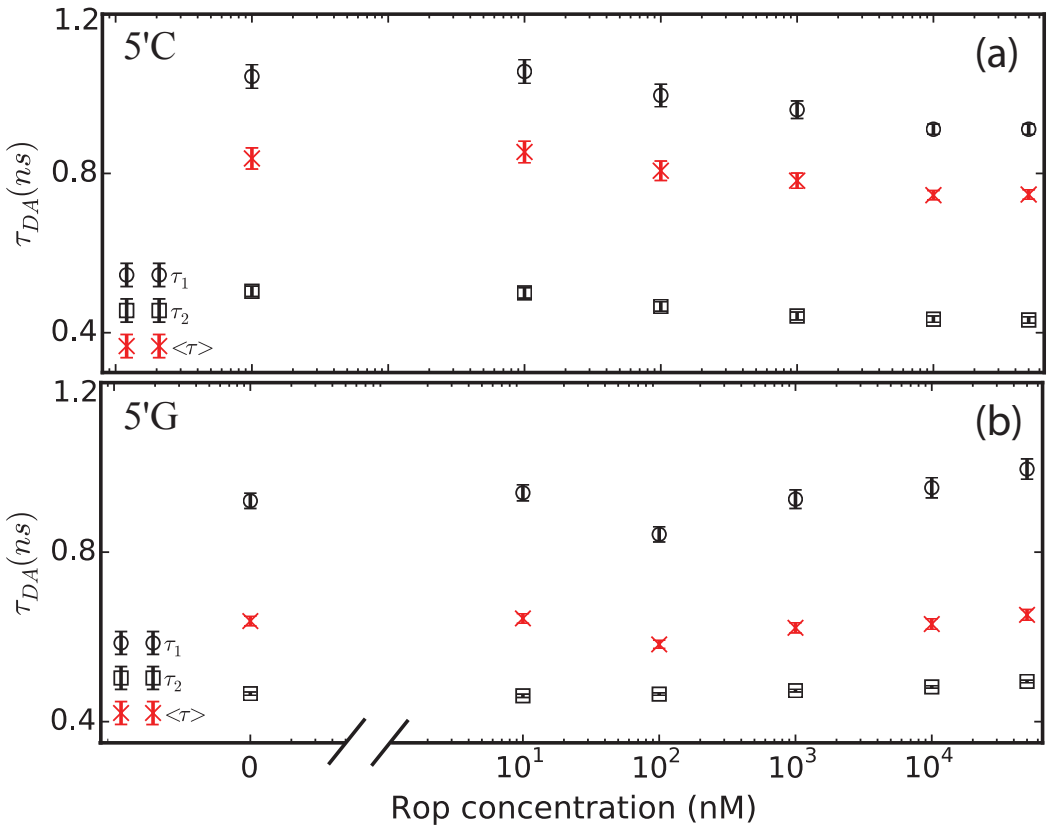

Figure 3.9. Fluorescence lifetimes τ_1 and τ_2 for quenched Cy3 in presence of Cy5 as a function of [Rop], for (a) R1inv-R2inv-C (b) R1inv-R2inv. Intensity weighted lifetimes are shown with red crosses in both (a) and (b). τ_3 is globally fitted across all [Rop] and found to be 0.136 $\pm$ 0.002 ns for R1inv-R2inv-C and 0.176 $\pm$ 0.002 ns for R1inv-R2inv.

For R1inv-R2inv-C (3.9(a)), τ_1 and τ_2 show a shift with [Rop]. Since τ_3 doesn't show a systematic change with [Rop], it is globally fitted across all concentrations of Rop and found to be 0.136 $\pm$ 0.002 ns. For R1inv-R2inv (3.9(b)), τ_1, τ_2 show no systematic change with Rop binding, although there is weak evidence for a small increase in τ_2 with Rop binding. For consistency τ_3 is globally fitted and found to be 0.176 $\pm$ 0.002 ns.

Fig. 3.10(a) shows apparent FRET efficiencies for R1inv-R2inv-C measured from the two longest lifetimes as a function of [Rop]. E_1 and E_2 increase with Rop binding,

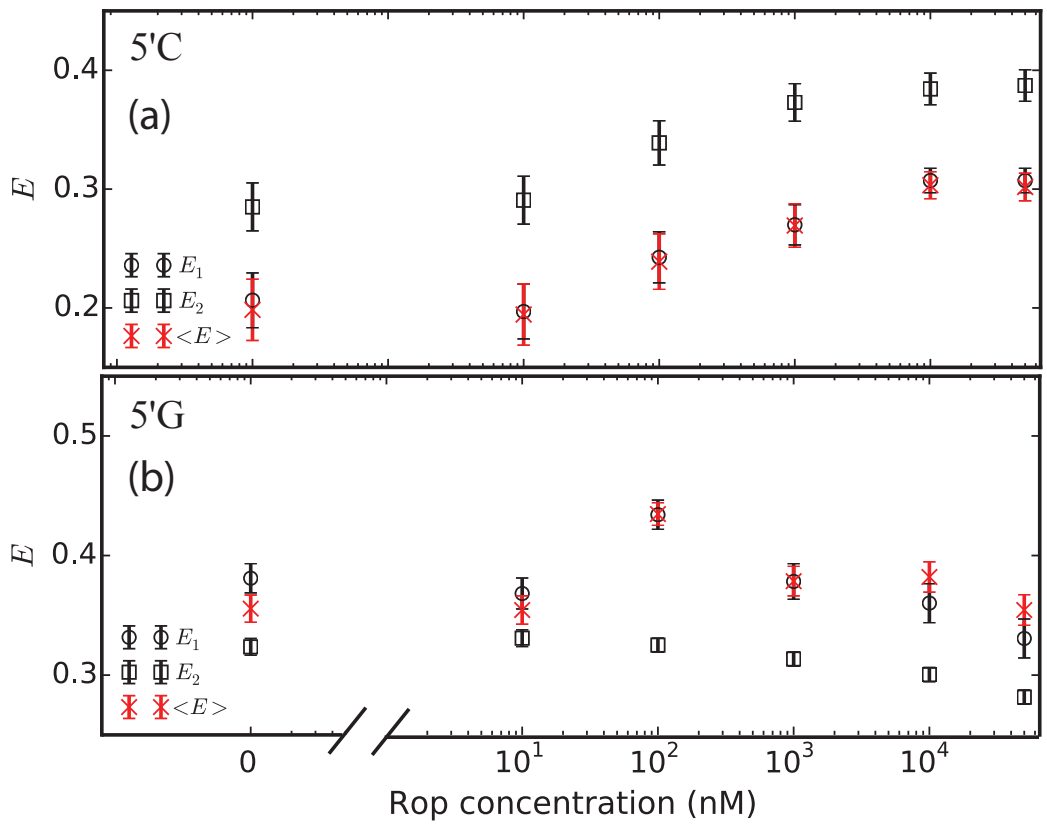

Figure 3.10. Measured FRET from fluorescence lifetimes as a function of [Rop]. (a) R1inv-R2inv-C (b) R1inv-R2inv. E_1 (squares) and E_2 (circles) are measured from the two longest lifetimes, $\langle E \rangle$ (red cross) is measured from $\langle \tau_D \rangle$ and $\langle \tau_{DA} \rangle$.

and E_3 is found to be 0.295 $\pm$ 0.02 for all [Rop]. Average FRET efficiency calculated from the average lifetimes (Eq. 3.7) shows a similar increase with [Rop]. The data for average FRET efficiency is fitted to a single-site binding curve (Eq. 3.6), with the values of FRET at 50 μM Rop and K_d as the free parameters. This fit gives: K_d= 289.6 $\pm$ 120.9 nM and FRET([Rop]=50 μM)= 0.303 $\pm$ 0.004 (Fig. 3.11). Therefore a 0.105 overall increase in FRET upon Rop binding is found.

For R1inv-R2inv, E_1, which is expected to report more about the orientation changes in structure, shows no systematic change with [Rop] (Fig. 3.10(b)), while E_2 which is more sensitive to distance changes in structure shows a very small decrease

in FRET with [Rop]. This might suggest that there is a small increase in distance with Rop binding.

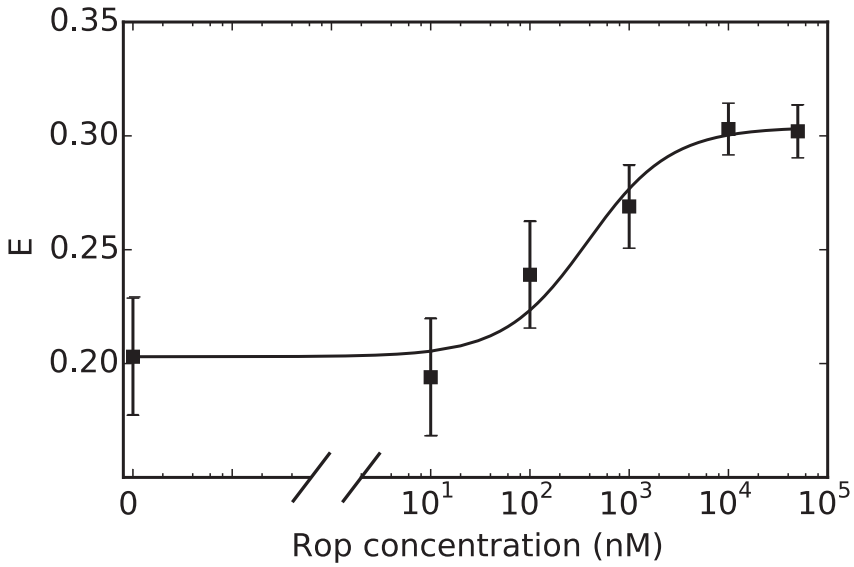

Figure 3.11. Average FRET efficiency for 10 nM R1inv-R2inv-C at different Rop concentrations. Solid line shows the best fit binding curve (Eq. 3.6), giving K_d= 289.6 ± 120.9 nM and a change in FRET of 0.105.

The relatively large shift in the larger fluorescent lifetime, and absence of any shift in the shorter lifetime, can be taken as additional evidence that the observed change is FRET is due to a change in the angular relation of the dyes, and not the distance between the dyes. Attached at the 5′ terminus of duplex nucleic acids, they develop additional, longer lifetimes that are associated with, *e.g*, more "rigid" base-stacked conformations. That the longer-lifetime component reports on a change in FRET while the shorter lifetime – preumably freer-rotating – component does not, is consistent with a change in angle between the dyes. The longer rotational lifetimes and the larger population of the longest fluorescence lifetime for Cy3 on 5′C terminus, suggests less rotational freedom for dyes on a 5′C terminus in compare with 5′G; therefore the R1inv-R2inv-C complex should have better sensitivity to angular

changes in structure. This can explain the observed shift in FRET with Rop binding for R1inv-R2inv-C and not for R1inv-R2inv complex. As I will show in chapter 4, this will be consistent with a change in twist of the RNA complex.

3.4 Results and Analysis: FCS

To rule out artifacts that might be associated with Rop-dependent dye photophysics, we used fluctuation correlation spectroscopy (FCS) on donor-only and acceptor-only labeled RNA. FCS data were acquired under the same conditions as FRET data, except that R1inv-R2inv-C was labeled with either Cy3 on R1inv or Cy5 on R2inv but not both. No significant change in kinetic terms attributed to dye photophysics (triplet and isomerization lifetime and amplitude) was observed as a function of Rop concentration, indicating that changes in FRET can not be due to changes in photophysics of dyes with Rop binding.

Fig. 3.12(a) shows FCS data and the corresponding fit to this data for 10 nM R1inv-R2inv complex labeled with Cy3 (10 nM) with 0 nM, 100 nM and 10 μM Rop concentrations. The fit model is given in Eq. 2.27. A global fit was performed onFCS data by taking τ_T and τ_I as the global fit parameters between the three autocorrelation functions and fitting for T, I and N of each curve separately. The results for fit parameters are provided in Table 3.6. Diffusion time for all three measurements is in the order of 300 μs, with $\tau_T = 4.5 \pm 0.3$ μs and $\tau_I = 121 \pm 4.9$ μs. Triplet and isomerization relaxation times are globally fitted. The fact that the global fits give better fit results, makes this assumption valid: binding of Rop protein does not change photophysics significantly. Residuals corresponding to the fits shown in panel (b-d) of Fig. 3.12 indicates the goodness of fit.

Fig. 3.13(a) shows FCS data and the corresponding fit to this data for R1inv-R2inv complex labeled with Cy5 (10 nM) with 0 nM, 100 nM and 10 μM Rop concentration. Similar to the donor only data, a global fit was performed on these ACFs by taking

τ_T and τ_I as the global fit parameters between the three autocorrelation functions and fitting for T, I and N of each curve separately. The diffusion times for these data are slightly larger than the donor only data but still in the order of 300 μs, this is due to the difference in the size of the detection volume as a result of excitation with longer wavelength (647 nm Ar-Kr laser).

Table 3.6. Results of the global fit to the FCS data for donor only and acceptor only R1inv-R2inv-C at three different concentrations of Rop protein. τ_T and τ_I are the global fit parameters and find to be $\tau_T = 4.5 \pm 0.3$ μs and $\tau_I = 121 \pm 4.9$ μs for R1invCy3-R2inv-C and $\tau_T = 10.2 \pm 0.3$ μs and $\tau_I = 56.9 \pm 1.6$ μs for R1inv-R2invCy5-C. τ_D, N, A_T and A_I are the other fit parameters.

	R1invCy3-R2inv-C				R1inv-R2invCy5-C			
[Rop] (μM)	τ_D (μs)	$\langle N \rangle$	T	I	τ_D	$\langle N \rangle$	A_T	A_I
0	302.6 ± 5.3	0.922 ± 0.013	0.230 ± 0.009	0.262 ± 0.01	344.14 ± 2.29	1.161 ± 0.005	0.243 ± 0.004	0.293 ± 0.004
0.1	326.3 ± 5.0	0.701 ± 0.008	0.229 ± 0.009	0.210 ± 0.009	457.51 ± 6.19	1.129 ± 0.008	0.227 ± 0.007	0.414 ± 0.005
10	317.5 ± 4.9	0.716 ± 0.008	0.236 ± 0.01	0.190 ± 0.01	342.46 ± 2.65	0.841 ± 0.004	0.236 ± 0.005	0.200 ± 0.006

FCS was also used in an attempt to investigate binding of Rop to the R1inv-R2inv-C labeled with both donor and acceptor. We found no evidence for contribution of another kinetic term that might be attributed to Rop binding: however, even if there are kinetics on a timescale suitable for observation with FCS, the small change in donor brightness necessary to account for the small change in FRET efficiency may be too small to observe in FCS. Results are shown in Fig. 3.14 and Table 3.7.

There was also no clear evidence of a change in diffusion time upon Rop binding. Given the small size of Rop, this is also not surprising. There should be a factor of 1.6 change in diffusion time in order to be resolvable by FCS [47]. This corresponds to a factor of ∼4-8 change in molecular weight of complex. Molecular weight for R1invCy3-R2invCy5 is 13.5kDa, and molecular weight for Rop is 15kDa, therefore the change in molecular weight with protein binding is not large enough to be resolvable in FCS.

In performing all these fits the aspect ratio (ω) for the focal volume is fixed to 8.3. ω= 8.3 is found by using a calibration sample, here I used TMR (tetramethylrhodamine) which has a known diffusion coefficient of 280 $\mu m^2/s$ [88]. ACF for TMR was measured at three different concentrations of 5 nM, 10 nM and 20 nM. These

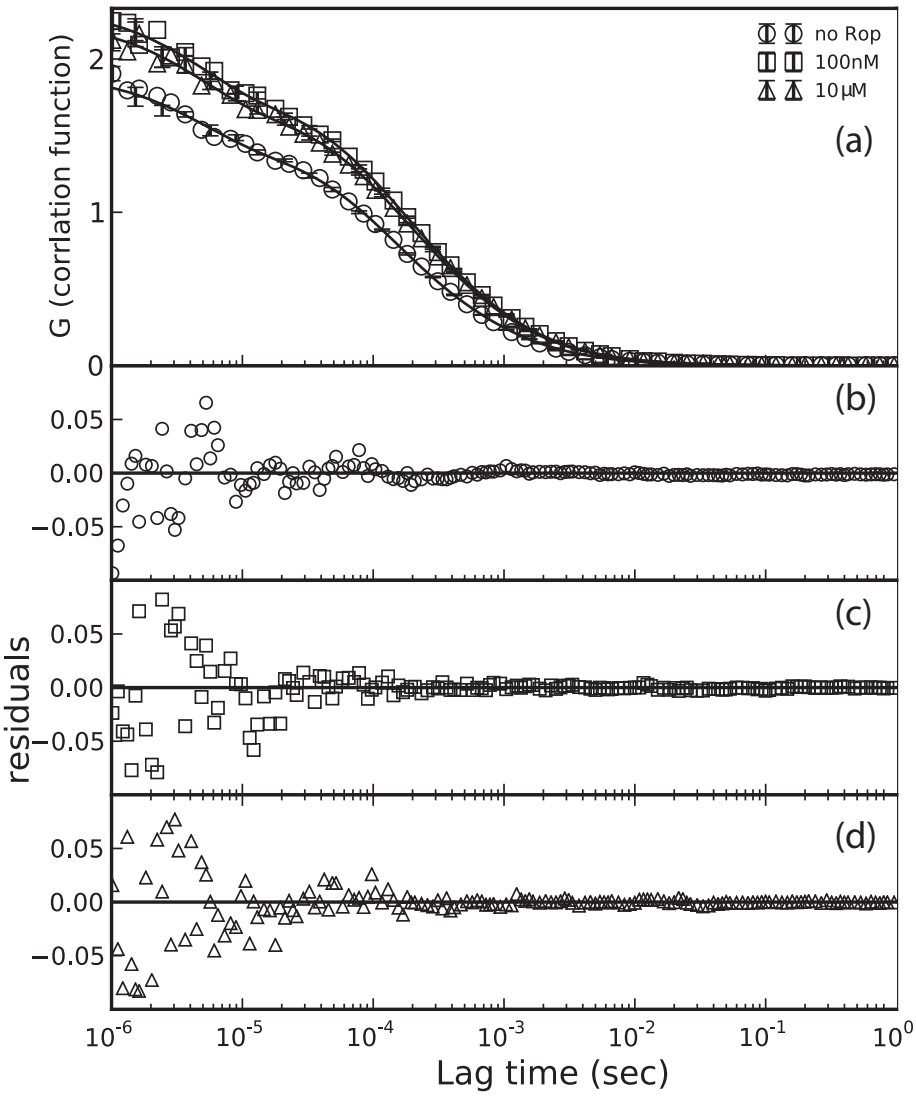

Figure 3.12. Global fit to ACFs for donor-only R1inv-R2inv-C (a) Autocorrelation (ACF) functions (symbols) and corresponding fits (black lines) for 10 nM R1inv-R2inv-C labeled with Cy3-only at 0 (circle), 100 nM (square) and 10 μM (triangle) Rop. Global fit to the ACFs gives $\tau_T = 4.5 \pm 0.3$ μs and $\tau_I = 121 \pm 4.9$ μs with $\chi^2 \approx 1.6$. The result of the fit for the other fit parameters (N, τ_D, A_T and A_I) are provided in Table. 3.6. (b-d) Residuals corresponding to the fits in (a).

ACFs were fitted using global parameters τ_D and τ_T and ω; number of molecules in volume (N) and fraction of triplet (T) was fitted individually for each plot. τ_D and

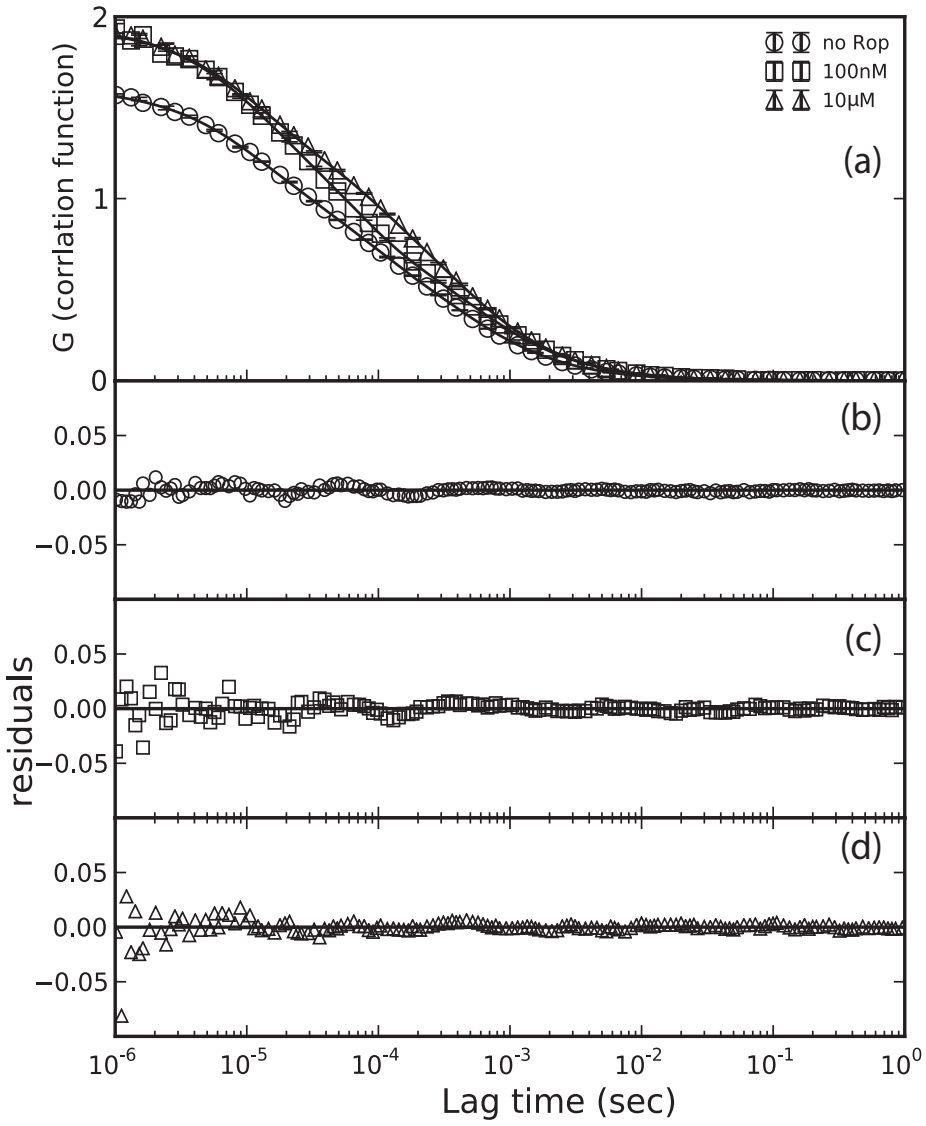

Figure 3.13. Global fit to ACFs for acceptor-only R1inv-R2inv-C.(a) Autocorrelation (ACF) functions (symbols) and corresponding fits (black lines) for 10 nM R1inv-R2inv-C labeled with Cy5-only at 0 μM (circle), 100 nM (square) and 10 μM (triangle) Rop. Global fit to the ACFs gives $\tau_T = 10.2 \pm 0.3$ μs and $\tau_I = 56.9 \pm 1.6$ μs with $\chi^2 \approx 1.1$. The result of the fit for the other fit parameters (N, τ_D, A_T and A_I) are provided in Table. 3.6. (b-d) Residuals corresponding to the fits in (a).

τ_T were found to be 79.6 $\pm$1.8 μs and 11.1 $\pm$1.4 μs, respectively. This results in: r_0= 0.3μm, z_0= 2.5μm, and V_{eff}= 0.3 fL.

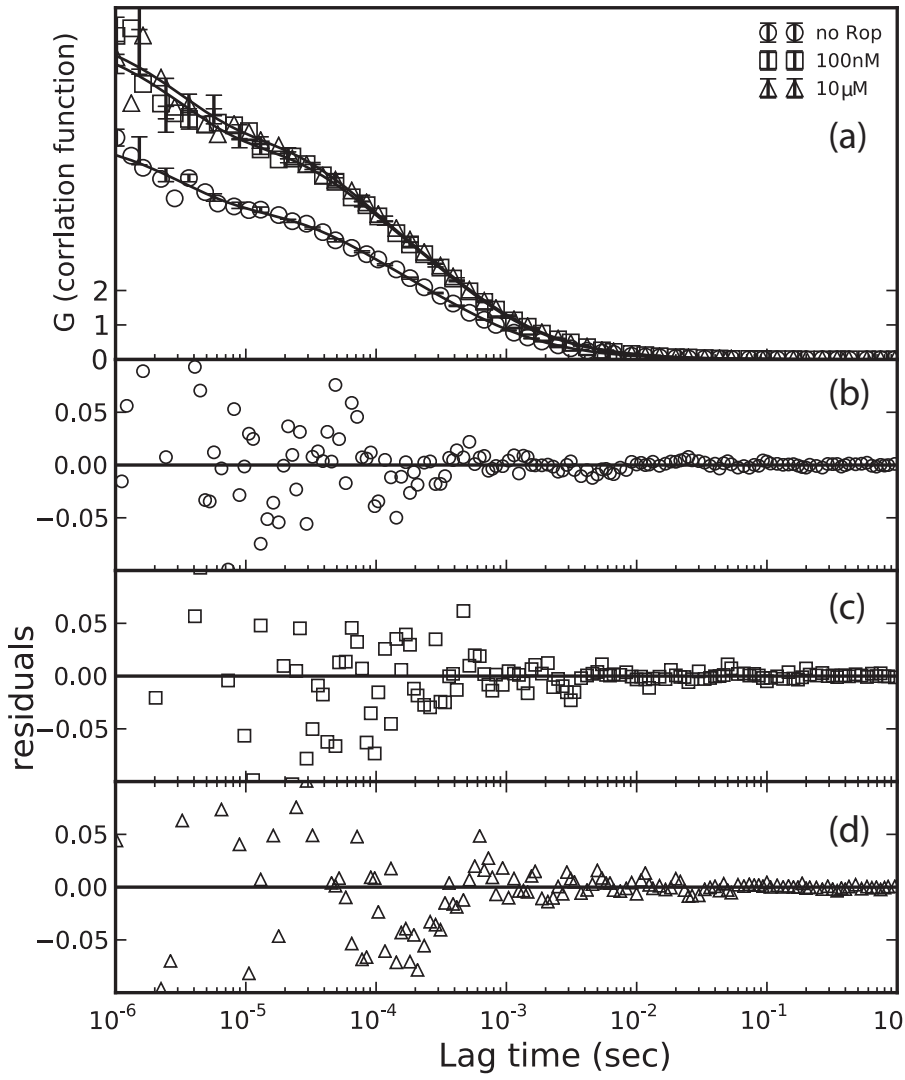

Figure 3.14. Global fit to ACFs for donor-acceptor labeled R1inv-R2inv-C. (a) Autocorrelation (ACF) functions (symbols) and corresponding fits (black lines) for 200 pM R1inv-R2inv-C labeled with Cy3 and Cy5 at 0 μM (circle), 100 nM (square) and 10 μM (triangle) Rop. Global fit to the ACFs gives $\tau_T = 3.0 \pm 0.3$ μs and $\tau_I = 65.3 \pm 3.4$ μs with $\chi^2 \approx 1.3$. The result of the fit for the other fit parameters (N, τ_D, A_T and A_I) are provided in Table. 3.7. (b-d) Residuals corresponding to the fits in (a).

Table 3.7. Results of the global fit to FCS data for R1invCy3-R2invCy5-C at three different concentrations of Rop protein. τ_T and τ_I are the global fit parameters and find to be $\tau_T = 4.5 \pm 0.3$ μs and $\tau_I = 121 \pm 4.9$ μs. τ_D, N, A_T and A_I are the other fit parameters.

	R1invCy3-R2invCy5-C			
[Rop] (μM)	τ_D (μs)	$\langle N \rangle$	A_T	A_I
0	332.7 ± 3.5	0.281 ± 0.002	0.29 ± 0.02	0.228 ± 0.007
0.1	332.5 ± 3.8	0.195 ± 0.002	0.30 ± 0.02	0.224 ± 0.01
10	352.6 ± 4.4	0.197 ± 0.002	0.29 ± 0.003	0.266 ± 0.01

CHAPTER 4

MODELING

To understand the structural change that gives rise to the observed FRET data, we first calculated FRET for a set of static model structures, using MD simulations to account for the dynamics of the dyes. The details about the MD procedure can be found in Appendix B. The models used were the eight known minimized energy structures [59], which vary widely in bend and twist and to a lesser extent in the end-to-end distance. The use of these structures therefore permits us to investigate any trends in FRET, particularly with bend or twist of the complex.

The dye trajectories were determined from 300 ns molecular dynamic (MD) simulations of the dye-labeled R1inv-R2inv-G and R1inv-R2inv-C complexes. Results were stored every 1 ps. MD runs were completed with different initial conditions for the dyes and with and without NMR constraints applied to the RNA complex. The distance and relative angle of the dyes with respect to the the final base is summarized in the two dimensional histograms of Figs. 4.1 and 4.2, and the relative orientation of dyes with respect to each other is summarized in Fig. 4.3. Adding NMR restraints to the kissing complex made little difference to the final behavior of the dyes, as should be expected since there are no restraints on the dyes. Different initial positions for the dyes (stacked or unstacked) made a larger difference, especially for Cy5 on $5'$ terminal C, Figs. 4.1(b) and 4.2(b), but were still more similar than not. One run with dyes initially stacked was extended out to 2 μs with resulting histogram indistinguishable from that of Fig. 4.1.

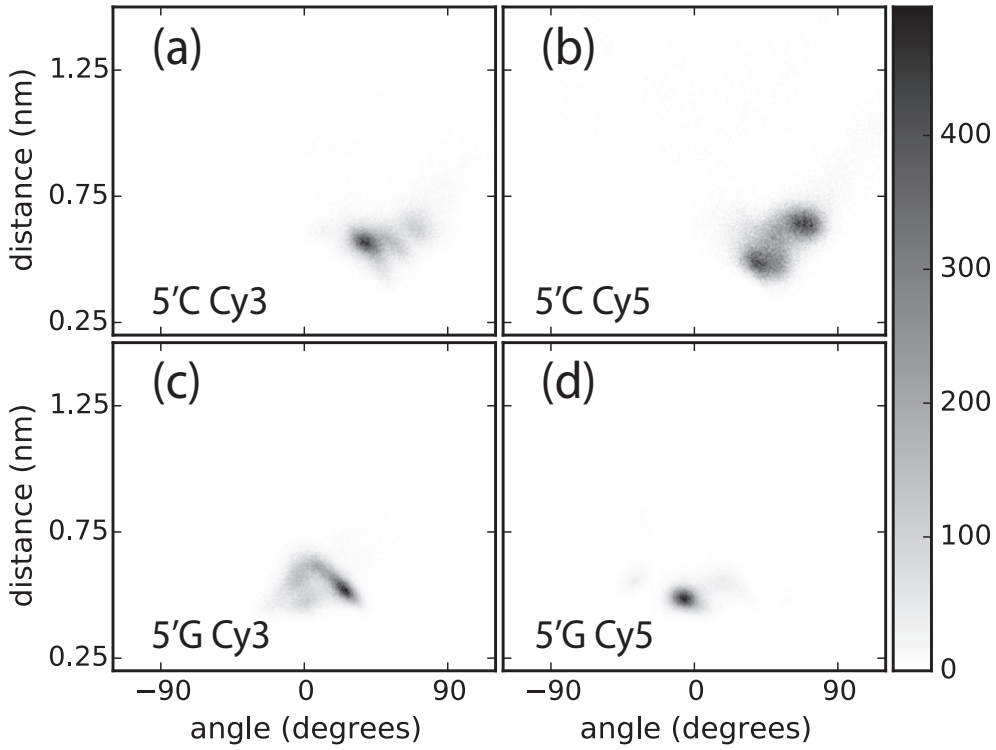

Figure 4.1. Distance/Angle 2D histogram of dyes attached to $5'C$ and $5'G$ terminal bases. For this simulation, no NMR restraints on the kissing complex were not used, and the dyes were initially stacked on the RNA. Distance is the distance between dye and nearest base pair and angle is the relative orientation for them.(a) Cy3 on 5′ terminal C, (b) Cy5 on 5′ terminal C, (c) Cy3 on 5′ terminal G, (d) Cy5 on 5′ terminal G.

For the MD simulations represented by Figs. 4.1 and 4.2, the dye trajectories with respect to the terminal base-pairs were recorded and used to calculate FRET for each of the eight underlying RNA kissing structures [59]. In these calculations, the coordinates of the dyes with respect to the terminal base-pair in each MD frame were mapped onto the eight static RNA kissing structures. This process gave 16 sets of dyes trajectories, one for each of the two simulated structures (R1inv-R2inv with 5′G attached dyes, and R1inv-R2inv-C with 5′C attached dyes) mapped onto each of the

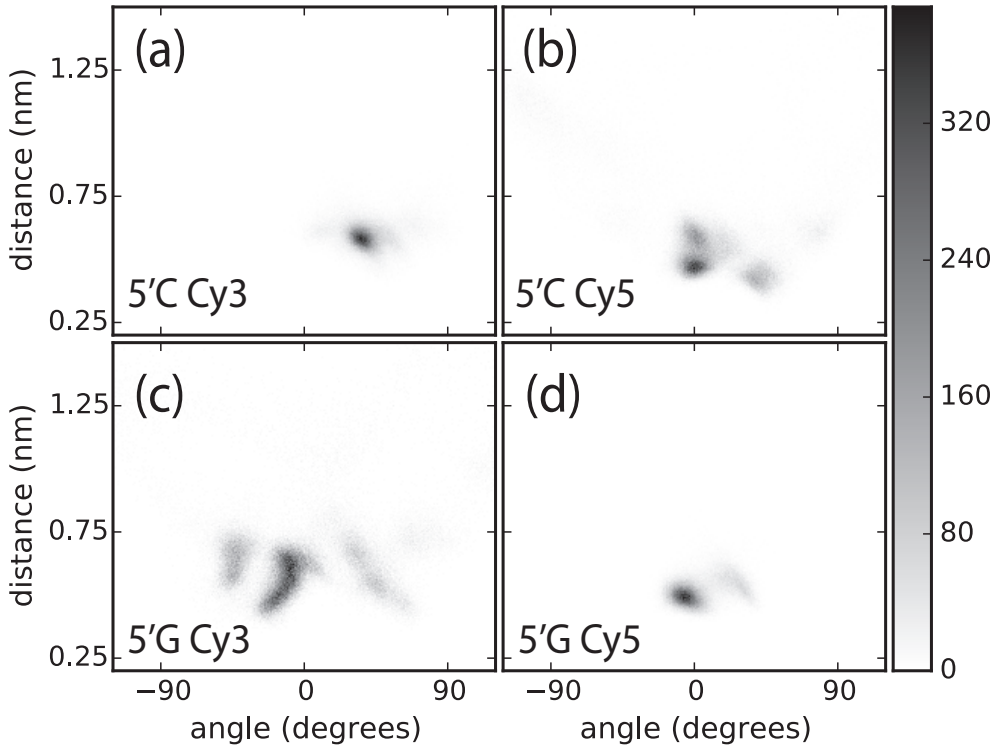

Figure 4.2. Distance/Angle 2D histogram of dyes attached to $5'C$ and $5'G$ terminal bases. For this simulation, NMR restraints [28, 29, 73, 72] was used. Distance is the distance between dye and nearest base pair and angle is their relative orientation in the plane of the base pair. (a) Cy3 on $5'$ terminal C, (b) Cy5 on $5'$ terminal C, (c) Cy3 on $5'$ terminal G, (d) Cy5 on $5'$ terminal G.

eight kissing structures, which were then integrated to calculate FRET as described below.

This should be adequate to investigate *trends* in FRET with changes in structure if RNA structural fluctuations about each minimized energy state are small and fast compared to the lifetime of the donor dye (≈ 1 ns). The dynamics of the dyes on the RNA do not satisfy these requirements [66] and so are dealt with explicitly using this model.

The 16 dye-pair trajectories differed in the relative positions and orientations of the dyes because of the differences in the bend and twist of the underlying RNA

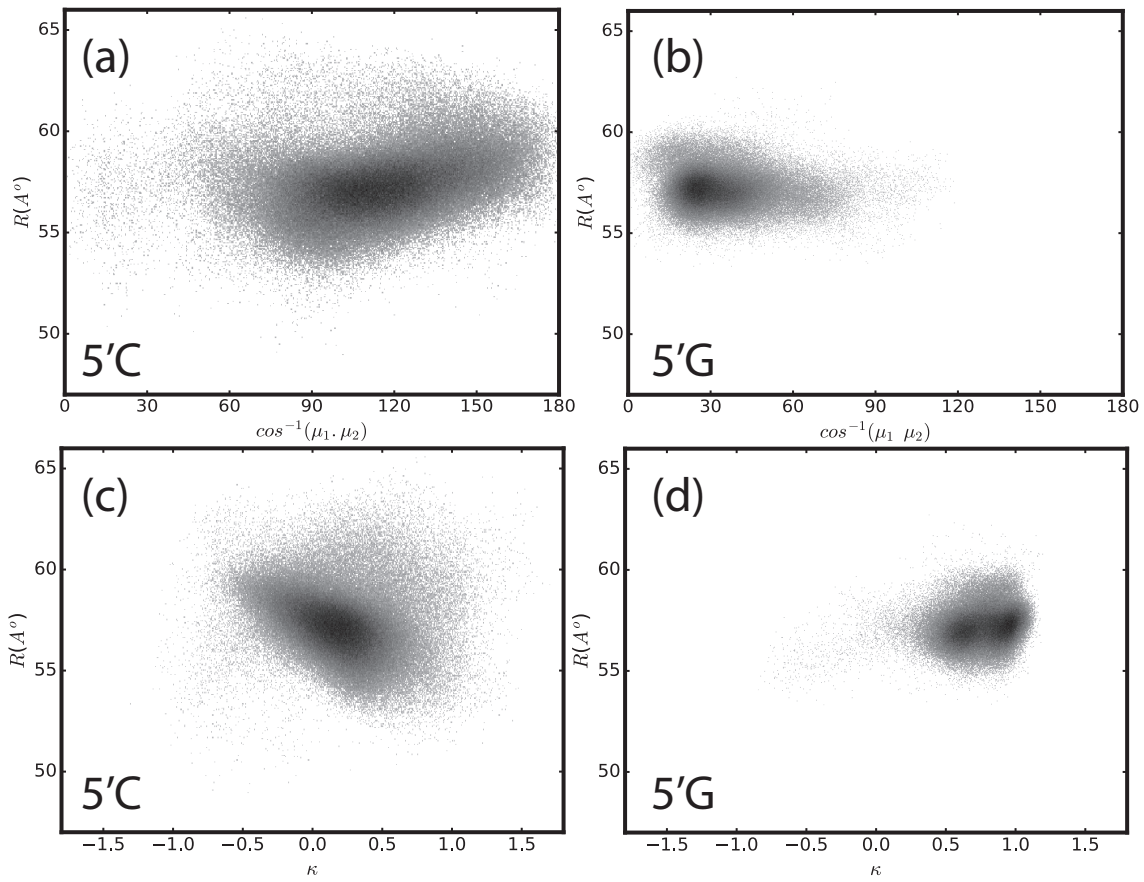

Figure 4.3. R *vs.* $cos^{-1}(\mu_1.\mu_2)$ 2D histograms for structure number 3 of the eight structures calculated from MD trajectories, for (a) 5′C, (b) 5′G. R *vs.* κ 2D histograms for structure number 3 of the eight structures calculated from MD trajectories, for (c) 5′C, (d) 5′G.

structure, and because of differences in the positions of 5′C and 5′G on the RNA. The trajectories are described by the interdye distance, R, and the orientational factor

$$\kappa = (\hat{\mu}_1 \cdot \hat{\mu}_2) - 3(\hat{\mu}_1 \cdot \hat{R})(\hat{\mu}_2 \cdot \hat{R}), \tag{4.1}$$

here $\hat{\mu}_1$ and $\hat{\mu}_2$ are the dye transition dipole unit vectors and $\hat{R}$ is the unit vector describing the distance from donor dye to acceptor dye. An example of trajectories for $\hat{R}$ and κ^2 and their histograms is shown in Fig. 4.4.

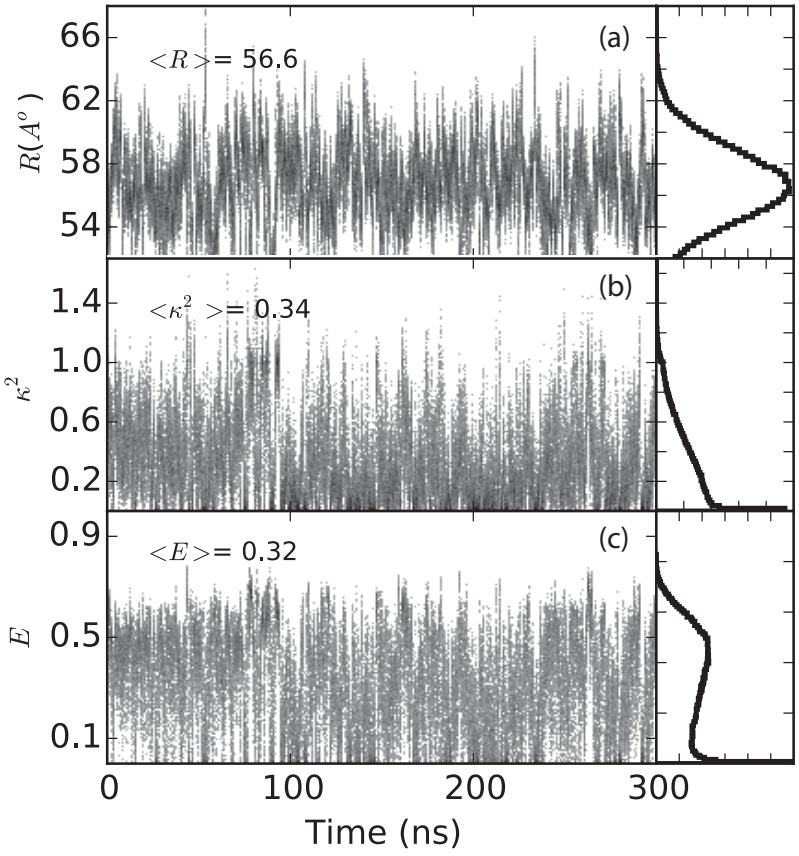

Figure 4.4. Trajectories and histograms for $5'C$**:** (a) The distance R between the center of the the two dyes, and the corresponding histogram with $\langle R \rangle = 56.6 \pm 2.8$ $\mathring{A}$, (b) κ^2 and its histogram with $\langle \kappa \rangle^2 = 0.34 \pm 0.25$, (c) Instantaneous FRET (Eq. 2.2, E, and its histogram with $\langle E_{inst} \rangle = 0.32 \pm 0.17$

FRET was calculated as described by Gopich [42]. From the R and κ^2 trajectories, we determine $k_{ET} = k_D(\frac{R_F}{R})^6$, the rate of energy transfer at each 1 ps time step, where ${R_F}^6$ is proportional to κ^2 and k_D is the decay rate of donor fluorescence [21, 54] (k_D=$1/\tau_D$= 1 ns^{-1}). The trajectory for rate of energy transfer is used to calculate average value of FRET by repeated integration over segments of the trajectory [14, 42]. We sampled 50000 starting times and integrated over the next 15 ns of the

trajectory from each start point, to obtain:

$$\langle E \rangle = 1 - k_D \int_0^{+\infty} I(\tau)\ d\tau, \tag{4.2}$$

where

$$I(\tau) = \left\langle exp(-\int_0^{\tau} [k_D + k_{ET}(t)]\ dt) \right\rangle. \tag{4.3}$$

We applied this technique to find $\langle E \rangle$ for each of the 16 structures: the results, which were generated using $R_0 = \sqrt[6]{\frac{2}{3\kappa^2}} R_F = 5.8$ nm [66], are given in Table. 4.1, along with the structural parameters that describe each structure.

It should be apparent from Figs. 4.1 and 4.2 that direct determination and integration of dye trajectories is necessary here: for example, the dyes are clearly not freely-rotating. Indeed, the minimal rotational freedom of the dyes is what gives sensitivity to twist. More generally, correlations between R and κ^2, and structural fluctuations of the dyes with respect to the RNA that have a timescale similar or longer than the donor fluorescence lifetime (≈ 1 ns) [66], make it necessary to use a complete description of the dye dynamics in the FRET calculation.

Table 4.1. Results of modeling FRET for each of the eight minimized energy RNA structures.

			R1inv-R2inv-C			R1inv-R2inv		
structure	bend angle($^\circ$)	twist angle($^\circ$)	$\langle R \rangle$	$\langle \kappa^2 \rangle$	$\langle E \rangle$	$\langle R \rangle$	$\langle \kappa^2 \rangle$	$\langle E \rangle$
1	96	4.4	58.1	0.25	0.27	57.4	0.91	0.58
2	82	-2.4	58.6	0.49	0.41	58.4	0.8	0.53
3	71	4.1	57.2	0.11	0.15	57.1	0.6	0.49
4	66	9.8	62	0.17	0.14	61.6	0.55	0.35
5	86	5.9	60.9	0.09	0.08	60.2	0.98	0.53
6	49	-1	55.1	0.17	0.26	55.3	0.76	0.6
7	64	-12.8	57.6	0.45	0.41	57.7	0.83	0.56
8	83	5.1	59.5	0.08	0.09	59.2	0.79	0.5

To understand which structural changes might account for the observed FRET data, we first plot $\langle E \rangle$ *vs.* $\langle R \rangle$, $\langle E \rangle$ *vs.* $\langle \kappa^2 \rangle$, and $\langle E \rangle$ *vs.* the bend and twist of the kissing complex, Fig. 4.5. The corresponding Pearson's coefficients, r, which characterize the linear correlation between two parameters, are given in the insets. Pearson's coefficients run from -1 to 1, with values near zero denoting no correlation and absolute values near 1 denoting a strong linear correlation.

Twist and bend angles of the eight minimized-energy structures [59] were determined using the nucleic acid conformational analysis program Curves+ [58], and are recorded in Table 4.1. The twist angle is the sum of the twist angles between base pair: twist angle modulo 360° gives the number of complete turns along the helix. Since the average twist angle of the minimized-energy structures for the R1inv-R2inv kissing complex corresponds to about 1.5 turns, we report the difference from 540° in Table. 4.1. A typical bent helical axis obtained by the program is shown in Fig. 1.2(c) in red. The bend angle is defined as the angle between the first and last segment of the helical axis: a bend angle of zero corresponds to a linear duplex. Note that the kissing structures have 47° range of bend and 23° range of twist.

For R1inv-R2inv-C, there is a very strong correlation, $r > 0.9$, between $\langle E \rangle$ and $\langle \kappa^2 \rangle$ for all MD runs, Fig. 4.5(a) and Fig. 4.6(a). There is also a correlation between $\langle E \rangle$ and $\langle \kappa^2 \rangle$ for R1inv-R2inv-G, but this correlation depends strongly on a single structure, number 4 in Table 4.1, that has the largest twist angle, largest inter-dye distance, and smallest FRET. The difference in the mean interdye distance $\langle R \rangle$ for the eight structures is relatively small, and there is a weaker negative correlation with $\langle R \rangle$ that is similar for both R1inv-R2inv and R1inv-R2inv-G (see particularly Fig. 4.6).

The substantial correlations between $\langle E \rangle$ and κ^2 confirm again that the dyes cannot be treated as fast, free rotators [66]. That κ^2 is near 2/3 for some of the

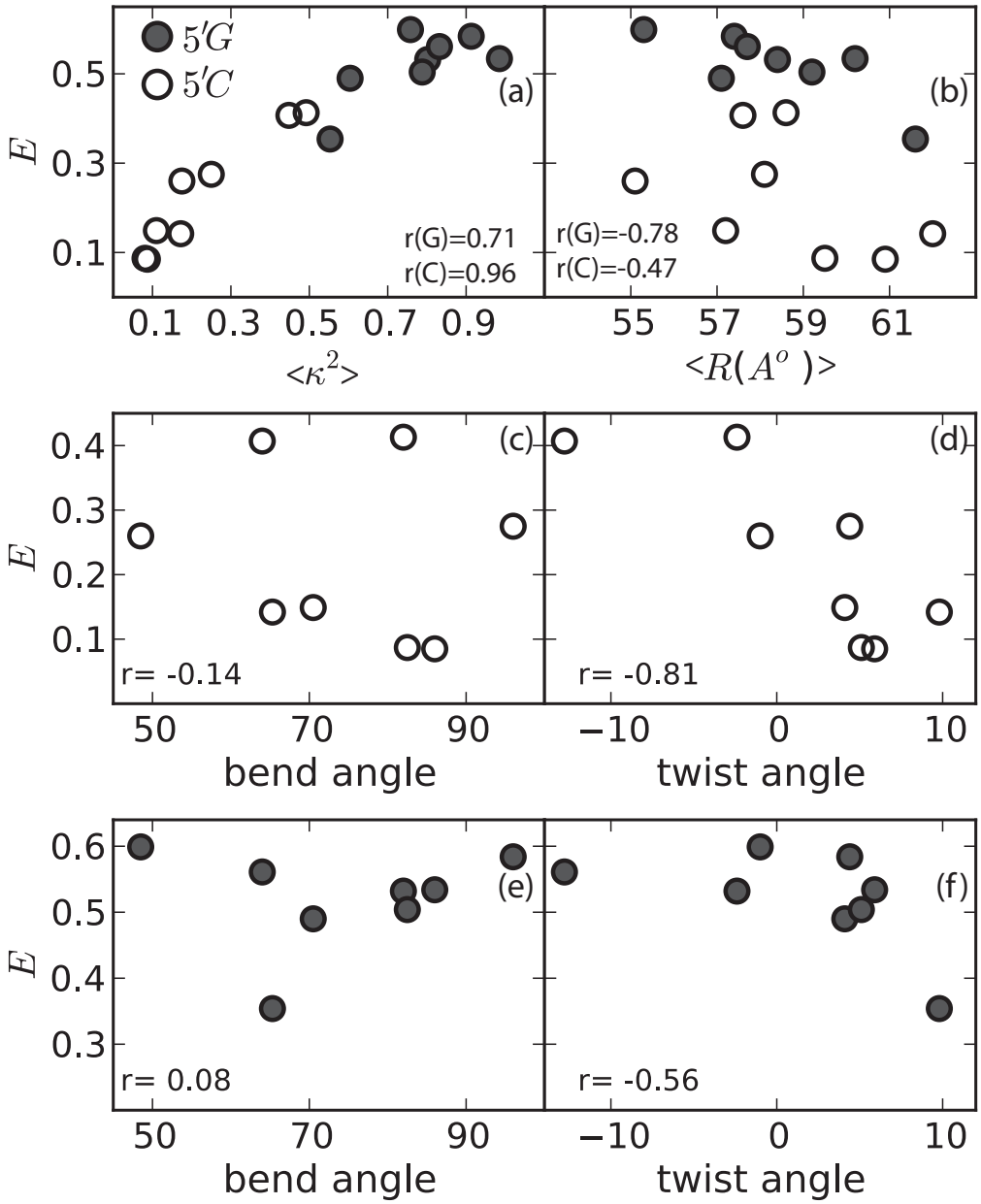

Figure 4.5. Results of modeling: of the R1inv-R2inv-C complex with dyes attached to the 5′ terminal C (open circles), and the R1inv-R2inv complex with dyes attached to the 5′ terminal G (filled circles). The panels show the predicted dependence of FRET efficiency on (a) κ^2 , (b) R, (c) bend angle and (d) twist angle.

structures is not an indication of free rotation, but rather related to the average relative orientation of the dyes for those structures.

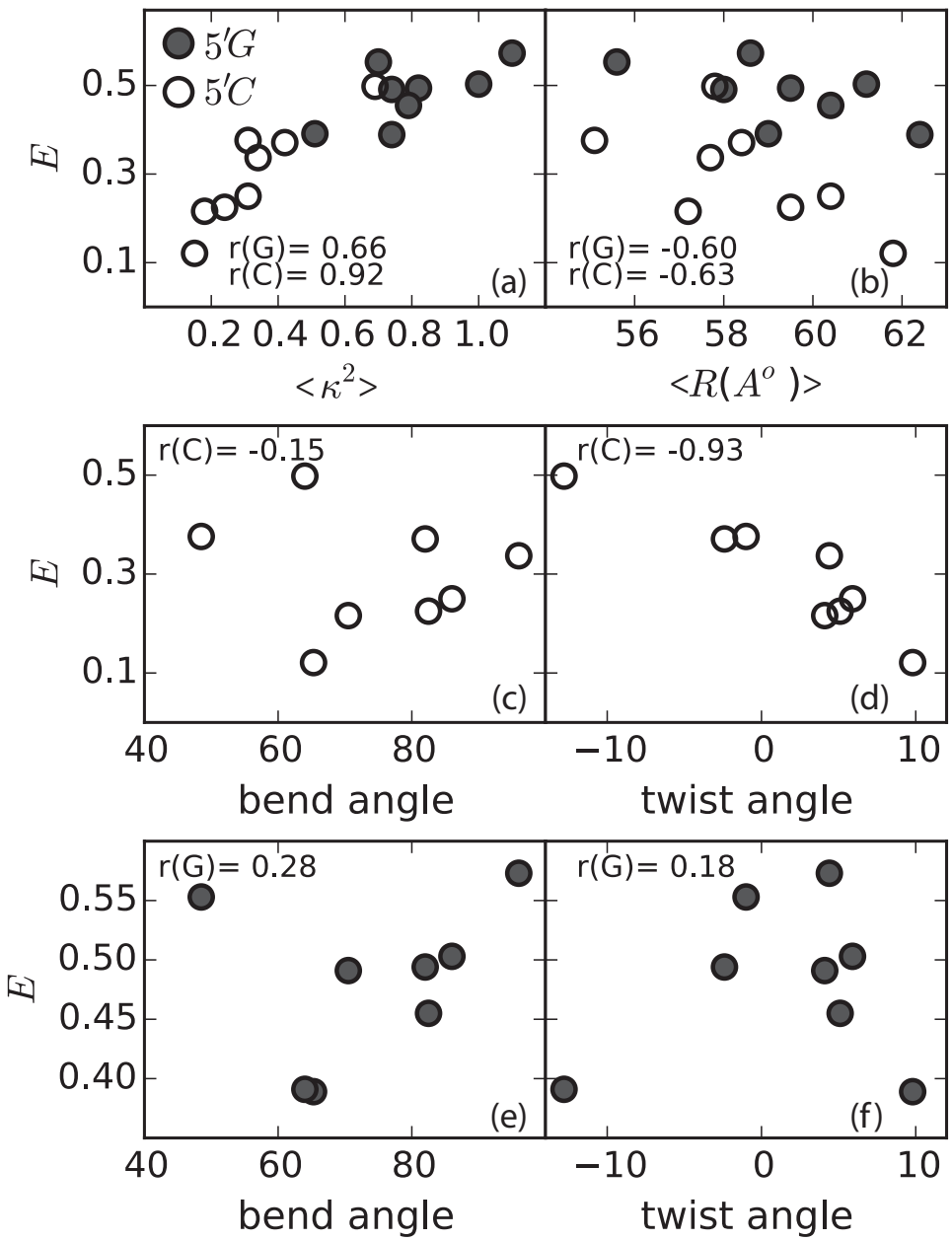

Figure 4.6. Results of Modeling for the second MD simulation with NMR constraints: for R1inv-R2inv-C complex with dyes attached to the 5′ terminal C (open circles), and the R1inv-R2inv complex with dyes attached to the 5′ terminal G (filled circles). The panels show the predicted dependence of FRET efficiency on (a) κ^2 , (b) R, (c) bend angle and (d) twist angle.

To which angle, then, should the observed change in FRET be attributed, and why is no or little change observed when the dyes are attached at a terminal 5′G? In

Fig. 4.5(c-f) and 4.6(c-f) we explore the correlations of $\langle E \rangle$ with bend and twist for the two kissing structures. The only decidedly significant correlation is between $\langle E \rangle$ and twist of the R1inv-R2inv-C complex, for which $r = -0.81$, -0.93 in the two MD runs. A smaller correlation between $\langle E \rangle$ and twist for R1inv-R2inv again depends strongly on a single structure, number 4 in Fig. 4.5. The correlation with bend angle is insignificant in both structures, despite the large range of bend angles, from 49° to 96° represented here. It is worth noting that a change in bend angle from 45° to 60° upon Rop binding, as suggested by Marino [61], also results in a 0.32 nm change in R. For freely-rotating dyes, we would expect to see a change in FRET, for both complexes, from 0.54 to 0.62 for this distance change.

The shift in FRET for the R1inv-R2inv-C structure, and the absence of shift for the R1inv-R2inv structure, can be attributed to the difference in the relative freedom of the dyes attached at a terminal 5′C or 5′G (Fig. 4.3). The fact that for R1inv-R2inv complex, dyes spend a large fraction of their time parallel with respect to each other ($\cos^{-1}(\mu 1.\mu 2)$ near zero and κ near 1), makes this complex to lose its sensitivity to angular changes in structure (Fig. 4.3 (b,d)). On the other hand, for R1inv-R2inv-C complex dyes are stacked on the RNA and are free to have different angles with respect to each other, which makes it more sensitive to angular changes in structure. Therefore if large changes in end-to-end distance of complex happens we would expect to resolve it with both $5'C$ and $5'G$ structures, while changes in orientation of structure are only resolvable by R1inv-R2inv-C complex.

To investigate the result of the change in twist or in other words the change in FRET, we artificially twist the coordinates of the last base pair around the helical axis, and recalculate FRET from the re-oriented dye trajectories and plot FRET as a function of twist angle for each of the eight minimized energy structures. This is illustrated in Fig. 4.7 for structure number three, with $\langle E \rangle = 0.15$. Modulation in FRET *vs.* twist angle is due to changes in κ^2 resulting from the helical twist.

For R1inv-R2inv (diamonds) in the range of twist angles (0 and -50°) that span a range greater than the twist for the eight structures, average FRET is near a maximum and doesn't change significantly with twist angle, in agreement with the data (Fig. 4.7(b)). In contrast, for R1inv-R2inv-C (squares), the somewhat different orientation of the dyes with respect to the final base pair result in a linear slope for FRET in the same range of twist angles (Fig. 4.7(b)). Average FRET for the unbound R1inv-R2inv-C structure (0.198) is shown with red circle and bound structure (0.303) with green circle. For this structure the 0.104 increase in FRET, observed in the experiment, with protein binding corresponds to $-24°$ change in twist angle. This $-24°$ change in twist angle for 5′-C structure corresponds to only a 0.029 change in FRET for 5′-G (shown with red triangles). For five of the eight minimized energy structures a change in twist of between $-20°$- $-20°$ was measured. FRET as a function of twist angle plots for the other structures are included in Appendix C.

We conclude that a decrease in twist could explain the shift in FRET upon Rop binding for the R1inv-R2inv-C structure. That there is smaller change in FRET for the R1inv-R2inv-G structure is consistent with its smaller correlation between $\langle E \rangle$ and twist. Changes in $\langle R \rangle$ between the eight proposed structures are not big enough to discern here, but if Rop binding resulted in a larger change in $\langle R \rangle$, we would see it in both structures. The 15° change in bend upon Rop binding proposed by Marino [61] would result in an end-to-end decrease of about 0.3 nm, which is probably not large enough for us to resolve here. So while our data are neutral regarding any change in bend upon Rop binding, they do show a change in $\langle E \rangle$ that is most likely explained by a decrease in the twist of the structure.

The best possible approach would use the change in FRET data as a constraint on the MD simulations of the bound complex, but as determining FRET requires integrating over a long trajectory, this needs very fast computers.

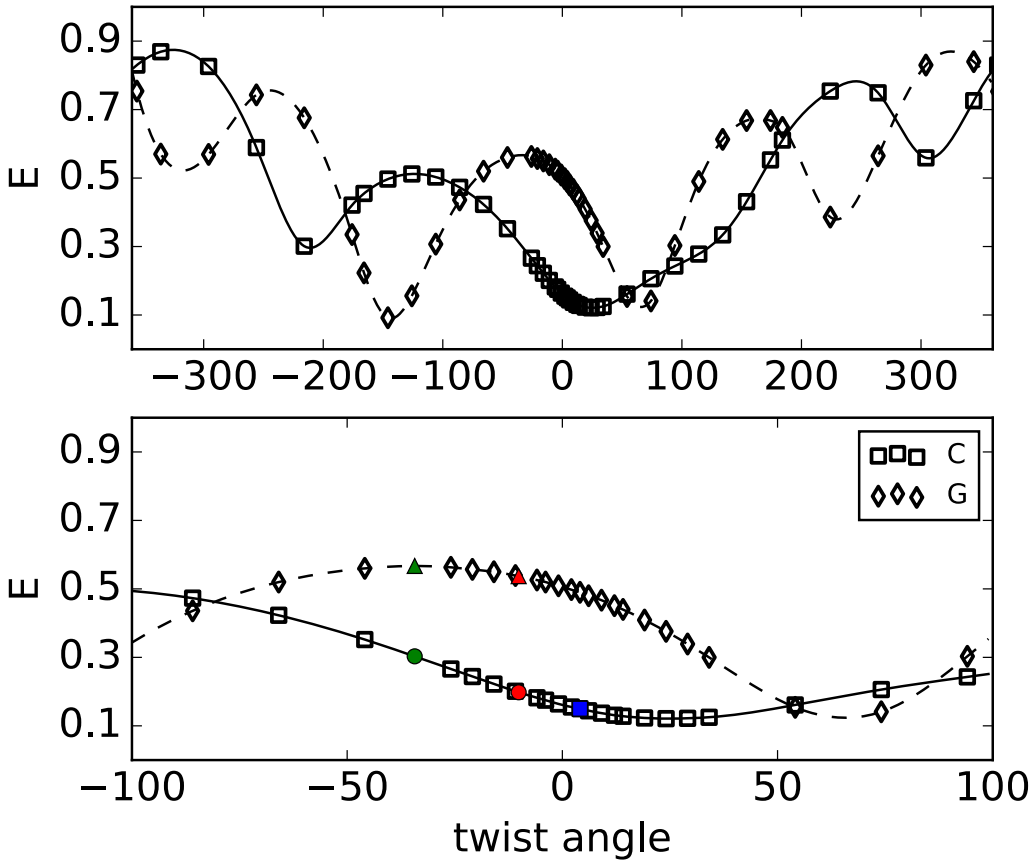

Figure 4.7. Calculated FRET at different twist angles for structure 3: (a) total twist from -360 to 360, (b) total twist from -100 to 100. Diamonds show FRET at each twist angle for 5′-G and squares for 5′-C construct. Dashed and solid lines are interpolated spline curves to the points for 5′-G and 5′-C respectively. In panel (b) the red circle and triangle show FRET for the unbound RNA (5′C=0.198 and5′G= 0.537), and the green circle and triangle shows FRET for the bound RNA (5′C=0.303 and 5′G= 0.567). The blue square represents twist angle for the initial untwisted structure.

It should be clear that while we do not expect the modeled values of $\langle E \rangle$ to be quantitative, we do expect that the general trends revealed by this method are valid. In short, both complexes show a correlation between $\langle E \rangle$ and FRET, but this correlation is more pronounced in R1inv-R2inv-C. A correlation between $\langle E \rangle$ and R is also predicted, and this correlation is similar for both complexes: if changes in R accounted for the observed change in FRET, we would see a similar shift for both

molecules. Our observation of a small change in FRET upon the addition of Rop for the R1inv-R2inv-C, but not R1inv-R2inv, is consistent with a change in twist, but not in R, of the Rop-bound complex. Because the RNA complex is not static, the observed change in FRET is small: for R1inv-R2inv with its larger distribution of dye orientations and smaller correlation with twist, the effect is apparently washed out altogether.

We cannot completely rule out that Rop changes the bend angle of the kissing complex. The lack of correlation between $\langle E \rangle$ and bend means that we are likely insensitive to bend. However, a change in bend angle should be correlated with a change in R, and the absence of a change in $\langle E \rangle$ for R1inv-R2inv-G would seem to obviate that possibility. It is not impossible, but very unlikely, that the change in R and change in twist conspire in such a way as to give no change in FRET for the R1inv-R2inv complex.

PART 2: DIMERIZATION INITIATION SITE (DIS) OF HIV-1 GENOME

In part II of my dissertation I include the preliminary work on another kissing complex. First, I give a background about the DIS kissing complex and the ultimate goals we are trying achieve in this project. Next, I will proceed with the initial work I did to prepare the experiments for the next student to continue the project.

CHAPTER 5

BACKGROUND: DIMERIZATION INITIATION SITE (DIS)

HIV-1 (Human Immunodeficiency virus type 1) is a retrovirus known as the cause of the Acquired Immunodeficiency Syndrome (AIDS). Similar to other retrovirus, HIV-1 has two identical RNA genomes that are linked near their 5′ ends within the Dimer Linkage Structure (DLS) [63, 57]. A schematic of HIV-1 genome RNA is shown in Fig.5.1(a).

Dimerization of genomic RNA is known to be important in modulating different steps in the retroviral life cycle such as, encapsidation, translation of the gag gene into viral proteins, reverse transcription. Therefore dimerization of genomic RNA is a target in designing antiviral drugs for HIV-1 and other retroviruses. During the last two decades there has been a lot of effort to understand the mechanism of retroviral genome dimerization. Contrary to previous studies proposing an RNA region downstream of the splice donor site (SD) as the dimerization site [62, 26], Skripkin et al. [90] showed that dimerization of HIV-1 genome initiates from an RNA sequence upstream of SD. This region, located between the primer binding site (PBS) and SD [63], is called the Dimerization Initiation Site (DIS) (Fig. 5.1(a)). Mutations in this region of the HIV-1 genome destroys the dimerization ability [90]. The observation that synthetic RNAs corresponding to the 5′ region of HIV-1 genome dimerize [26], has facilitated the in vitro studies on the HIV-1 system. The 35-nt DIS sequence, shown in Fig. 5.1(b), forms a stem-loop. In the loop region, DIS consists of a highly conserved self-complementary sequence with 6-nt which is flanked by three purines, one on 3′ side (A280) and two on 5′ side (A272, A/G273). These purines

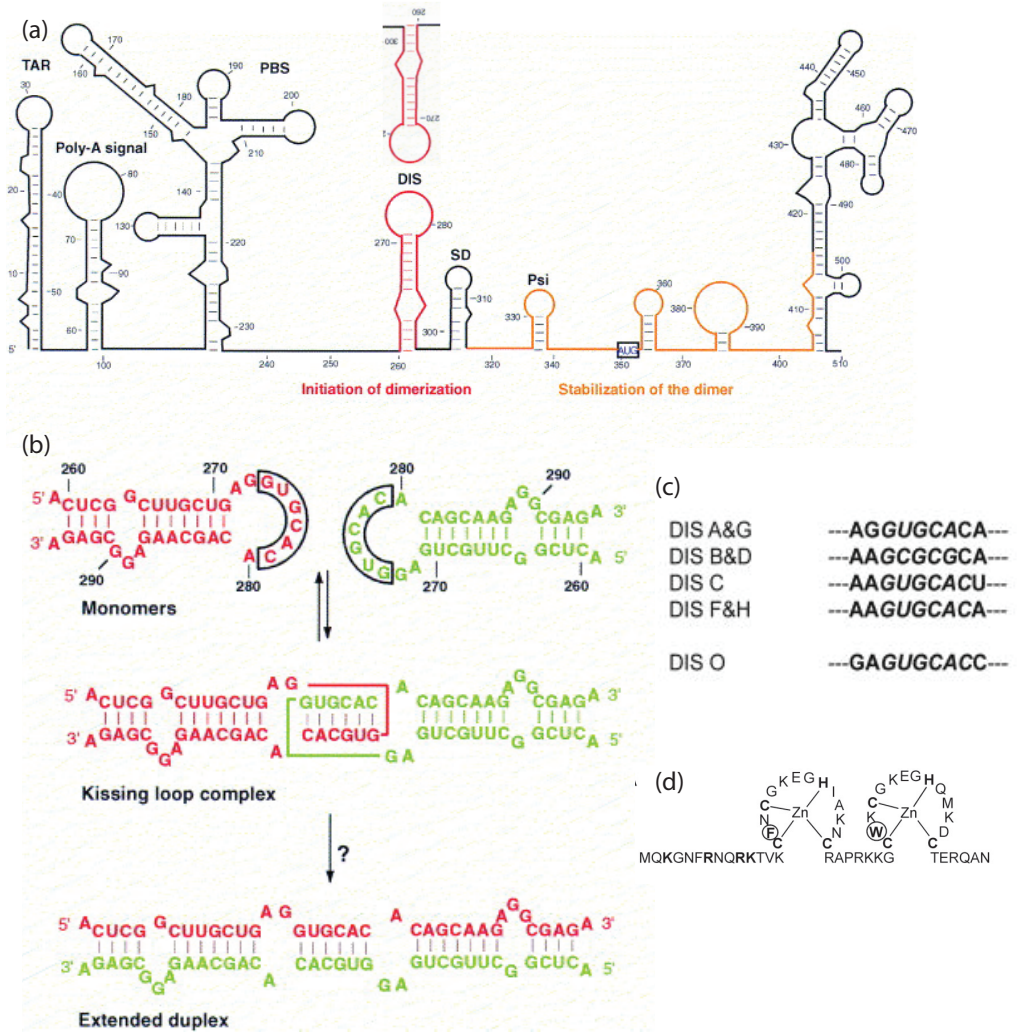

Figure 5.1. (a) Secondary structure of the 5′ UTR region of HIV-1 genomic RNA. Dimerization Initiation site and its complementary stem-loop from the other genome are shown in red [17]. (b) Dimerization mechanism for HIV-1 genomic RNA starts with a kissing interaction at the DIS and proceeds in to a mature duplex [17]. (c) DIS loop sequence for different HIV-1 subtypes [38]. (d) NCp7 structure, Zinc coordinating residues and the basic residues in the N-terminus are shown in bold [1].

are critical for stability of DIS kissing complex [78, 22]. HIV-1 has several subtypes which are shown in Fig. 5.1(c). In HIV-1 subtype A (Mal) and all the other subtypes, except HIV-1 subtype B (Lai) and subtype D, the self-complementary sequence is GUGCAC; in HIV-1 subtype B (Lai) this sequence is GCGCGC.

According to the kissing-loop model proposed for dimerization of HIV-1 genome, the core of dimerization is the 6 nucleotide auto-complementary sequence in the loop. At certain ionic condition these palindromes form Watson-Crick base pairs between loops, known as a kissing interaction. This kissing complex can also form an extended duplex [56, 77] (Fig.5.1(b)). In vitro experiments have shown formation of a stable duplex dimer from the kissing complex happens either by incubation at 55° [56, 69] or by incubation in presence of the viral protein nucleocapsid protein (NCp7) [70].

NCp7 is a 55 amino acid protein (Fig. 5.1(d)). It contains two zinc fingers that are linked by a basic seven amino acid sequence. In one side it has a highly basic N-terminus and on the other end a short six amino acid C-terminus [11, 27]. NCp7 coats nucleic acids by either specific or non-specific binding. NCp7 is known for its chaperone activity [24] which means it binds to nucleic acids and changes the conformation of nucleic acid to its final structure. Experiments using NCp7 mutants show zinc fingers and positive charge of the N-terminus in NCp7 are critical in DIS mature dimer formation [1].

Takahashi *et al.* [93] studied the minimal RNA sequence containing DIS which shows both a kissing complex and a DIS duplex. Takahashi *et al.* deduced the minimal RNA sequence for DIS to mimic this two step conversation is a sequence with optimal stability in stem. Low stability makes kissing step undetectable, and high stability makes duplex formation difficult.

The sturcture of the DIS kissing complex and duplex have been studied using NMR [67, 41, 5] and X-ray [35, 36]. Most of these studies are performed on a truncated

DIS stem-loop with 23 base pairs. The main difference between the crystal and NMR solution structures are different conformations for A272 and R273.

Crystal structure of DIS kissing complex for Mal and Lai subtypes shows complete coaxial alignment and stacking of the two purines A272 and R273 in a bulged out conformation (Fig. 5.2(a)) [35]. Here A280 is unpaired and always stacked inside the helix. DIS (Lai) kissing complex structure obtained by NMR [67] is different from the crystal structure. The loop helix for this structure deviates from an A-form helix (Fig. 5.2(c)). The observed bend in this structure indicates possibility of a hing-like flexibility. The NMR structure determined by Baba *et al.* [5] for DIS subtype F (similar to Mal) shows A272 and A273 are stacked inside the helix. In compare with the structure resolved by Mujeeb *et al.* they observe a different conformation for R273. Therefore the global structure reported by Baba *et al.* does not show a bend (Fig. 5.2(d)).

Crystal structure of DIS duplex [36] shows a complete coaxial alignment similar to kissing DIS. In Mal subtype, A272 is bulged out and duplex shows two G273-A280 Watson-Crick like mismatches in vicinity of A272 (Fig. 5.2(b)). In subtype Lai two unpaired A272, A273 are bulged out and stacked, and A280 is unpaired and stacked inside. The overall NMR structure of DIS extended duplex measured by Baba *et al.* [41, 5] is similar to the crystal structure, but for both subtypes unpaired adenines are stacked inside the helix (Fig. 5.2(e)). Baba *et al.* used the complete DIS stem-loop with 39 nucleotides for the NMR solution measurements.

In the kissing complex model which is the proposed model for DIS hairpins, the first step is base pairing of the two hairpins from complementary loops: then the structure rearranges to reach coaxial alignment. Salim *et al.* [85] studied kinetics and thermodynamics of RNA hairpins; they used HP1and HP2 hairpins, which are derivatives of the *E. coli* DsrA-rpoS bulge-loop, as their model system. Using ITC (isothermal titration calorimetry), UV melting, smFRET and SPR (surface plasmon

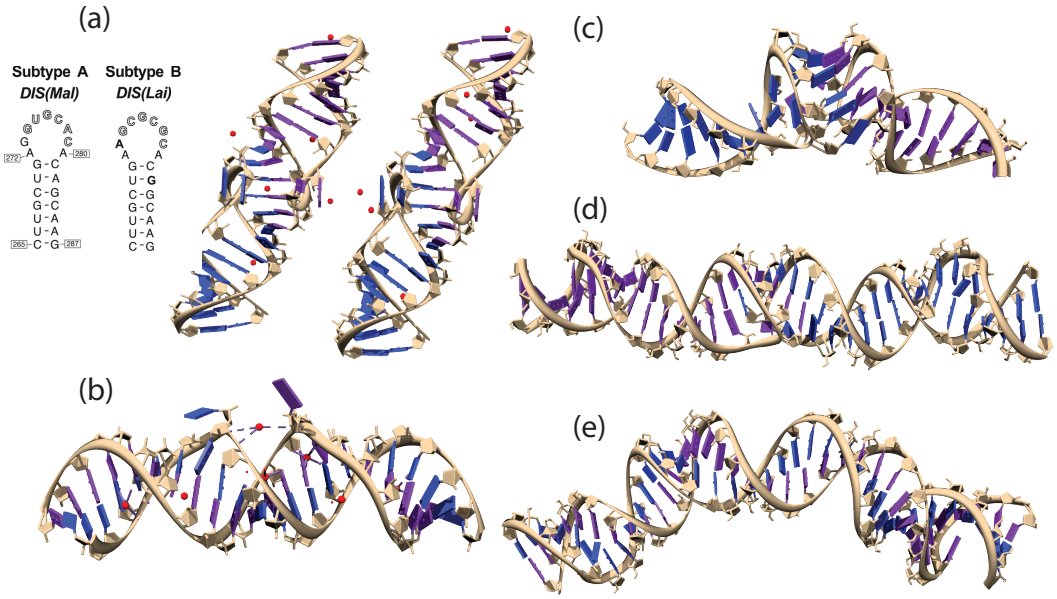

Figure 5.2. (a) Secondary structure for DIS(Mal) and DIS(Lai) with 23 nucleotides, the x-ray and NMR structures shown in part (a-c) have the same sequence. From left to right x-ray tertiary structures for DIS(Mal) and DIS(Lai) kissing complex. In both types, purines A272 and R273 from each stem-loop are bulged out and stacked. The red circles represent Mg^{+2} ions (PDB2b8s and PDB2b8r) [35]. (b) X-ray tertiary structure for DIS(Mal) extended duplex(PDB1y99) [36]. (c) NMR solution structure for DIS(Lai) kissing complex (PDB1bau) [67]. (d) NMR solution structure for DIS(Mal) kissing complex with 39 nucleotides (PDB2d1b) [5]. (e) NMR solution structure for DIS(Mal) extended duplex with 39 nucleotides (PDB2d1a) [5].

resonance) data, they proposed an energy landscape for kissing complex formation and its conversion to extended duplex (Fig. 5.3). Their data indicates kissing complex to duplex transition requires overcoming to a large energy barrier, and proteins like NCp7 can facilitate this transition by decreasing the energy barrier. The hairpin to duplex ratio is found to be highly dependent on concentration of hairpins [12, 93] and self-complementarity of loops [12, 53].

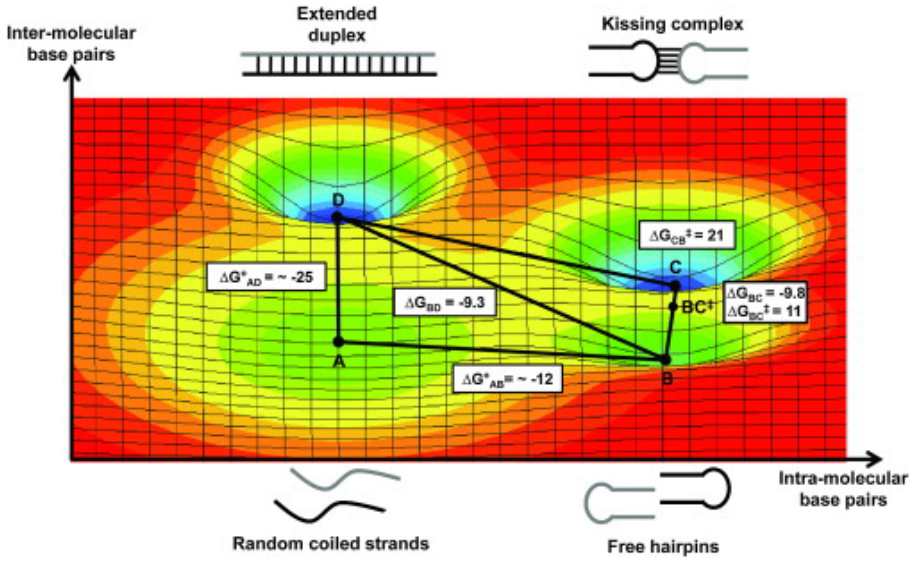

Figure 5.3. From Ref. [85]: Putative potential energy surface for KC and ED formation. Thermodynamic (ΔG_{ij}) and activation energies (ΔG^*_{ij}) for pathways associated with KC formation and their conversion to EDs. Thermodynamic data were obtained using ITC, UV melting, and smFRET, and activation parameters were derived from kinetic data obtained by SPR and smFRET. Reaction coordinates are defined by the number of intramolecular (X) and intermolecular (Y) basepairs present in the molecular ensemble of a particular state. Stabilization energies are plotted along the z axis. Four different states are shown: unfolded strands (A), free hair- pins (B), the KC (C), and the ED (D). The energy of unfolded strands (A) was used as the reference state (ΔG_A).

Rist and Marino [82] used 2-AP (an adenosine base analogue) labeled stem-loops to report on kinetics of DIS kissing complex and its conversion to extended duplex. 2-AP is bright in its unstacked state and its fluorescence decreases once it stacks by

base pairing. By substituting 2-AP with an adenosine in the loop and monitoring the change in fluorescence in time, they found an equilibrium binding constant of $K_D = 3 \pm 1$ nM for DIS kissing complex. In a similar measurement, by substituting 2-AP with an adenosine in the stem and in presence of enough concentration of NCp7 they found a kissing to dimer conversion rate of $K_{conv} = 0.46 \pm 0.024$ min^{-1} for 100 nM kissing complex and 250 nM of NCp7. An equilibrium dissociation constant of $K_D = 61 \pm 12$ nM was found for binding of NCp7 to DIS kissing complex. Divalent ions such as Mg^{+2} stabilize DIS in its kissing form and transition to mature duplex is only possible in presence of enough NCp7. This protein accelerates rate of conversion from kissing DIS to extended duplex; the maximum DIS conversion rate is obtained for a 2:1 stochiometry for NCp7:DIS. Since previous studies indicate necessity of one NCp7 per seven nucleotides RNA for NCp7 to have its chaperone function, it is suggested that DIS stem-loop needs to be saturated with NCp7 to have its complete catalytic effect [82]. Rist *et al.* propose a secondary structure rearrangement model for kissing complex to duplex conversion. According to this model, kissing complex has structural dynamics and at an intermediate transient state NCp7 binding and stem exchange might be favored. A bend structure, similar to the NMR solution structure of R1inv-R2inv kissing complex, might be a possible conformation; such a conformation can bring the two stems closer and facilitate stem exchange. Our initial goal was to resolve this intermediate bent structure using single molecule FRET.

Mihailescu *et al.* [65] used NMR spectroscopy and reported on localized conformational dynamics for DIS kissing complex with time scale of micro- to milli- seconds. They attribute the observed dynamics to protonation of the N1 nitrogen of A272 in the loop near pH 6.5. They measured C2 and C8 chemical shifts at different pHs from 5.5 to 8.2 for all the adenines in the stem-loop and found a pK_a of 6 ± 1 for A272 and pK_a of 4.5 for all the other adenines. This explains the local dynamics observed at near physiological pH. The rate of conversion to extended duplex was measured at

pH 6 and 7.2; and found to be five times faster at pH 6. For this measurement 2-AP was substituted with an adenine in the loop, as discussed earlier, and the change in fluorescent was monitored in time. At pH 6 and pH 7.2, 72% and 20% of A272 is protonated, respectively. The acceleration in catalyzing effect of NCp7 is attributed to A272 protonation [65].

Ennifar *et al.* [37] showed the crystal structure of HIV-1 DIS kissing complex is very similar to the bacterial 16S ribosomal aminoacyl-tRNA site (A-site). Similarities between ribosomal A-site and DIS kissing complex is shown in Fig. 5.4(a). Since ribosomal A-site is a target for amino glycoside antibiotics, it is expected that DIS kissing complex also be a target. Current antiviral drugs, target viral enzymes such as reverse transcriptase and protease. Due to observed resistance to some of the drugs and their side effects, targeting other viral sites such as locations within the HIV-1 RNA genome might provide an alternative solution.

Binding of a variety of aminoglycoside antibiotics to DIS kissing complex was studied using gel shift, lead-induced cleavage and footpring experiments. Among different antibiotics (such as amikacin, kanamycin, gentamicin, geneticine, neomycin, ribotamycin, paromomycin, spectinomycin and tobramycin) only a few (such as neomycin and paromomycine) bind to DIS kissing complex with high affinity[39]. The footprint of neomycin on DIS kissing complex and ribosomal A-site is shown in Fig. 5.4(b). ITC (isothermal titration calorimetry) microcalorimetry measures a high affinity of $\approx$ 30nM for DIS kissing complex and neomycin or lividomycin, and lower affinity of $\approx \mu$M for paromomycin and apramycin [13]. In general, 4,5-disubstituted 2-desoxystreptamine (2-DOS) amino glycoside antibiotics (with 5 rings), such as neomycin, paromomycin and lividomycin have high affinity for DIS kissing complex; while this is not true for 4,6-disubstituted 2-DOS antibiotics (with 3 rings), such as tobramycin and kanamycin. Chemical structure for aminoglycoside antibiotics is shown in Fig. 5.4(c). Neomycin and promomycin binding to DIS kissing complex increases

stability of the complex. Stability was studied using UV-melting; at 100 mM NaCl, melting temperature of DIS kissing complex (65.6 °C) increases by 6.4 °C in presence of neomycin and 1.7 °C in presence of paromomycin [39]. Increase in stability of DIS kissing prevents it from converting to an extended duplex [13].

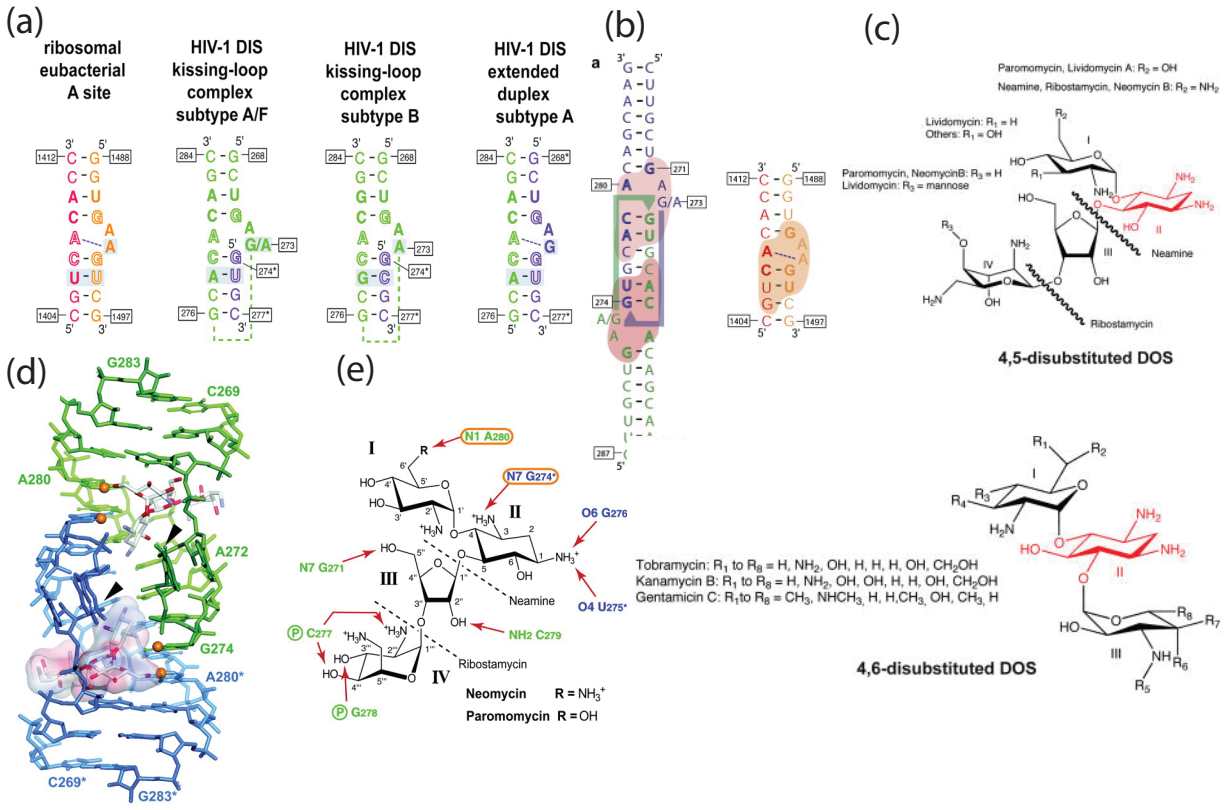

Figure 5.4. (a) Sequence similarities between HIV-1 DIS (subtype A and B) and ribosomal A-site [39]. Open symbols represent the conserved residues involved in antibiotic binding and boldface symbols represent the A-site motif residues. The difference between sequences is highlighted with a grey box. (b) Neomycin footprint on 23-mer DIS kissing complex and ribosomal A-site. Essential bases for antibiotic binding are in bold [37]. (c) Chemical structure of 4,5-disubstituted 2-desoxystreptamine (top) and 4,6-disubstituted 2-desoxystreptamine (bottom) aminoglycoside antibiotics [38]. (d) Molecular model for binding of two antibiotic molecules to DIS (subtype A) kissing complex. Orange circles represent positions on RNA that are protected against chemical modification upon binding of antibiotic [39]. (e) Observed contacts between DIS kissing complex and neomycin and paromomycin [39].

Mundigala *et al.* [68] used single molecule FRET and reported on kinetics of KC formation and its conversion to duplex. For KC formation they measure $k_{on} = 10^5\ M^{-1}s^{-1}$ and a short lived KC with $k^1_{off} = 0.9\ min^{-1}$ and a long lived KC with $k^2_{off} = 0.15\ min^{-1}$. These measurements are made at 20 mM Tris (pH 7.4), 5 mM Mg^{2+} and 150 mM KCl. They also observed a bent intermediate required for KC to duplex conversion; this intermediate highly relies on Mg^{2+} ions. Figure. 5.5 describes the proposed kinetics model for DIS kissing complex to duplex transition [68]. In absence of NCp7 only 13% of the kissing complexes reach the duplex state. They also show by mutating A272, the long lived KC population disappears; similar behavior happens to DIS KC in absence of Mg^{2+}. Therefore binding of Mg^{2+} most probably happens near A272.

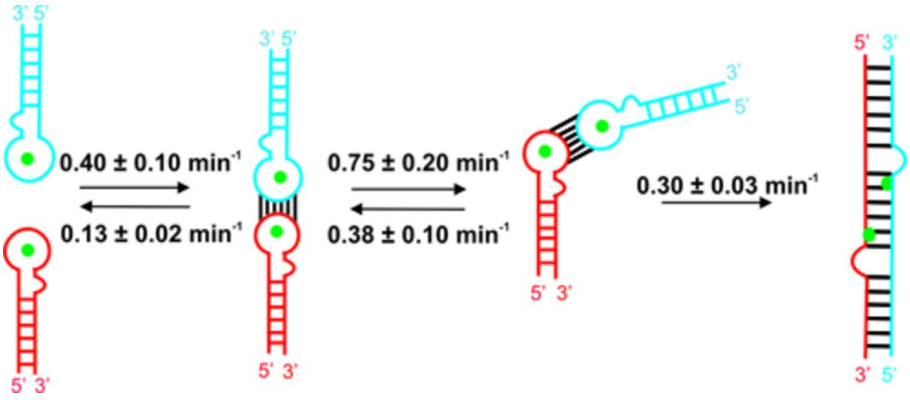

Figure 5.5. From Ref. [68]: Minimal kinetic model for HIV-1 RNA dimerization.

Our goal for DIS dynamics project is to observe the intermediate bent structure, predicted by Rist and Marino [82] and reported by [68], and study the effect of NCp7 and antibiotics on the dynamics of DIS KC to duplex conversion and formation of the bent intermediate structure. NCp7 facilitates stem exchange and extended duplex formation and antibiotics like Neomycin prevent duplex formation by stabilizing the KC state, in both cases we would expect a change in conformation of the intermediate state.

Another aim is to study the effect of Rop protein on the dynamics and kinetics of DIS KC to duplex conversion. Rop protein is known to bind to RNAI-RNAII KC by recognizing its bent structure and stabilizing the KC. We have evidence that Rop protein binds to DIS KC. We ran a gel shift assay for DIS kissing complex in presence of different concentrations of Rop protein. The gel was prepared in the same condition as for R1inv-R2inv/Rop complex. Interestingly the gel result shown in Fig. 5.6 indicates binding of Rop to DIS kissing complex. Therefore it is possible that Rop have the same stabilizing effect as it has for R1inv-R2inv KC. Also it probably affects the conformation of the intermediate state. Rop protein can be introduced to the system at the same time as NCp7, if Rop protein binds to the KC competitively it can either abolish the role of NCp7 or enhance its function. If Rop protein can stop dimerization to happen, this will introduce a new insight in designing anti HIV drugs.

Better understanding of conformational dynamics of DIS kissing complex can give us insight into the mechanism of kissing complex to duplex conversion, and as a result a way to control dimerization as an antiviral drug. It can also provide a model for understanding other short RNA dynamics.

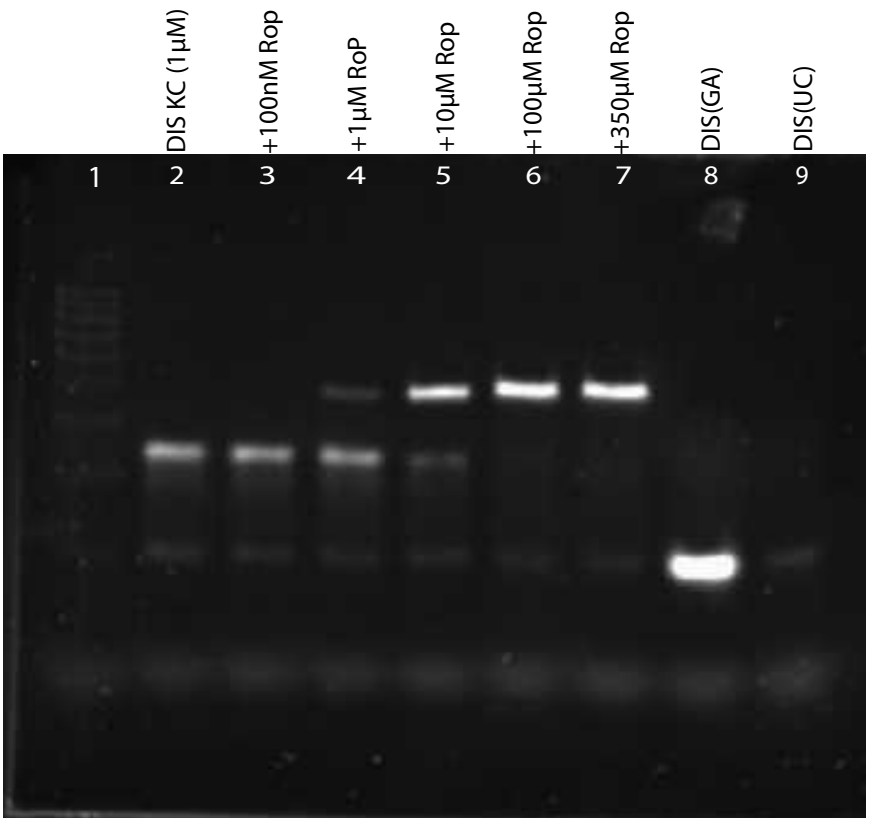

Figure 5.6. Electrophoresis gel demonstrating the binding of Rop to DIS kissing complex. First lane is a DNA ladder. DIS(GA) and DIS(UC), both at concentration of 1.5 μM, are labeled with Cy3 and Cy5 respectively, and the gel is stained with SYBR green I dye (invitrogen) which is a nucleic acid gel stain.

CHAPTER 6

PRELIMINARY WORK: FRET-TIRF MEASUREMENTS ON DIS

My intent was to use Total Internal Reflection Microscopy (TIRF) to study conformational changes of DIS kissing complex and its conversion to dimer duplex. The millisecond resolution of TIRF microscopy makes observation of intermediate states, if any, possible.

TIRF microscopy uses the phenomenon of total internal reflection. Even at total reflection from surface an evanescent field exists in the low refractive index medium (water) to excite the fluorescent molecules in the vicinity of the coverslip [4]. The evanescent field decays exponentially with increasing distance normal to the surface. The small penetration depth (in the order of wavelength of incident light) of evanescent waves suppresses the background fluorescence from other parts of the sample. Also this technique has the advantage of observing hundreds or thousands of molecules simultaneously.

We used an objective-type TIRF microscope, shown in Fig. 6.1(a). The 514 nm Ar laser light is sent to fluorescent molecules immobilized on the coverslip surface. The emitted fluorescent signal from fluorophores (Cy3B and Cy5) are collected with a high numerical aperture objective (Olympus 60x NA 1.45).

To measure FRET, the donor and acceptor emitted light should be separated and imaged side by side on a CCD camera (iXon 879 DU, Andor), for that I added a dual-view to the TIRF microscope. The design for dual view is shown in Fig. 6.1(b). An adjustable slit is placed in the image plane of the side port of the micrsocope

to restrict the imaging area to half the size of the CCD chip. Donor and acceptor emission is split using a dichroic mirror and imaged on the CCD.

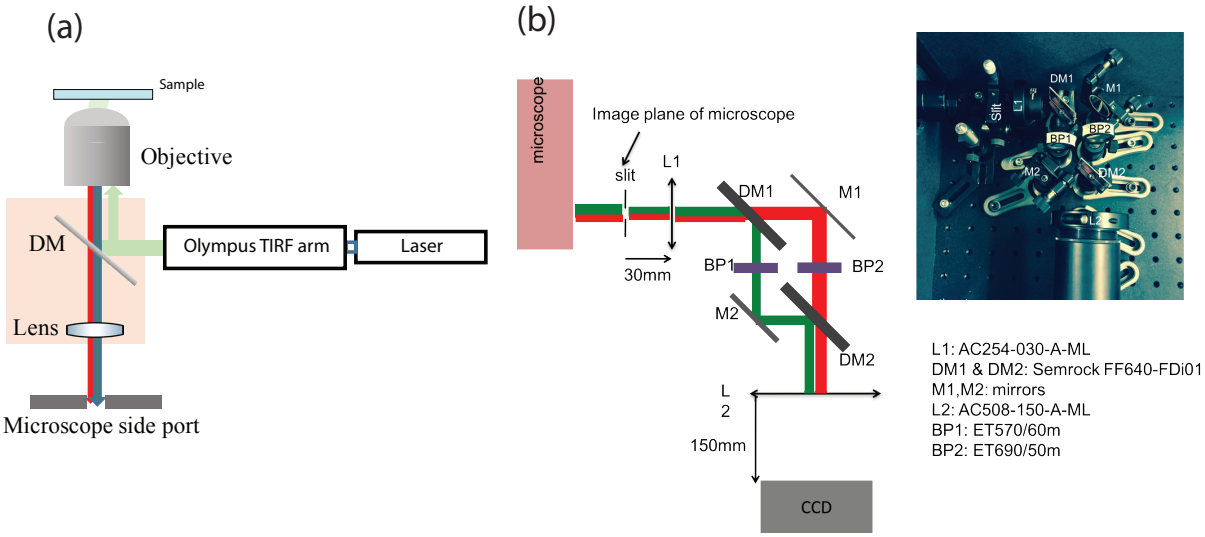

Figure 6.1. (a) Schematic for an objective type TIRF microscope. Single molecules tethered to surface are excited with laser light. Collected fluorescent light from donor and acceptor molecules are separated and imaged using a dual view. (b) Design for the home-built dual view, an adjustable slit is positioned at the image plane of the microscope. The first dichoric mirror (DM) separates the donor and acceptor emission and the second DM sends them to the CCD camera.

Dynamics of DIS KC conversion to duplex happens at timescales longer than a few milliseconds, therefore solution FRET measurements using a confocal microscope is not capable of identifying the intermediate states in KC to duplex conversion. By immobilizing molecules on the surface, it would be possible to observe them over longer periods of time.

6.1 Surface passivation and attachement

Two different strategies can be used for surface immobilization (Fig. 6.2). In one method we can coat a glass slide with biotinylated BSA and Neutravidin (or Streptavidine). The biotinylated RNA molecules can bind to BSA through Neutravidin

(or Streptavidine) [103]. For measurements including a protein, it is recommended to passivate the surface with PEG (Polyethylene Glycol) to suppress nonspecific binding to surface (BSA coated surface is too adhesive for protein studies) [44]. For passivating the surface with PEG, slides and coverslips are incubated with a solution of NHS esters of PEG and biotin PEG (Fig. 6.2). I used the PEGylation method for surface preparation; the detailed protocol for surface immobilization procedure and required materials can be found in Ref. [20]. In Fig. 6.3 I summarized different steps for surface passivation.

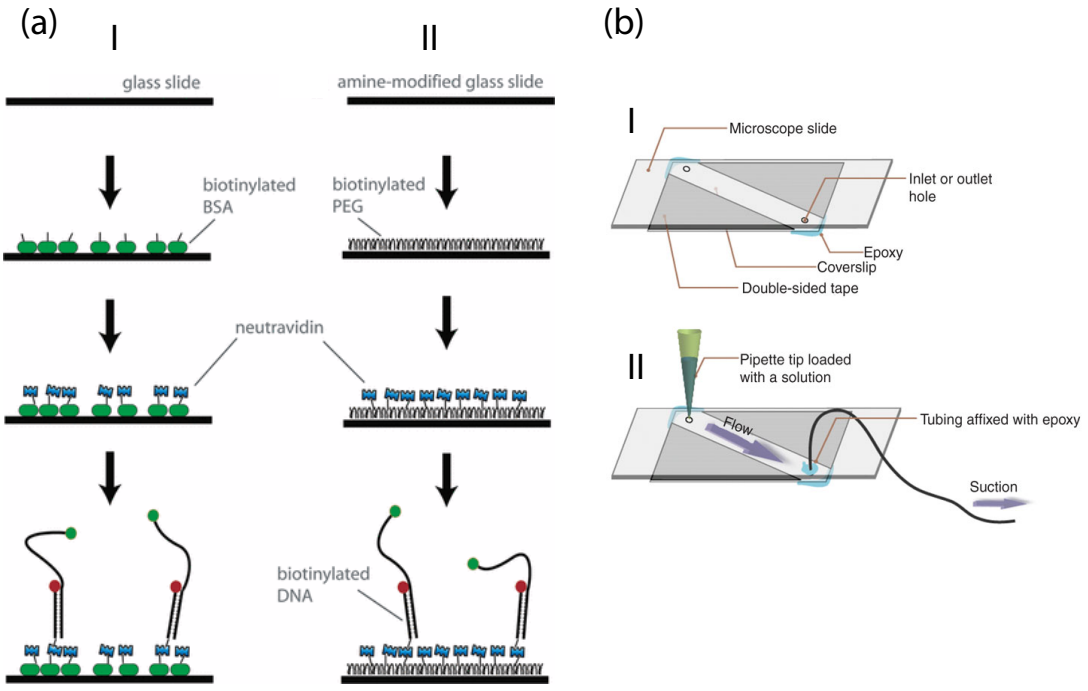

Figure 6.2. (a) immobilization strategies: (I) Surface is passivated with biotinylated BSA and biotinylated RNA molecules are tethered to surface through Neutravidin, (II) Passivating the surface with NHS ester PEG and biotin PEG. Neutravidin binds to biotin PEG species, and biotinylated RNA molecules are tethered through Neuravidin [45]. (b) Sample chamber: (I) double sided tape sandwiched between a glass slide and coverslip. two holes are drilled in the glass slide to allow solution exchange, (II) a pipette tip is plugged into the inlet hole, and a string containing the solution is connected to the pipette [45, 84].

Surface passivation for single molecule experiments

I) Cleaning glass slide and coverslip

1) water (sonication in MilliQ water several times)

2) Aceton (sonication in Acetone for 20min, rinsed with water 3 times)

3) KOH 1M (sonication in KOH 1M for 20min, rinse with water 3 times)

4) Piranha etching (keeping in 600ml mixture of H_2SO_4: H_2O_2 (3:1) for 20min, rinse with water)

<u>* Piranha etching step makes the glass hydrophilic with OH groups</u>

II) Amino-Silanization of surface

1) While preparing the amino-silanization solution keeping slides in Methanol.

2) incubation in amino-silanization solution for 20-30min

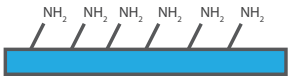

amino-silanization solution:

100ml Methanol + 5ml Acetic acid + 3ml APTES

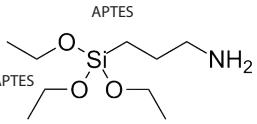

3) Rinse with Methanol and keep in Methanol.

III) Surface passivation using NHS-ester PEG (First round)

1) Dry with N_2 gas and place them in pipette boxes

2) Drop 70µl of PEGylation mixure on the slide, and place a dried coverslip over it.

PEGylation mixture:
mixing 0.2 mg <u>biotinylated NHS-ester PEG (5kDa)</u> + 8 mg <u>NHS-ester mPEG (5kDa)</u> in 1.5 ml tube + 64ul sodium bicarbonate buffer

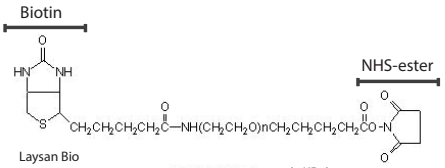

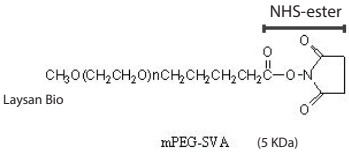

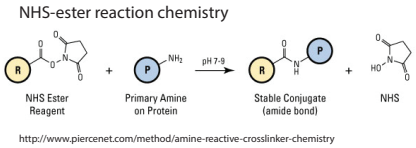

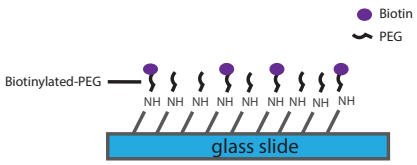

Then put a clean coverslip on it.

3) Incubate overnight or at least for 2 hours.

4) Dissamble slide and coverslip, and dry them. For imediate use go to next step which is second round of PEGylation. For storing put them in a tube and vuccume the tube and fill it with N_2, and store it in freezer.

IV) Assembling a Microfluidic Chamber:

place a PEGylated coverslip on the PEGylated side of the glass slide. double sided tap will be sandwitched between the two glasses making a small channel. The edges can be sealed by epoxy.

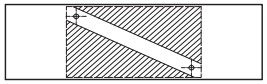

The solid lines show the glass slide, dotted lines shows the coverslip and hashed lines show double sided tape.

adding 50 µl of 0.1 mg/ml of Neutravidin solution in the buffer of 10 mM Tris-HCl [pH 8] with 50mM NaCl. After 1min incubation, flush with 100µl of buffer.

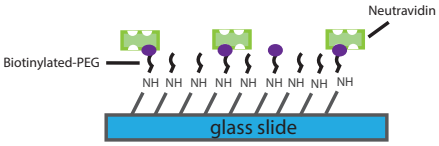

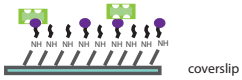

Finally, adding the biotinylated biological molecules.

Density of RNA molecules on surface shouldn't be too high or too low; for a 25 μM$\times$50 μM field of view, having $\approx$200 molecules is reasonable [45]. We used a 30 pM concentration of biotinylated DIS-Cy3 molecules.

6.2 Design of DIS kissing complex constructs

We are studying a short derivative of dimerization Initiation Site (DIS). Each stem-loop has 21 nucleotides, and with respect to the wild-type they are mutated in the loop (Fig. 6.4(b)). One base pair in the loop is flipped to prevent formation of homodimer complexes with two similar color dyes on them. Also the G-C base pair at the end of stem gives the stem-loops the proper stability to reproduce the two step kissing complex to duplex conversion. These RNA constructs are similar to the DIS sequence used in the study by Mundigala *et al.* [68]. DIS1 is labeled on the 5′ guanine terminus with Cy3B, the 3′ terminus has a short UAU extention to minimize RNA interaction with surface. The 3′ end is biotinylated, and DIS1 hairpin will be tethered to surface from this end. The other construct DIS(m) (Fig. 6.4(c)) is mutated in the stem to prevent it from duplex formation; this construct will be used in control experiments were we don't want extended duplex to form. A schematic for DIS kissing complex tethered to surface is shown in Fig. 6.4(e). In the KC state, Cy3B and Cy5 will be in distance and we would expect to measure low FRET. While in the extended duplex form, dyes are in close proximity and we would expect to measure high FRET.

6.2.1 Fluorescence dyes

Some characteristics that make fluorescent dyes suitable for single molecule fluorescence experiments are as follow: 1) high brightness, 2) high quantum yield, 3) photostability and 4) being small and water soluble. These fluorophores make a good

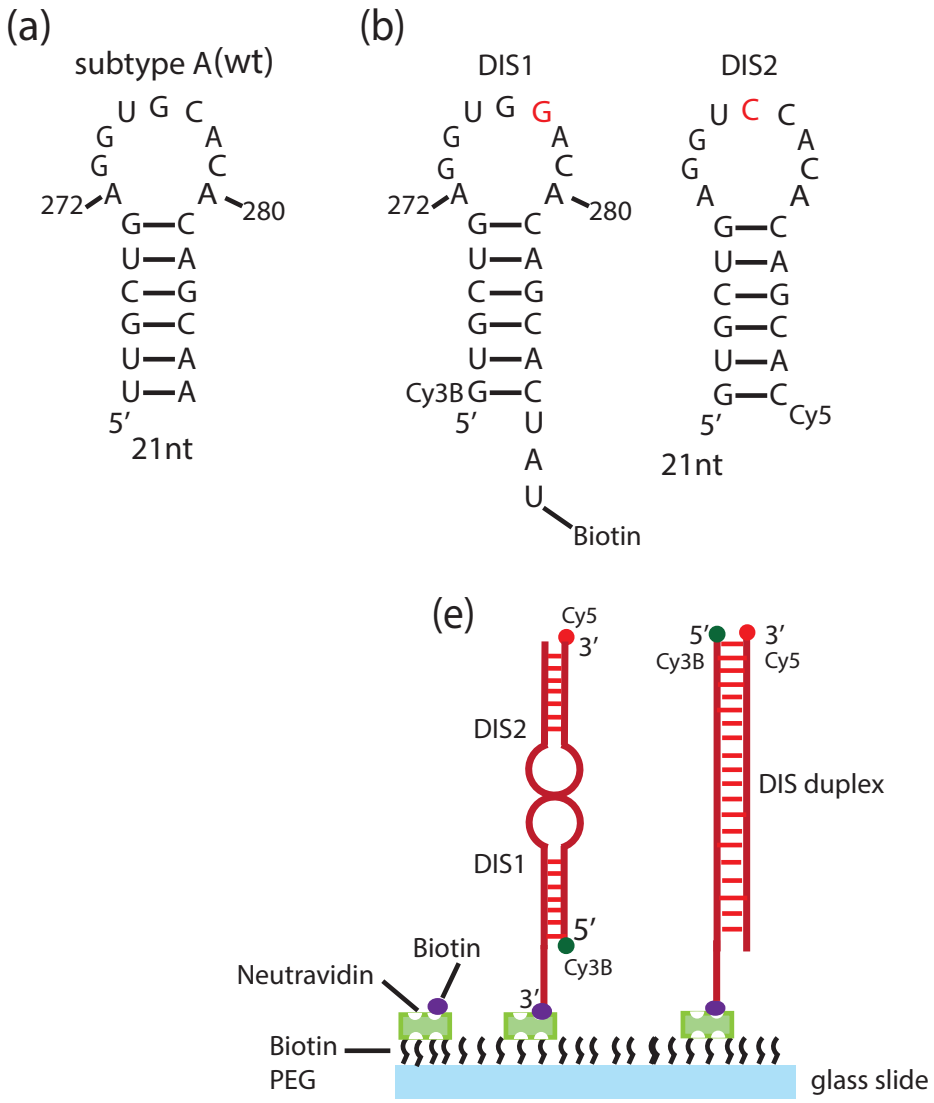

Figure 6.4. (a) A 21bp derivative of wild type DIS A-type. (b) DIS1 sequence with 21 nucleotides and its complementary sequence DIS2; both with one base pair flipped in the loop to prevent homodimer formation. Mutations are shown in red. (c) DIS(m) has mutations in the stem, shown with the box, to avoid duplex formation. (d) On left side of glass slide DIS kissing complex is shown immobilized on surface through a UAU short strand. In this conformation Cy3B and Cy5 fluorophores are distant. On right side of the glass slide, DIS is shown after conversion to extended duplex; in this state dyes are in close proximity.

Table 6.1. Some characteristics of common fluorescent dyes in FRET measurements (this data are from atdbio and GE life technologies websites).

Dye	λ_{max}(excitation)	λ_{max}(emission)	$\epsilon(\mathrm{M^{-1}cm^{-1}})$	quantum yield	τ(ns)
Cy3	550	570	136000	0.15	0.3
Cy5	649	670	250000	0.3	1
Cy3B	558	572	130000	0.67	2.8
Atto647N	644	669	150000	0.65	3.5

FRET pair if the spectral separation between donor and acceptor emission is large and their quantum yields and detection efficiencies are similar [84].

Common FRET pairs are Cy3-Cy5 and Cy3B-Atto647N. In Table. 6.1 some characteristics of these dyes are summarized. Cy3 can undergo cis-trans isomerization because of its conjugated chain. While Cy3B has a rigid aromatic chain which prevents isomerization. This makes Cy3B brighter and more photostable in comparison with Cy3, we used it as the donor dye and kept Cy5 as the acceptor. As it will be shown in the next section, it seems Cy3B-Cy5 do not make a good FRET pair and this is most probably because of the large difference in their quantum yields. Therefore we decided to use Cy3B-Atto647N for the experiments. Figure. 6.5 shows the chemical structure for Cy3, Cy5, Cy3B and Atto647N[86].

6.2.2 Sample Preparation

RNA, dye-labeled RNA molecules (biotinylated on its $3'$ terminus and labeled with Cy3B on the $5'$ terminus) are purchased from Integrated DNA Technologies (IDT). NCp7 was provided by Michael Miller in Daniele Fabris Lab at University at Albany. DIS hairpins can be formed with the same method used for R1inv-R2inv complex: heating RNA strands for 3 minutes at 93 °C, then snap cooling on dry ice for 3 minutes. First DIS1-Cy3B stem-loop was added to the chamber and imaged and then the complementary DIS2 strand was added to form the KC. To improve

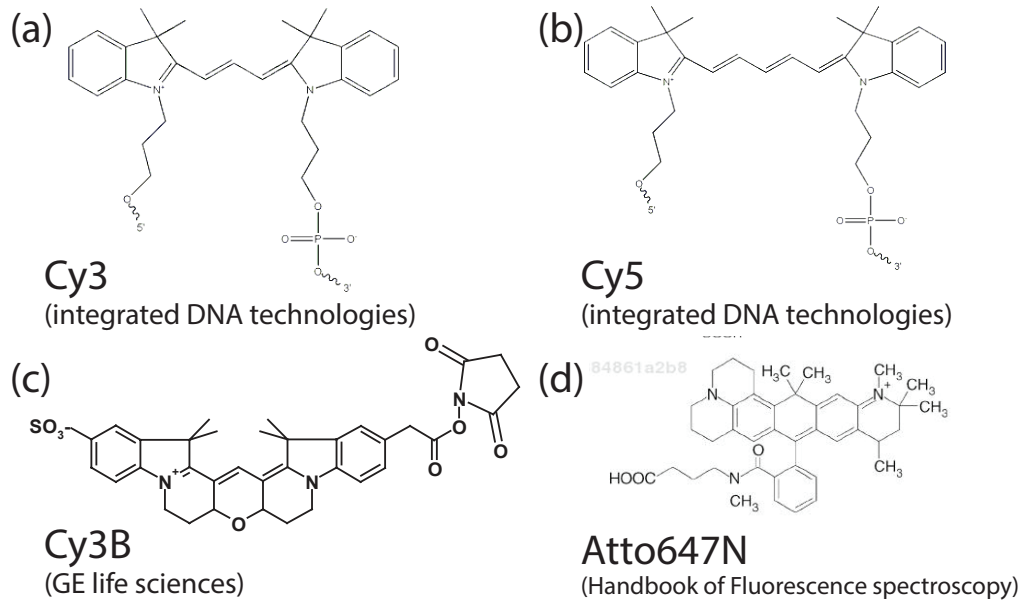

Figure 6.5. Chemical structure for: (a) Cy3 phosphoramidite (IDT website), (b) Cy5 phosphoramidite (IDT website) (c) Cy3B (GE lifesciences websit) (d) Atto647N NHS ester[86].

photophysics of the fluorophores and minimize photobleaching and blinking of them, protocatechuate3,4-dioxygenase (PCD) and protocatechuic acid (PCA) was added to the RNA mixture as an enzymatic oxygen scavenger system [2] and methylviologen (MV) was added as part of the reducing and oxidizing system (ROXS) [95].

Sample chamber was prepared by sandwiching double sided tape between a pre-cleaned slide and coverslip, and sealing it with grease. Since we want to exchange buffer solution and inject protein during the measurement, we drilled two holes in the glass slide; this allows pipetting or pumping and therefore exchange of solution (Fig. 6.2(b)). For exchanging solution through the holes we used Cole Parmer 30 gauge tubings, and used epoxy to seal it.

6.2.3 Preliminary work

First I calibrated the system to find the pixel size. To find the pixel size I imaged a micrometer scale (0.01 mm) centered on a glass slide (Fig. 6.6(a)) and measured

the number of pixels between two grids several times (Using ImagJ) and found and average of 183 pixels between every two grids. Knowing the distance between two grids is 10 μm I found a pixel size of 54 nm.

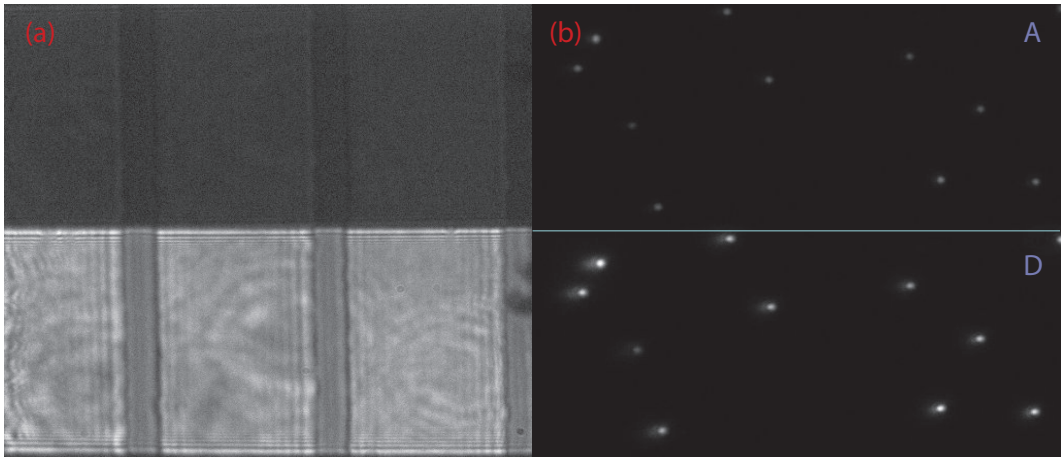

Figure 6.6. (a) Image for 0.01mm micrometer scale, (b) Image for multicolor fluorescent beads excited at 514 nm.

The image in donor and acceptor channels are not completely on top of each other, therefore it is necessary to overlay them by making a transformation map. Before taking movies of the RNA samples, I take an image of multicolor fluorescence beads (Spherotech, 0.14 μm cat# FP0257-2) immobilized on surface (Fig. 6.6(b)). By finding a few beads in the donor channel and the corresponding beads in the acceptor channel it will be possible to generate a linear transformation between the two images.

Next I checked the background by flowing in a solution of buffer containing Tris, NaCl and $MgCl_2$ (Fig. 6.7(a)), background image shows there are not many contaminants in the buffer. Next, I injected the DIS1-Cy3B sample to check for non-specific binding (Fig. 6.7(b)). There are a small number of molecules binding nonspecifically. After injecting a 0.1 mgr/mL solution of Neutravidin in the flow cell and incubating it for 2 minutes, I washed it with buffer two times and injected a solution of

biotinylated DIS1-Cy3B with concentration of 30 pM. Finally, I washed the chamber with buffer to remove DIS molecules that are not tethered successfully and filled the chamber with buffer containing the oxygen scavenger components. In Fig. 6.7(c), one frame of the movie taken on this sample is shown. In the donor channel area, 54 DIS-Cy3B molecules are identified. After adding 50 nM of DIS-Cy5, formation of KC is expected, and we would expect to have fluorescent molecules in the acceptor channel due to FRET. .

For identifying the features I used the Python version of Dr. Maria Kilfoil's particle tracking package. This code is based on an IDL code by John Crocker. It identifies the high intensity regions on the image, and then excludes the false features based on their intensity and shape. Fig. 6.8 shows features found for an image of tethered DIS1 molecules labeled with Cy3B in the donor channel. First the feature finding algorithm finds about thousands of bright spots, since many of these high intensity regions are noise. After false features are removed, 54 features were identified which are shown with red circles. The right panel of Fig. 6.8 shows the intensity profile for one of these features. The number of photons is calculated from pixel intensities using: $\#\ of\ photons = \frac{counts \times sensitivity}{EM \times qe}$, here counts is the intensity of each pixel, sensitivity for our camera is 3.94, EM gain is set to 300 and quantum yield (qe) is 0.95. Average background is about 3 photons per pixel.

In order to form the kissing complex I added a high concentration of DIS2-Cy5 (50 nM). Once the kissing complex forms we would expect to have bright molecules both in donor and acceptor channels. Fig. 6.9(a) and (b) shows an image for donor and acceptor channels respectively. The corresponding intensity profile for one feature of each image is shown on the right. The signal to noise ratio is better in the donor channel this is because molecules are excited directly with 514 nm laser light. The emission from molecules in the acceptor channel is due to FRET and shows a smaller signal to noise. Considering the length of DIS strands a FRET efficiency of 0.4-0.5 is

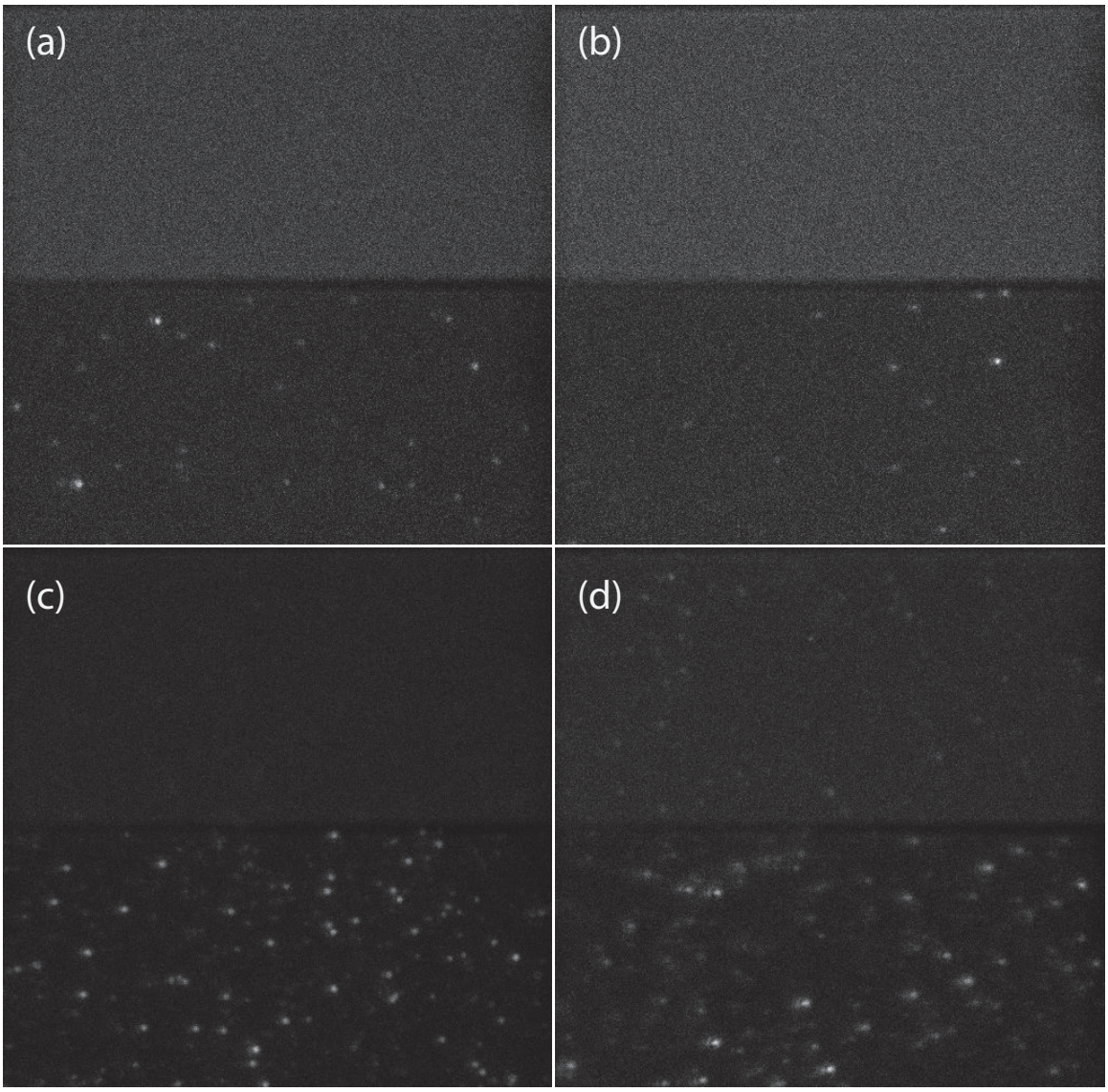

Figure 6.7. In all panels the top of the image is acceptor channel and bottom of image is donor channel, (a) Background image from a buffer only sample, (b) non-specific binding of DIS1-Cy3B to the chamber, (c) Image for DIS1-Cy3B tethered to surface, (d) Image for DIS1Cy3B-DIS2Cy5 kissing complex. For all these images sample is excited with 514 nm laser light at 6 mW and CCD is set to: exposure time of 1 sec, EM gain of 300 and pre-amplifier of 2.5x.

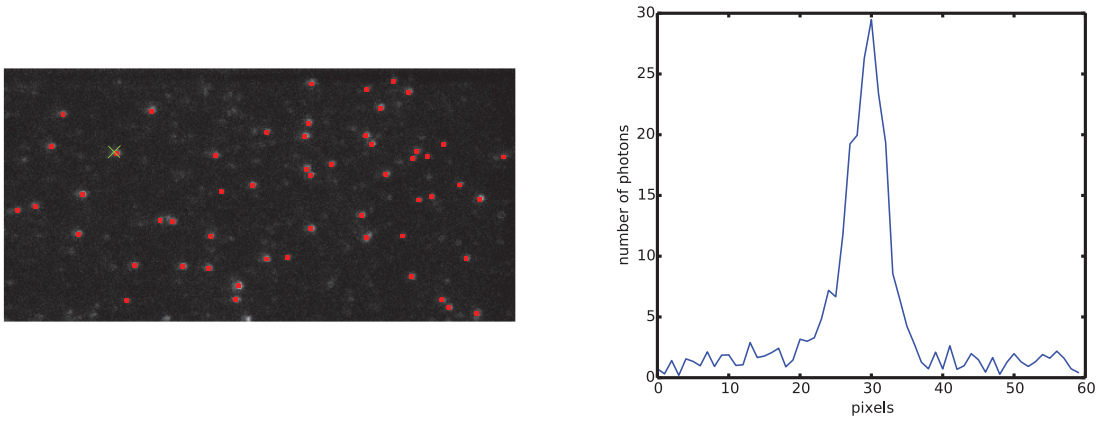

Figure 6.8. (left) Image of 30 pM DIS1-Cy3B molecules tethered to surface; identified features are shown with red dots. (right) intensity profile in terms of number of photons for one the molecules (green cross)

expected, but here there are not much fluorescence in the acceptor channel. In the duplex form the donor and acceptor fluorophores will be in close proximity and we would expect to measure a FRET efficiency of about 1.

Since I wasn't getting a large enough FRET signal for the DIS1Cy3B-DIS2Cy5 KCs, I did a TIRF-FRET measurement for a duplex DNA (OligoAD) with large FRET of about 1. OligoAD [71] shown in Figure. 6.11 is a double stranded DNA with a short single stranded DNA hanging from one of the strands, this construct has a high FRET value and we often use it to check the alignment of our microscopes for FRET measurements.

Figure. 6.9 shows the fluorescent signal in donor and acceptor channel for OligoAD, the signal in acceptor channel is definitely stronger and likely to be near 1. This made me believe that Cy3B-Cy5 is not a good FRET pair. In order to check this I did solution FRET measurements on the DIS system to see whether I get similar results to the FRET-TIRF measurements. These experiments are described in chapter 7.

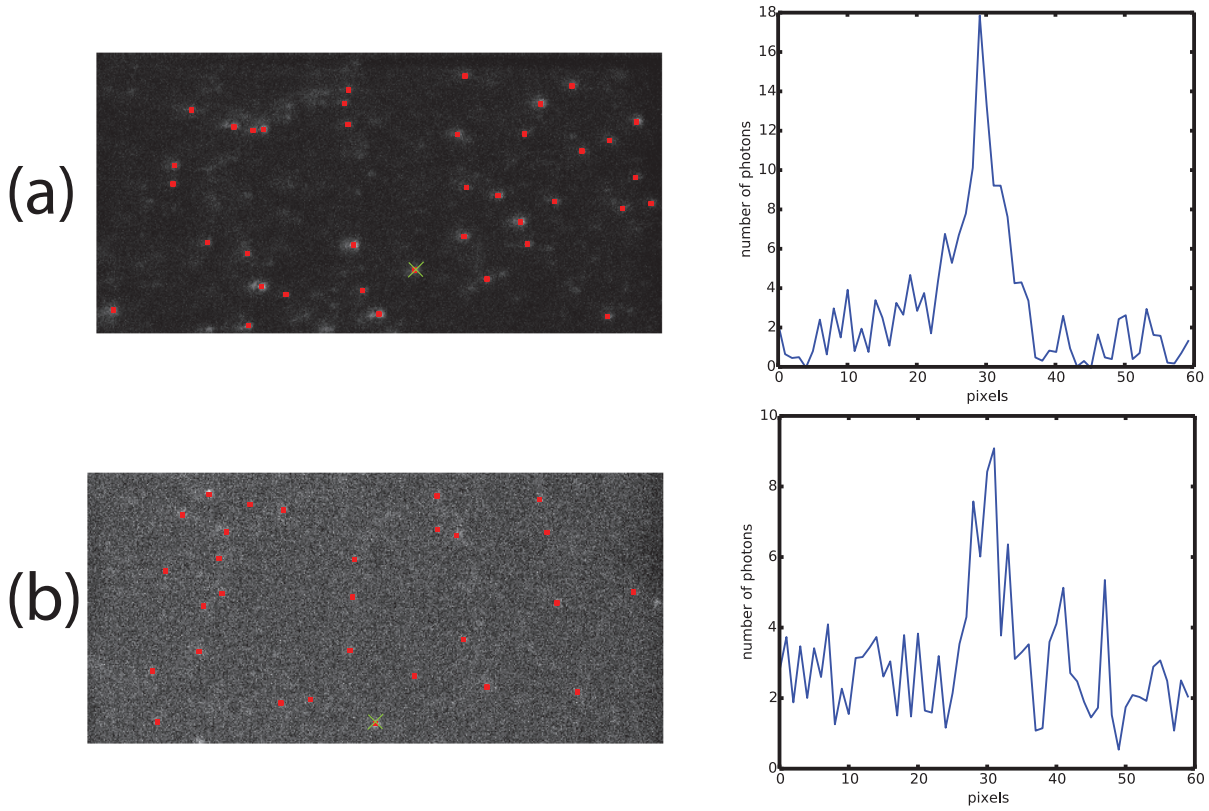

Figure 6.9. Image for DIS1Cy3B-DIS2Cy5 molecules in the (a) donor channel and (b) acceptor channel. Features are labeled with red dots, and the intensity profiles are shown on the right side of images.

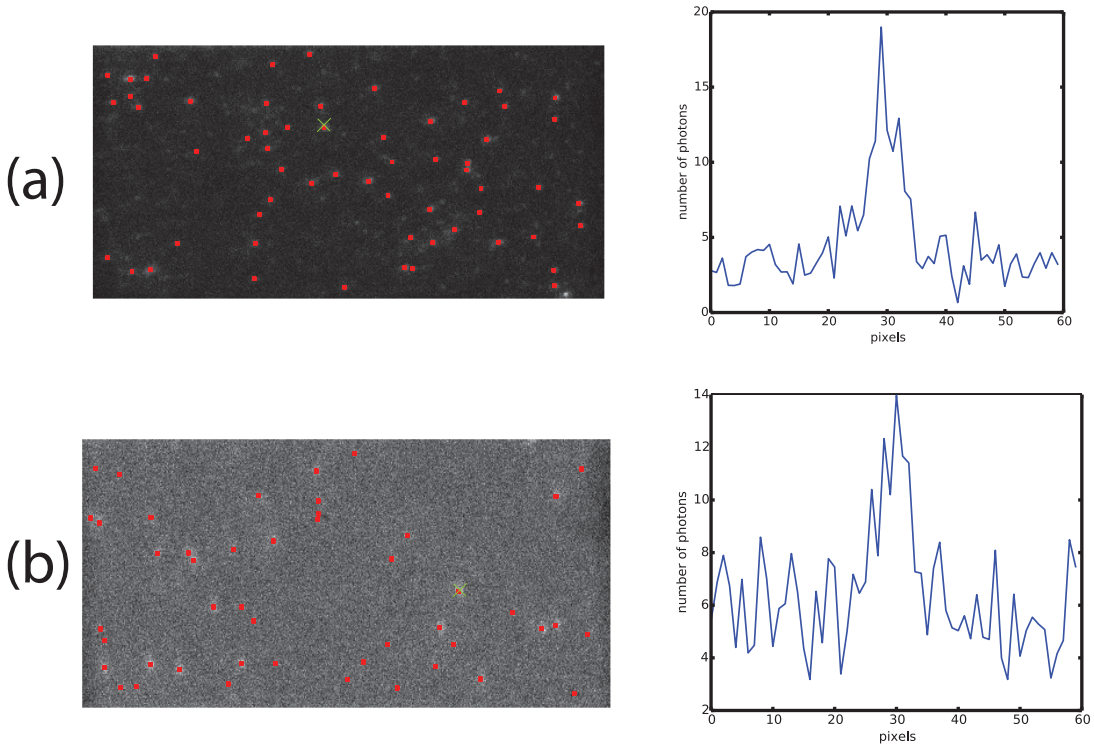

Figure 6.10. Image for OligoAD (DNA duplex labeled with Cy3-Cy5) moleclues in the (a) donor channel and (b) acceptor channel. Features are labeled with red dots, and the intensity profiles are shown on the right side of images.

For the FRET-TIRF experiments all the analysis described in this section are qualitative, in future for better evaluation of the efficiency of samples and setup, it is important to develop or use a software package for FRET calculations. There are a few packages that are available to use for single molecule FRET analysis, for example iSMS [80] a package written in Matlab for TIRF-FRET analysis, and twotone [49] analysis software provided by Kapanidis group at Oxford university.

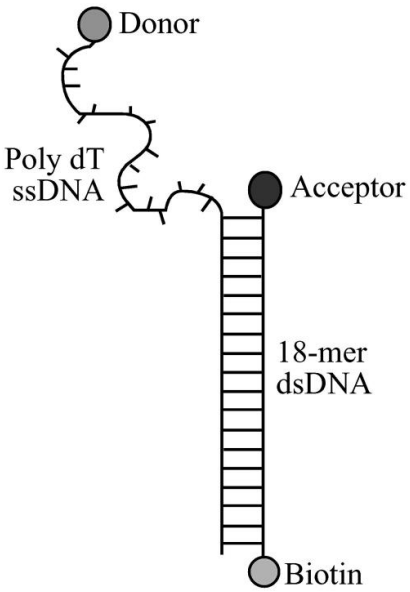

Figure 6.11. 18bp double stranded DNA with a dT_N tail with 13 bases labeled with Cy3 at the $3'$ end of the tail and Cy5 on the $5'$ terminal of the dsDNA and biotinylated on the $3'$ end [71].

CHAPTER 7

DIS SOLUTION FRET : CY3B-CY5 PAIR *VS.* CY3-CY5 PAIR

In this section I'm reporting on different solution FRET measurements I did on DIS KC and duplex complex labeled with Cy3B-Cy5 or Cy3-Cy5. These measurements are performed in different salt conditions. The main purpose of this section is to investigate whether the low FRET observed in FRET-TIRF measurements are due to the samples.

Figure. 7.1(a-c) shows proximity ratio histograms for 50 pM DIS kissing complex (with 1.2x excess of DIS2-Cy5) prepared in 20 mM Tris (pH 7.8), 5mM $MgCl_2$ and 50 mM, 100 mM and 200 mM NaCl. All these samples show a very low FRET of about 0.2, although we would expect to have larger FRET of about 0.4 for KC. For DIS duplex a large FRET efficiency of about 1 is expected. A sample of duplex DIS was prepared by mixing the DIS hairpins in 20 mM Tris (pH 7.8) and 200 mM of NaCl with no $MgCl_2$ at final concentration of 2 μM, incubating it for 30 minutes at 55 °C and finally diluting it to 100 pM concentration. The proximity ratio histogram for duplex DIS, shown in Figure. 7.1(d), is very similar to DIS KC and doesn't show any population at high FRET efficiencies. To better investigate the formation of duplex, I prepared duplex DIS at different conditions and with different Mg^{+2} concentrations. Figure. 7.2 shows proximity ratio histograms for these different trials. Still neither of them shows high FRET efficiency. My hypothesis is that Cy3B-Cy5 is not a good FRET pair and this is probably because of the large difference in their quantum yields.

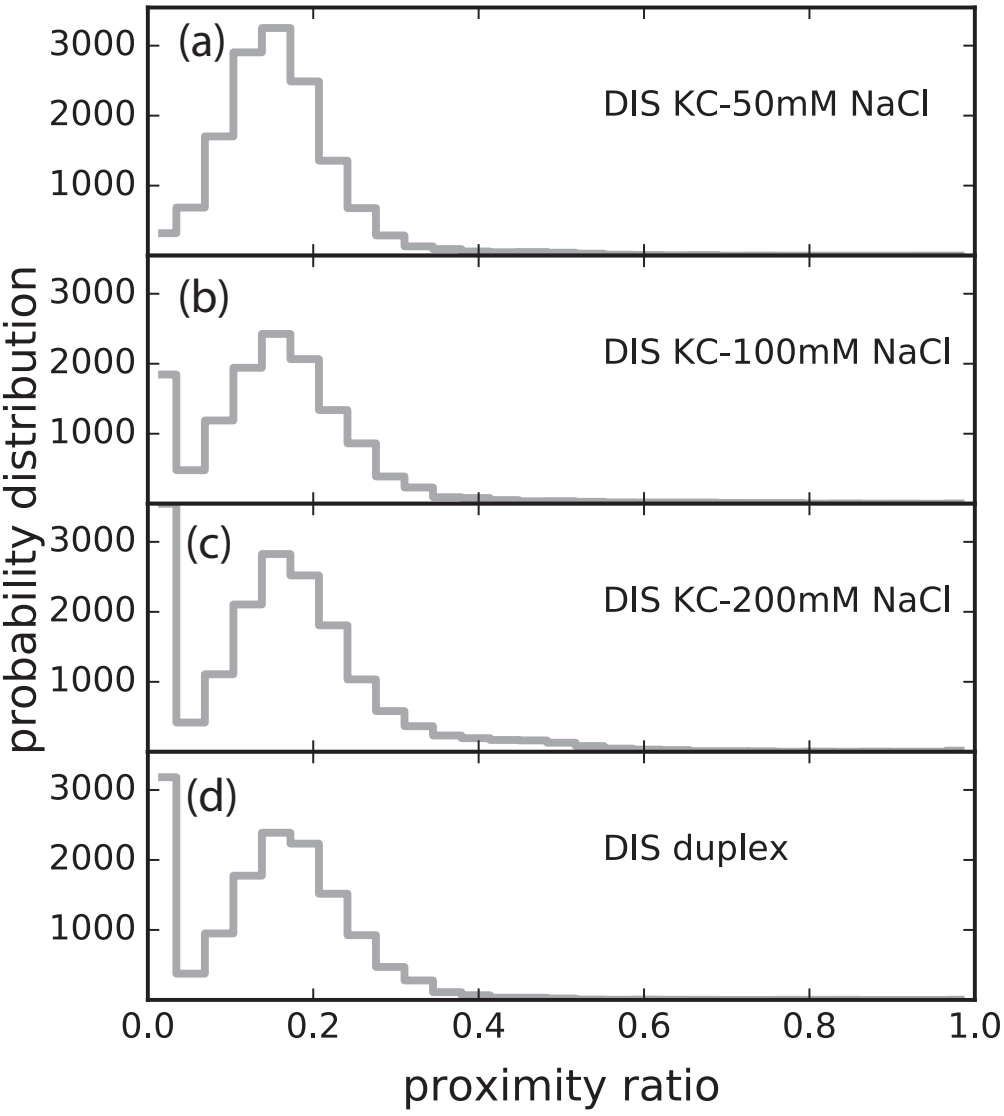

Figure 7.1. Proximity ratio histograms of DIS kissing complex prepared in 20 mM Tris (pH 7.8), 5mM $MgCl_2$ with (a) 50 mM NaCl (b) 100 mM NaCl (c) 200 mM NaCl (d) DIS duplex at 200 mM NaCl.

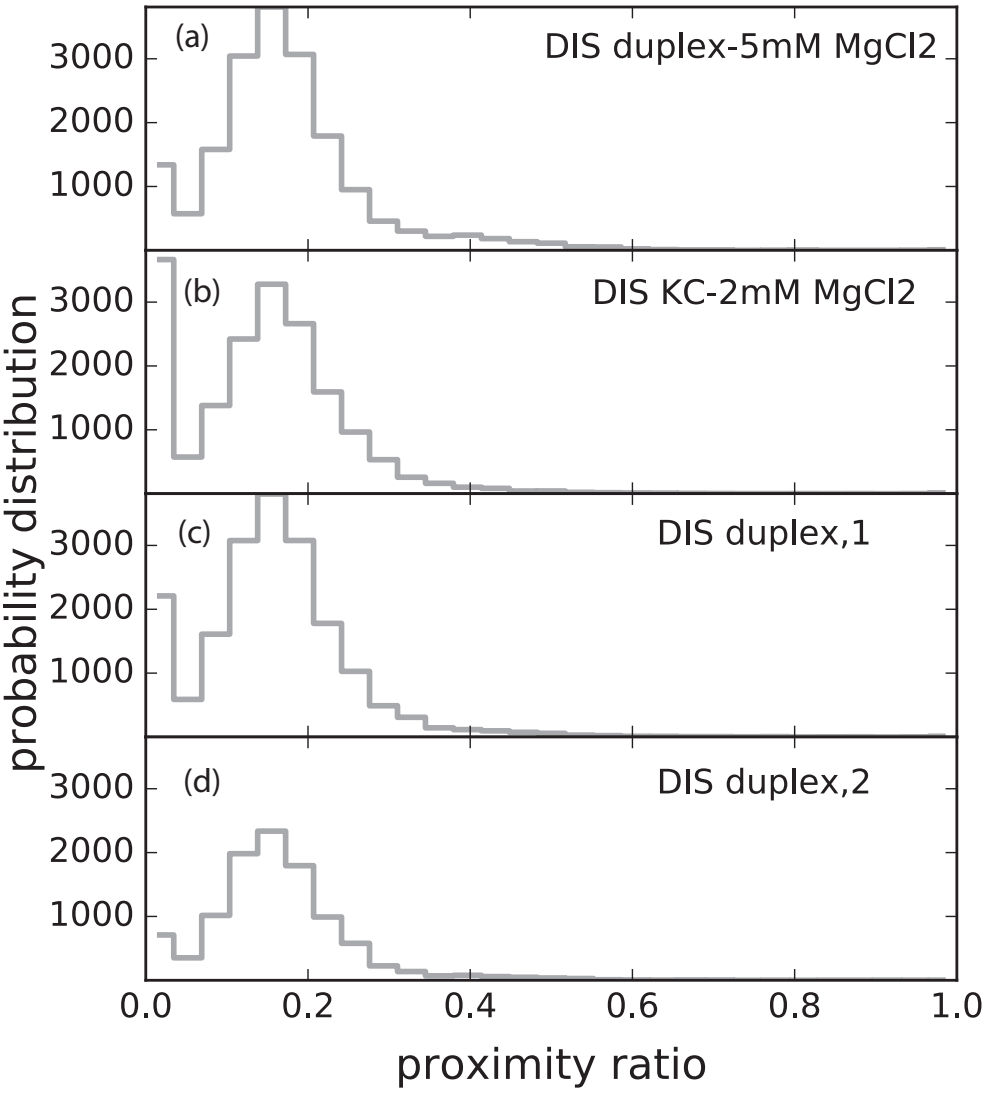

Figure 7.2. Proximity ratio histograms of DIS duplex prepared by mixing DIS1Cy3B, DIS2Atto647N hairpins and incubating them at 55 °C in 20 mM Tris, 200 mM NaCl with (a) 5 mM $MgCl_2$ (b) 2 mM $MgCl_2$ (c) DIS duplex prepared in PCR machine (d) DIS duplex prepared by mixing DIS strands before forming the hairpins and incubating them at 55 °C.

We also have some older DIS strands in our lab labeled with Cy3 and Cy5; these strands have 24 bases and the mutation in their loop is different from the strands we used for TIRF measurements. I tested my hypothesis about the inefficiency of Cy3B-Cy5 pair by preparing a duplex DIS labeled with Cy3 and Cy5 and measuring FRET for it. The sequence for DIS24(GA)Cy3 and DIS24(UC)Cy5 and the corresponding proximity ratio histogram for the duplex formed from them is shown in Figure. 7.3(a,b). This histogram shows an a population of FRET near 1 consistent with duplex formation. I believe this observation is evidence for Cy3B-Cy5 not being a good FRET pair. To confirm our speculation, we have to get DIS strands labeled with Cy3 and Atto647N and repeat the FRET measurements with Cy3-Cy5 pair and Cy3B-Atto647N pair.

I used fluorescence lifetime measurements to measure FRET for DIS labeled with Cy3B-Atto647N in presence and absence of NCp7. In presence of NCp7 we expect formation of duplex DIS which has a high FRET efficiency. The fluorescence lifetime decay curves, shown in Figure. 7.4, for DIS labeled with Cy3B-Atto647N shows a larger decrease in fluorescence lifetime in presence of NCp7, this indicates formation of duplex DIS.

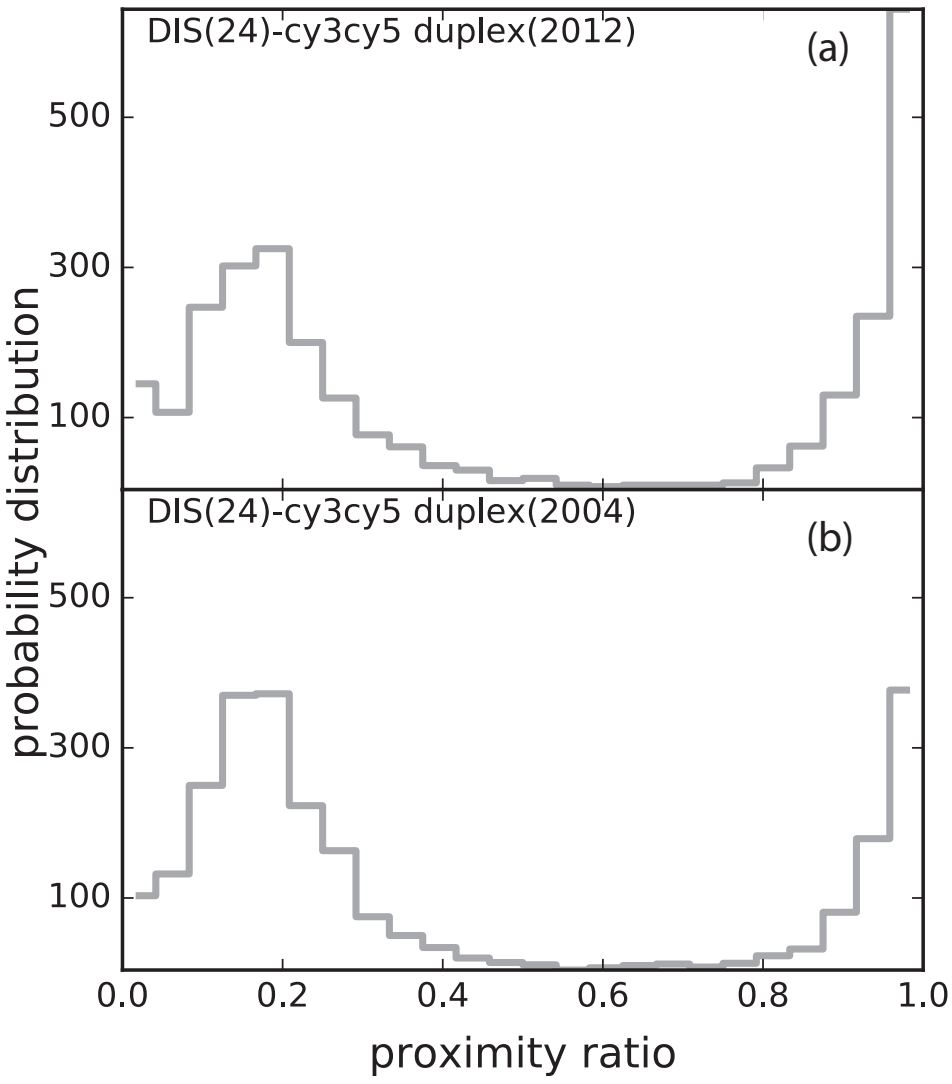

Figure 7.3. Proximity ratio histograms for DIS24(GA)-DIS24(UC) duplex labeled with Cy3 and Cy5 prepared at 20 mM Tris (pH 7.8), 150 mM NaCl and 5 mM $MgCl_2$ (a) newer samples from 2012 (b) older samples from 2004

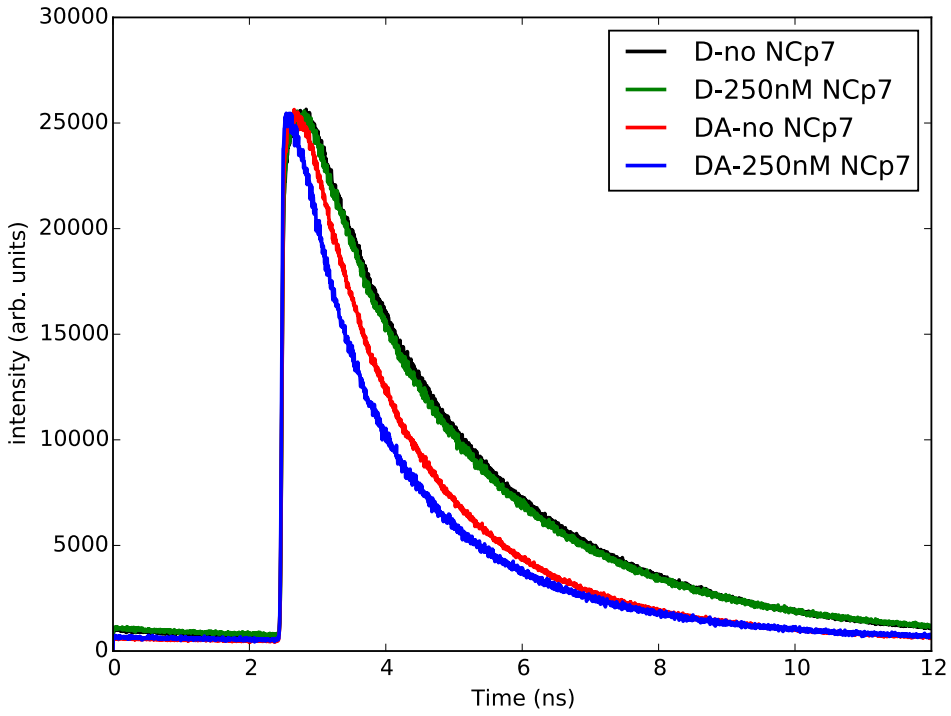

Figure 7.4. Fluorescence lifetime decay curves for DIS labeled with Cy3B only and Cy3B-Atto647N in presence and absence of NCp7

APPENDIX A

ELECTROPHORETIC MOBILITY SHIFT ASSAY PROTOCOL

The DNA-protein or RNA-protein complexes can be separated from unbound DNA or RNA by electrophoresis through a nondenaturing polyacrylamide gel. Since formation of hairpins is Mg^{2+} dependant, these gels have been prepared in TBM buffer (Tris-borate, $MgCl_2$), which has Mg^{2+} in it.

Procedure:

1) Prepare a 15% polyacrylamide gel

Resolving gel	
ddH_2O	4.65 mL
polyacrylamide (30%) (BioRad)	5 mL
TBM* buffer (5x)	2 mL
Glycerol (2.5%)	1.25 mL of 20% glycerol
APS*** (10%)	100 μL
TEMED(BioRad)	8 μL

Stacking gel	
ddH_2O	3.35 mL
polyacrylamide(30%) (BioRad)	625 μL
TBM* buffer (5x)	1mL
APS*** (10%)	100 μL
TEMED(BioRad)	8 μL

2) Prerun the gel at 10 mA in 1x TBM buffer for 30min.

3) Load the gel with 15-20 μL of sample. Sample can be a mixture of DNA or RNA with protein and the loading dye**.

4) Run the gel at 10mA while keeping it on ice(4°C) for the desired time.

5) Take the gel out and put it in 1x TBM buffer with one drop of EtBr in it for staining.

* 5x TBM buffer: 54 g Tris base + 27.5 g boric acid in 1L ddH_2O + 10 mL Mg^{2+} (500 mM) (1x TBM buffer is 90 mM Tris-Borate, 1 mM Mg^{2+} .)

**loading dye 6X: Promega G190A

***APS (Ammonium Persulfate) 10% (1 g APS (BioRad 161-0700) in 10 mL ddH_2O) store at 4°C.

Note: TEMED should always be added at the end.

For DNA samples or RNA oligos which are not in hairpin form the regular Tris buffer can be used instead of TBM buffer. Also the gel does not need to be kept on ice. Here is an example for a 15% polyacrylamide gel:

15% polyacrylamide gel:

Resolving gel	
ddH_2O	5.4 mL
polyacrylamide (30%)	5 mL
resolving buffer* (5x)	2.5 mL
APS (10%)	100 μL
TEMED(BioRad)	8 μL

Stacking gel	
ddH_2O	3.1 mL
polyacrylamide (30%)	625 μL
stacking buffer**	1.25 mL
APS (10%)	100 μL
TEMED(BioRad)	8 μL

* Resolving buffer(4x): 90.75 gr Tris base in 500 mL ddH_2O, pH=8.8

** Stacking buffer(4x): 30 gr Tris in 500 mL ddH_2O, pH=6.8

APPENDIX B

MOLECULAR DYNAMICS SIMULATIONS

MD simulations used in this work are done with Louis Parrot and Peker Milas from Goldner lab. Molecular dynamics simulations were run to calculate FRET using the cpptraj module of Amber 12 [25] and the FF12SB force field. Trajectories for Cy3 and Cy5 attached to 5′ terminal G or C were extracted from 300 ns runs of the dye-labeled R1inv-R2inv or R1inv-R2inv-C kissing complex, respectively. TIP3P water was used with 22 Na^+ ions giving a concentration of about 160 mM.

NMR restraints were converted from 1bj2 PDB file to a format compatible with Amber using the NMR Restraints grid website [28, 29, 73, 72]. Four simulations of at least 300 ns each were performed using the process described in Ref. [66], one for each model with and without NMR dihedral restraints. In all simulations we observed a significant deviation in the molecular bend angle in less than 1ns during the heating phase. We believe this is an artifact of the FF12SB force field incorrectly modeling the interactions in the kissing region. However, the dye stacking and orientation behavior relative to the nearest base pair were consistent with previous work [66]. It is important to note that the MD simulations were run primarily to extract the dye trajectories, and not to gain any insight into the RNA structure or dynamics.

APPENDIX C

FRET *VS.* TWIST ANGLE FOR THE EIGHT MINIMIZED ENERGY STRUCTURES

Fig. C.1 shows FRET *vs.* twist angle for four of the eight minimized energy structures. The change in twist angle corresponding to the experimental change in FRET for structures number 4, 5, 7 and 8 is: -20°, -25°, -31°, -25°, respectively.

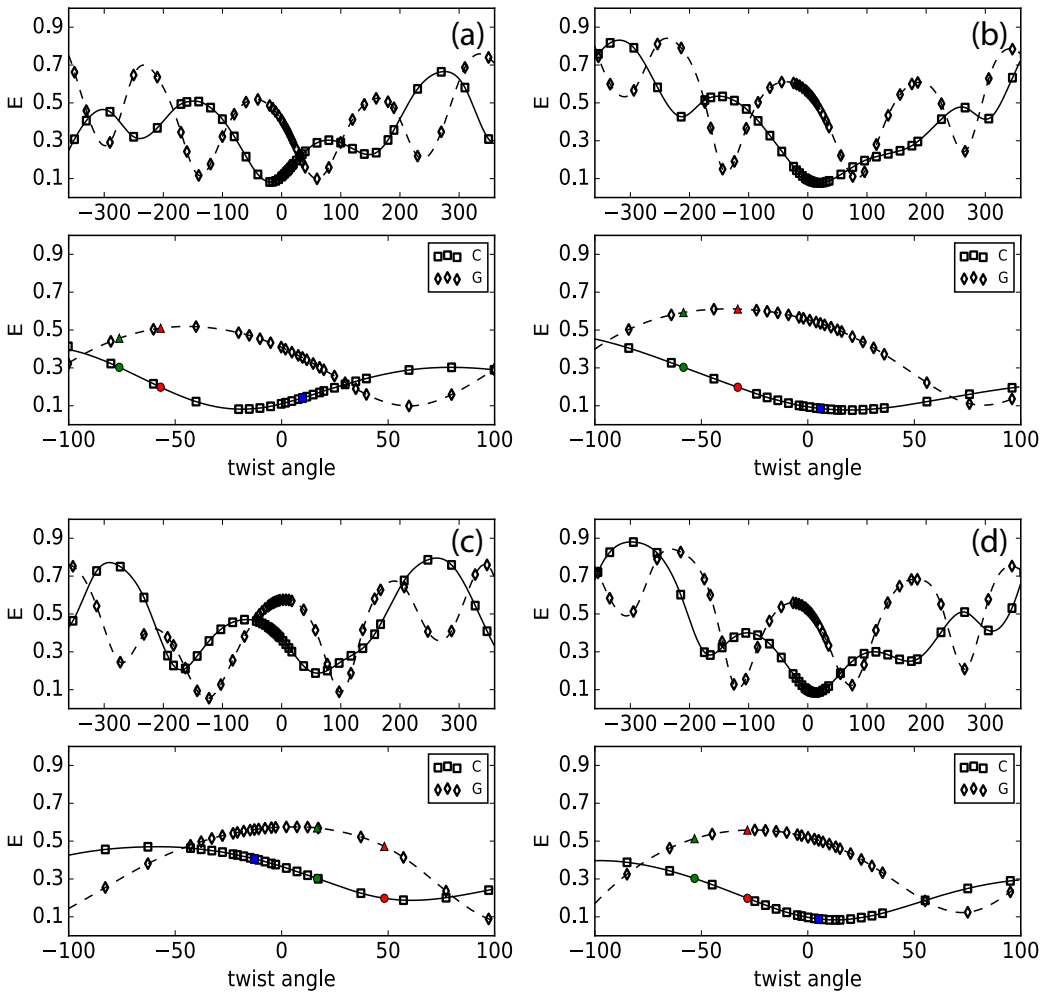

Figure C.1. Calculated FRET at different twist angles for structures (a) four, (b) five (c) seven (d) eight. Diamonds show FRET at each twist angle for 5′-G and squares for 5′-C construct. Dashed and solid lines are interpolated spline curves to the points for 5′-G and 5′-C respectively. The red circles and triangles in all panels show FRET for the unbound RNA, and the green circles and triangles show FRET for the bound RNA. The blue square represents twist angle for the initial untwisted structure.

APPENDIX D

PCD, PCA AND MV RECIPES

Recipe for 100 μM PCD (protocatechuate 3,4-Dioxygenase): Mix 50 μL KCl* (1M) + 200 μL Glycine** (500 mM, pH9)+750 μL DEPC*** =1 mL Then take 971 μL of this mix and add it to the bottle which contains PCD. Then start making 10 μL or 20 μL aliquots and store them at -80°C freezer. PCD is from Sigma-Aldrich with code of P8279.

KCL (1M)*: dissolving 2.2365 grams of KCl in 30 mL of DEPC water. Then filtering the solution and autoclaving it.

Glycine (500 mM, pH 9)**: dissolving 1.1260 grams of Glycine in 30 mL of DEPC water, then adjusting the pH to 9 using NaOH. Finally, filtering and autoclaving.

DEPC water ***: Add 1 mL of DEPC(Diethylpyrocarbonate) to 1L of ddH_2O (double-distilled water) and after mixing it place it in oven at 37°C overnight or at least for 2 hours. Then Autoclave it using the liquids cycle and let it cool down and store it in refrigerator.

Recipe for PCA (3,4-Dihydroxybenzoic acid):

Add a small tablet of NaOH to 10 mL of DEPC water. To prepare 100 mM (40x) concentration of PCA (M_w= 154.12 gr/mol) add 0.23118 gr of PCA to it (without NaOH PCA won't dissolve). Then check the pH with pH meter and set it to 9 using NaOH. Then make the volume 15 mL by adding more DEPC water. Filter it using 0.22 μm syringe filter and prepare aliquots of 50 μL or larger and store them in -20°C freezer. PCA is from Sigma-Aldrich with code of 37580-25G.

Recipe for MV (Methylviologen): To prepare a 200 mM (100x) solution of MV (M_w= 257.2 gr/mol), add 0.0514 gr MV to 1 mL DEPC water. Filter it using 0.22 μm syringe filter and prepare 10 μL aliquots and store then in -20°C freezer.

APPENDIX E

TRIS BUFFER, $MGCL_2$ AND NACL SOLUTIONS

Tris buffer (400mM, pH 7.8): Dissolve 3.152 gr of Tris (M_w= 157.6 gr/mol) in 50 mL of DEPC water. Then setting the pH with HCl or NaOH to 7.8. Taking 25 mL of the buffer and adding 25 mL of DEPC water to it, to make 200mM Tris buffer. Then filter and autoclave the buffer and store it in refreigerator.

$MgCl_2$ solution (100 mM): Dissolve 1.0165 gr $MgCl_2$ (M_w= 203.3 gr/mol) in 50 mL DEPC water. Filter and autoclave it and store it in refrigerator.

NaCl solution (1 M): Dissolve 2.922 gr NaCl (M_w= 58.44 gr/mol) in 50 mL DEPC water. Filter and autoclave it and store it in refrigerator.

BIBLIOGRAPHY

[1] Aduri, Raviprasad, Briggs, Katharine T, Gorelick, Robert J, and Marino, John P. Molecular determinants of HIV-1 NCp7 chaperone activity in maturation of the HIV-1 dimerization initiation site. *Nucleic acids research 41*, 4 (Feb. 2013), 2565–80.

[2] Aitken, Colin Echeverría, Marshall, R Andrew, and Puglisi, Joseph D. An oxygen scavenging system for improvement of dye stability in single-molecule fluorescence experiments. *Biophysical journal 94*, 5 (Mar. 2008), 1826–35.

[3] Anderson, BJ, Larkin, Chris, Guja, Kip, and Schildbach, JF. Using Fluorophore-Labeled Oligonucleotides to Measure Affinities of ProteinDNA Interactions. *Methods in enzymology 6879*, 08 (2008).

[4] Axelrod, Daniel. Total Internal Reflection Fluorescence Microscopy in Cell Biology. *Traffic 2*, 11 (Nov. 2001), 764–774.

[5] Baba, Seiki, Takahashi, Ken-ichi, Noguchi, Satoko, Takaku, Hiroshi, Koyanagi, Yoshio, Yamamoto, Naoki, and Kawai, Gota. Solution RNA structures of the HIV-1 dimerization initiation site in the kissing-loop and extended-duplex dimers. *Journal of biochemistry 138*, 5 (Nov. 2005), 583–92.

[6] Banner, D. W., Kokkinidis, M., and Tsernoglou, D. Structure of the co1e1 rop protein at 1.7 a resolution. *Journal of Molecular Biology 196*, 3 (1987), 657–675.

[7] Banner, DW, Kokkinidis, M, and Tsernoglou, D. structure of ColE1 ROP Protein at 1.7A Resolution. *Journal of molecular biology* (1987), 657–675.

[8] Bartel, David P. MicroRNAs: target recognition and regulatory functions. *Cell 136*, 2 (Jan. 2009), 215–33.

[9] Becker, W., Bergmann, A., Hink, M. A., Konig, K., Benndorf, K., and Biskup, C. Fluorescence lifetime imaging by time-correlated single-photon counting. *Microscopy Research and Technique 63*, 1 (2004), 58–66.

[10] Berezin, Mikhail Y, and Achilefu, Samuel. Fluorescence lifetime measurements and biological imaging. *Chemical reviews 110*, 5 (May 2010), 2641–84.

[11] Berkhout, Ben, Gorelick, Robert, Summers, Michael F, Mély, Yves, and Darlix, Jean-Luc. 6Th International Symposium on Retroviral Nucleocapsid. *Retrovirology 5* (Jan. 2008), 21.

[12] Bernacchi, Serena, Ennifar, Eric, Tóth, Katalin, Walter, Philippe, Langowski, Jörg, and Dumas, Philippe. Mechanism of hairpin-duplex conversion for the HIV-1 dimerization initiation site. *The Journal of biological chemistry 280*, 48 (Dec. 2005), 40112–21.

[13] Bernacchi, Serena, Freisz, Séverine, Maechling, Clarisse, Spiess, Bernard, Marquet, Roland, Dumas, Philippe, and Ennifar, Eric. Aminoglycoside binding to the HIV-1 RNA dimerization initiation site: thermodynamics and effect on the kissing-loop to duplex conversion. *Nucleic acids research 35*, 21 (Jan. 2007), 7128–39.

[14] Best, Robert B, Merchant, Kusai a, Gopich, Irina V, Schuler, Benjamin, Bax, Ad, and Eaton, William a. Effect of flexibility and cis residues in single-molecule FRET studies of polyproline. *Proceedings of the National Academy of Sciences of the United States of America 104*, 48 (Nov. 2007), 18964–9.

[15] Borst, Jan Willem, and Visser, Antonie J W G. Fluorescence lifetime imaging microscopy in life sciences. *Measurement Science and Technology 21*, 10 (2010), 102002.

[16] Brantl, Sabine. Antisense RNAs in plasmids : control of replication and maintenance. *Plasmid 48* (2002), 165–173.

[17] Brunel, Christine, Marquet, Roland, Romby, Pascale, and Ehresmann, Chantal. RNA loop-loop interactions as dynamic functional motifs. *Biochimie 84*, 9 (Sept. 2002), 925–44.

[18] Cao, Song, and Chen, Shi-Jie. Predicting kissing interactions in microRNA-target complex and assessment of microRNA activity. *Nucleic acids research 40*, 10 (May 2012), 4681–90.

[19] Castagnoli, L, Scarpa, M, Kokkinidis, M, Banner, D W, Tsernoglou, D, and Cesareni, G. Genetic and structural analysis of the ColE 1 Rop (Rom) protein. *The EMBO Journal 8*, 2 (1989), 621–629.

[20] Chandradoss, Stanley D, Haagsma, Anna C, Lee, Young Kwang, Hwang, Jae-Ho, Nam, Jwa-Min, and Joo, Chirlmin. Surface Passivation for Single-molecule Protein Studies. e50549.

[21] Clegg, R. M. Fluorescence resonance energy-transfer and nucleic-acids. *Methods in Enzymology 211* (1992), 353–388.

[22] Clever, J L, Wong, M L, and Parslow, T G. Requirements for kissing-loop-mediated dimerization of human immunodeficiency virus Requirements for Kissing-Loop-Mediated Dimerization of Human Immunodeficiency Virus RNA. *J. Virol 70*, 9 (1996).

[23] Comolli, L. R., Pelton, J. G., and Tinoco, I. Mapping of a protein-rna kissing hairpin interface: Rom and tar-tar. *Nucleic Acids Research 26*, 20 (1998), 4688–4695.

[24] Cristofari, Gaël, and Darlix, Jean-Luc. The ubiquitous nature of RNA chaperone proteins. *Progress in nucleic acid research and molecular biology 72* (Jan. 2002), 223–68.

[25] D.A. Case, T. A. Darden T. E. Cheatham III C. L. Simmerling J. Wang R. E. Duke R., Luo, R. C. Walker W. Zhang K. M. Merz B. Roberts B. Wang S. Hayik A. Roitberg, G. Seabra, I. Kolossváry K. F. Wong F. Paesani J. Vanicek X. Wu S. R. Brozell T., Steinbrecher, H. Gohlke Q. Cai X. Ye J. Wang M. J Hsieh G. Cui D. R. Roe D. H., Mathews, M. G. Seetin C. Sagui V. Babin T. Luchko S. Gusarov A. Kovalenko, , and Kollman, P. A. Amber 12, 2012.

[26] Darlix, J L, Gabus, C, Nugeyre, M T, Clavel, F, and Barré-Sinoussi, F. Cis elements and trans-acting factors involved in the RNA dimerization of the human immunodeficiency virus HIV-1. *Journal of molecular biology 216*, 3 (Dec. 1990), 689–99.

[27] Darlix, Jean-Luc, Godet, Julien, Ivanyi-Nagy, Roland, Fossé, Philippe, Mauffret, Olivier, and Mély, Yves. Flexible nature and specific functions of the HIV-1 nucleocapsid protein. *Journal of molecular biology 410*, 4 (July 2011), 565–81.

[28] Doreleijers, Jurgen F., Mading, Steve, Maziuk, Dimitri, Sojourner, Kassandra, Yin, Lei, Zhu, Jun, Markley, John L., and Ulrich, Eldon L. BioMagResBank database with sets of experimental NMR constraints corresponding to the structures of over 1400 biomolecules deposited in the Protein Data Bank. *Journal of Biomolecular NMR 26*, 2 (2003), 139–146.

[29] Doreleijers, Jurgen F., Nederveen, Aart J., Vranken, Wim, Lin, Jundong, Bonvin, Alexandre M J J, Kaptein, Robert, Markley, John L., and Ulrich, Eldon L. BioMagResBank databases DOCR and FRED containing converted and filtered sets of experimental NMR restraints and coordinates from over 500 protein PDB structures. *Journal of Biomolecular NMR 32*, 1 (2005), 1–12.

[30] Eguchi, Y, Itoh, Tateo, and Tomizawa, JI. Antisense RNA. *Annual review of biochemistry* (1991).

[31] Eguchi, Y., and Tomizawa, J. Complexes formed by complementary rna stem-loops - their formations, structures and interaction with cole1 rom protein. *Journal of Molecular Biology 220*, 4 (1991), 831–842.

[32] Eguchi, Yutaka, and Tomizawa, Jun-ichi. Complex formed by complemetary RNA stem-loops and its stabilization by a protein: Function of ColE1 Rom protein. *Cell 60*, 2 (Jan. 1990), 199–209.

[33] Eguchi, Yutaka, and Tomizawa, Jun-ichi. Complexes formed by complementary RNA stem-loops. *Journal of Molecular Biology 220*, 4 (Aug. 1991), 831–842.

[34] Elson, Elliot L. Fluorescence correlation spectroscopy: past, present, future. *Biophysical journal 101*, 12 (Dec. 2011), 2855–70.

[35] Ennifar, E, Walter, P, Ehresmann, B, Ehresmann, C, and Dumas, P. Crystal structures of coaxially stacked kissing complexes of the HIV-1 RNA dimerization initiation site. *Nature structural biology 8*, 12 (Dec. 2001), 1064–8.

[36] Ennifar, E, Yusupov, M, Walter, P, Marquet, R, Ehresmann, B, Ehresmann, C, and Dumas, P. The crystal structure of the dimerization initiation site of genomic HIV-1 RNA reveals an extended duplex with two adenine bulges. *Structure 7*, 11 (Nov. 1999), 1439–1449.

[37] Ennifar, Eric, Paillart, Jean-Christophe, Bernacchi, Serena, Walter, Philippe, Pale, Patrick, Decout, Jean-Luc, Marquet, Roland, and Dumas, Philippe. A structure-based approach for targeting the HIV-1 genomic RNA dimerization initiation site. *Biochimie 89*, 10 (Oct. 2007), 1195–203.

[38] Ennifar, Eric, Paillart, Jean-Christophe, Bodlenner, Anne, Walter, Philippe, Weibel, Jean-Marc, Aubertin, Anne-Marie, Pale, Patrick, Dumas, Philippe, and Marquet, Roland. Targeting the dimerization initiation site of HIV-1 RNA with aminoglycosides: from crystal to cell. *Nucleic acids research 34*, 8 (Jan. 2006), 2328–39.

[39] Ennifar, Eric, Paillart, Jean-Christophe, Marquet, Roland, Ehresmann, Bernard, Ehresmann, Chantal, Dumas, Philippe, and Walter, Philippe. HIV-1 RNA dimerization initiation site is structurally similar to the ribosomal A site and binds aminoglycoside antibiotics. *The Journal of biological chemistry 278*, 4 (Jan. 2003), 2723–30.

[40] Gamari, Benjamin D., Zhang, Dianwen, Buckman, Richard E, Milas, Peker, Denker, John S., Chen, Hui, Hongmin, Li, and Goldner, Lori S. Inexpensive electronics and software for photon statistics and corerlation spectroscopy. *American Journal of Physics* (2013).

[41] Girard, F, and Barbault, F. Dimer initiation sequence of HIV-1 Lai Genomic RNA: NMR solution structure of the extende duplex. *... Structure and ...* (1999).

[42] Gopich, Irina V., and Szabo, Attila. Theory of single-molecule fret efficiency histograms. In *Single-molecule biophysics: Experiment and theory*, T Komatsuzaki, M Kawakami, S Takahashi, H Yang, and RJ Silbey, Eds., vol. 146 of *Advances in Chemical Physics*. 2012, pp. 245–297.

[43] Gregorian, R S, and Crothers, D M. Determinants of RNA hairpin loop-loop complex stability. *Journal of molecular biology 248*, 5 (May 1995), 968–84.

[44] Ha, Taekjip, Rasnik, Ivan, Cheng, Wei, Babcock, Hazen P, Gauss, George H, Lohman, Timothy M, and Chu, Steven. Initiation and re-initiation of DNA unwinding by the Escherichia coli Rep helicase. *Nature 419*, 6907 (Oct. 2002), 638–41.

[45] Ha, Taekjip, and Selvin, Paul R. The New Era of Biology In Singulo. 1–36.

[46] Hannon, Gregory J. RNA interference. *Nature 418* (2002), 24–26.

[47] Hess, Samuel T, and Webb, Watt W. Focal volume optics and experimental artifacts in confocal fluorescence correlation spectroscopy. *Biophysical journal 83*, 4 (Oct. 2002), 2300–17.

[48] Hoefling, Martin, Lima, Nicola, Haenni, Dominik, Seidel, Claus A. M., Schuler, Benjamin, and Grubmueller, Helmut. Structural heterogeneity and quantitative fret efficiency distributions of polyprolines through a hybrid atomistic simulation and monte carlo approach. *PLOS One 6*, 5 (2011), e19791.

[49] Holden, Seamus J., Uphoff, Stephan, Hohlbein, Johannes, Yadin, David, Le Reste, Ludovic, Britton, Oliver J., and Kapanidis, Achillefs N. Defining the limits of single-molecule FRET resolution in TIRF microscopy. *Biophysical Journal 99*, 9 (2010), 3102–3111.

[50] Iqbal, A., Arslan, S., Okumus, B., Wilson, T. J., Giraud, G., Norman, D. G., Ha, T., and Lilley, D. M. J. Orientation dependence in fluorescent energy transfer between cy3 and cy5 terminally attached to double-stranded nuclelic acids. *Proceedings of the National Academy of Sciences of the United States of America 105*, 32 (2008), 11176–11181.

[51] Iqbal, A., Wang, L., Thompson, K. C., Lilley, D. M. J., and Norman, D. G. The structure of cyanine 5 terminally attached to double-stranded dna: Implications for fret studies. *Biochemistry 47*, 30 (2008), 7857–7862.

[52] Kalinin, Stanislav, Sisamakis, Evangelos, Magennis, Steven W., Felekyan, Suren, and Seidel, Claus A. M. On the origin of broadening of single-molecule fret efficiency distributions beyond shot noise limits. *Journal of Physical Chemistry B 114*, 18 (MAY 13 2010), 6197–6206.

[53] KIRCHNER, R. Secondary structure Dimorphism and interconversion between hairpin and duplex form of oligoribonucleotides. *Antisense & nucleic acid drug development and Nucleic Acid ...* (1998).

[54] L Novotny, B Hecht. *Principles of Nano-Optics*. Cambridge University Press, 2006.

[55] Lakowicz, Joseph R. *Principles of Fluorescence Spectroscopy*, vol. Second. Kluwer Academic/Plenum Publishers, New York.

[56] Laughrea, M, and Jetté, L. Kissing-loop model of HIV-1 genome dimerization: HIV-1 RNAs can assume alternative dimeric forms, and all sequences upstream or downstream of hairpin 248-271 are dispensable for dimer formation. *Biochemistry 35*, 5 (Feb. 1996), 1589–98.

[57] Laughrea, Michael, and Jettc, Louis. A 19-Nucleotide Sequence Upstream of the 5 Major Splice Donor Is Part of the Dimerization Domain of Human Immunodeficiency Virus 1 Genomic RNAt $$. *Biochemistry*, 1993 (1994), 13464–13474.

[58] Lavery, R, Moakher, M, Maddocks, J H, Petkeviciute, D, and Zakrzewska, K. Conformational analysis of nucleic acids revisited: Curves+. *Nucleic acids research 37*, 17 (Sept. 2009), 5917–29.

[59] Lee, Anna J, and Crothers, Donald M. The solution structure of an RNA looploop complex: the ColE1 inverted loop sequence. *Structure 6*, 8 (Aug. 1998), 993–1007.

[60] Lichtman, Jeff W, and Conchello, José-Angel. Fluorescence microscopy. *Nature methods 2*, 12 (dec 2005), 910–9.

[61] Marino, J P, Gregorian, R S, Csankovszki, G, and Crothers, D M. Bent helix formation between RNA hairpins with complementary loops. *Science (New York, N.Y.) 268*, 5216 (June 1995), 1448–54.

[62] Marquet, Roland, Baudin, Florence, Gabus, Caroline, Darlixl, Jean-luc, Mougel, Marylene, Ehresmann, Chantal, Ehresmann, Bernard, Cedex, Strasbourg, Normale, Ecole, Lyon, Superieure De, and Cedex, Lyon. Dimerization of human immunodeficiency virus (type 1) RNA : stimulation by cations and possible mechanism. *Nucleic acids research 19*, 9 (1991).

[63] Marquet, Roland, Paillart, Jean-christophe, Skripkin, Eugene, and Ehresmann, Chantal. Dimerization of human immunodeficiency virus type 1 RNA involves sequences located upstream of the splice donor site. *Nucleic Acids Research 22*, 2 (1994), 145–151.

[64] Masukata, Hisao, and Tomizawa, Jun-ichi. Control of primer formation for ColE1 plasmid replication: Conformational change of the primer transcript. *Cell 44*, 1 (Jan. 1986), 125–136.

[65] Mihailescu, Mihaela-Rita, and Marino, John P. A proton-coupled dynamic conformational switch in the HIV-1 dimerization initiation site kissing complex. *Proceedings of the National Academy of Sciences of the United States of America 101*, 5 (Feb. 2004), 1189–94.

[66] Milas, Peker, Gamari, Ben D, Parrot, Louis, Krueger, Brent P, Rahmanseresht, Sheema, Moore, James, and Goldner, Lori S. Indocyanine Dyes Approach Free Rotation at the 3' Terminus of A-RNA: A Comparison with the 5' Terminus and Consequences for Fluorescence Resonance Energy Transfer. *The journal of physical chemistry. B 117*, 29 (July 2013), 8649–58.

[67] Mujeeb, Anwer, Clever, Jared L., Billeci, Todd M., James, Thomas L., and Parslow, Tristram G. Structure of the dimer a initiation complex of HIV-1 genomic RNA. *Nature Structural Biology 5*, 6 (June 1998), 432–436.

[68] Mundigala, Hansini, Michaux, Jonathan B, Feig, Andrew L, Ennifar, Eric, and Rueda, David. HIV-1 DIS stem loop forms an obligatory bent kissing intermediate in the dimerization pathway . *Nucleic Acids Research 1* (2014), 1–9.

[69] Muriaux, Delphine, Fosse, Philippe, Paoletti, Jacques, Cnrs, U R A, Gusta, Institut, Roussy, V, and Desmoulins, Camille. A Kissing Complex Together with a Stable Dimer Is Involved in the HIV-1 Lai RNA Dimerization Process in Vitro . *Biochemistry*, 1995 (1996), 5075–5082.

[70] Muriaux, Delphine, Rocquigny, Hugues De, Roques, Bernard-pierre, and Paoletti, Jacques. Molecular Genetics : NCp7 Activates HIV-1 Lai RNA Dimerization by Converting a Transient Loop-Loop Complex into a Stable Dimer NCp7 Activates HIV-1 Lai RNA Dimerization by Converting a Transient Loop-Loop Complex into a Stable Dimer *. *J Biol Chem.* (1996).

[71] Murphy, M. C., Rasnik, I., Cheng, W., Lohman, T. M., and Ha, T. J. Probing single-stranded dna conformational flexibility using fluorescence spectroscopy. *Biophysical Journal 86*, 4 (2004), 2530–2537.

[72] Nabuurs, Sander B., Nederveen, Aart J., Vranken, Wim, Doreleijers, Jurgen F., Bonvin, Alexandre M J J, Vuister, Geerten W., Vriend, Gert, and Spronk, Christian A E M. DRESS: A Database of REfined Solution NMR Structures. *Proteins: Structure, Function and Genetics 55*, 3 (2004), 483–486.

[73] Nederveen, Aart J., Doreleijers, Jurgen F., Vranken, Wim, Miller, Zachary, Spronk, Chris A E M, Nabuurs, Sander B., G??ntert, Peter, Livny, Miron, Markley, John L., Nilges, Michael, Ulrich, Eldon L., Kaptein, Robert, and Bonvin, Alexandre M J J. RECOORD: A recalculated coordinate database of 500+ proteins from the PDB using restraints from the BioMagResBank. *Proteins: Structure, Function and Genetics 59*, 4 (2005), 662–672.

[74] Norman, D. G., Grainger, R. J., Uhrin, D., and Lilley, D. M. J. Location of cyanine-3 on double-stranded dna: Importance for fluorescence resonance energy transfer studies. *Biochemistry 39*, 21 (2000), 6317–6324.

[75] O'Connor, D.V., and Phillips, D. *Time Correlated Single Photon Counting.* 1984.

[76] Ouellet, Jonathan, Schorr, Stephanie, Iqbal, Asif, Wilson, Timothy J, and Lilley, David M J. Orientation of cyanine fluorophores terminally attached to DNA via long, flexible tethers. *Biophysical journal 101*, 5 (sep 2011), 1148–54.

[77] Paillart, J C, Marquet, R, Skripkin, E, Ehresmann, C, and Ehresmann, B. Dimerization of retroviral genomic RNAs: structural and functional implications. *Biochimie 78*, 7 (Jan. 1996), 639–53.

[78] Paillart, J C, Westhof, E, Ehresmann, C, Ehresmann, B, and Marquet, R. Non-canonical interactions in a kissing loop complex: the dimerization initiation site of HIV-1 genomic RNA. *Journal of molecular biology 270*, 1 (July 1997), 36–49.

[79] Predki, PF, Nayak, L Mike, Gottlieb, MBC, and Regan, L. Dissecting RNA protein interactions: RNA-RNA recognition by ROP. *Cell* (1995).

[80] Preus, Søren, Noer, Sofie L, Hildebrandt, Lasse L, Gudnason, Daniel, and Birkedal, Victoria. iSMS: single-molecule FRET microscopy software. *Nature methods 12*, 7 (jul 2015), 593–4.

[81] Rasnik, I., Myong, S., Cheng, W., Lohman, T. M., and Ha, T. Dna-binding orientation and domain conformation of the e-coli rep helicase monomer bound to a partial duplex junction: Single-molecule studies of fluorescently labeled enzymes. *Journal of Molecular Biology 336*, 2 (2004), 395–408.

[82] Rist, Manuela J, and Marino, John P. Mechanism of nucleocapsid protein catalyzed structural isomerization of the dimerization initiation site of HIV-1. *Biochemistry 41*, 50 (Dec. 2002), 14762–70.

[83] Rist, M., J. Marino. Association of an RNA kissing complex analyzed using 2-aminopurine fluorescence. *Nucleic Acids Research 29*, 11 (June 2001), 2401–2408.

[84] Roy, Rahul, Hohng, Sungchul, and Ha, Taekjip. A practical guide to single-molecule FRET. *Nature methods 5*, 6 (June 2008), 507–16.

[85] Salim, Nilshad, Lamichhane, Rajan, Zhao, Rui, Banerjee, Tuhina, Philip, Jane, Rueda, David, and Feig, Andrew L. Thermodynamic and kinetic analysis of an RNA kissing interaction and its resolution into an extended duplex. *Biophysical journal 102*, 5 (Mar. 2012), 1097–107.

[86] Sauer, Markus, Hofkens, Johan, and Enderlein, Jrg. *Handbook of Fluorescence Spectroscopy and Imaging.* Hoboken, DE: Wiley-VDH, 2010.

[87] Schwille, P. Fluorescence correlation spectroscopy and its potential for intracellular applications. *Cell biochemistry and biophysics 34*, 3 (2001), 383–408.

[88] Schwille, P, Haupts, U, Maiti, S, and Webb, W W. Molecular dynamics in living cells observed by fluorescence correlation spectroscopy with one- and two-photon excitation. *Biophysical journal 77*, 4 (1999), 2251–2265.

[89] Simons, RW, and Kleckner, N. BIOLOGICAL REGULATION BY antisense RNA in prokaryotes. *Annual review of genetics* (1988).

[90] Skripkin, E, Paillart, J C, Marquet, R, Ehresmann, B, and Ehresmann, C. Identification of the primary site of the human immunodeficiency virus type 1 RNA dimerization in vitro. *Proceedings of the National Academy of Sciences of the United States of America 91*, 11 (May 1994), 4945–9.

[91] Spiriti, Justin, Binder, Jennifer K., Levitus, Marcia, and van der Vaart, Arjan. Cy3-dna stacking interactions strongly depend on the identity of the terminal basepair. *Biophysical Journal 100*, 4 (2011), 1049–1057.

[92] Struble, E B, Ladner, J E, Brabazon, D M, and Marino, J P. New crystal structures of ColE1 Rom and variants resulting from mutation of a surface exposed residue: Implications for RNA-recognition. *Proteins 72*, 2 (Aug. 2008), 761–8.

[93] Takahashi, K I, Baba, S, and Chattopadhyay, P. Structural requirement for the two-step dimerization of human immunodeficiency virus type 1 genome . Structural requirement for the two-step dimerization of human immunodeficiency virus type 1 genome. *RNA* (2000), 96–102.

[94] Tomizawa, Jun-ichi. Control of ColEI Plasmid Replication : Binding of RNA I to RNA II and Inhibition of Primer Formation. *Cell 47* (1988), 89–97.

[95] Vogelsang, Jan, Kasper, Robert, Steinhauer, Christian, Person, Britta, Heilemann, Mike, Sauer, Markus, and Tinnefeld, Philip. A reducing and oxidizing system minimizes photobleaching and blinking of fluorescent dyes. *Angewandte Chemie-International Edition 47*, 29 (2008), 5465–5469.

[96] W, Becker. *International Review of Cytology - a Survey of Cell Biology, Vol 178*. Berlin:Springer, 2005, ch. Advanced Time-Correlated Single Photon Counting Tsechniques.

[97] W., Becker. *The bh TCSPC Handbook, 6th Edition.* 2015.

[98] Wagner, EGH, and Simons, RW. Antisense RNA Control in Bacteria, Phages, and Plasmids. *Annual Reviews in Microbiology* (1994).

[99] Widengren, Jerker, Mets, Uelo, and Rigler, Rudolf. Fluorescence correlation spectroscopy of triplet states in solution: a theoretical and experimental study. *The Journal of Physical Chemistry 99*, 36 (Sept. 1995), 13368–13379.

[100] Widengren, Jerker, and Schwille, Petra. Characterization of Photoinduced Isomerization and Back-Isomerization of the Cyanine Dye Cy5 by Fluorescence Correlation Spectroscopy. *Journal of Physical Chemistry A 104*, 27 (2000), 6416–6428.

[101] Wu, HM, and Crothers, DM. The Locus of Sequence-Directed and Protein-Induced DNA Bendings. *Nature 308*, 5959 (1984), 509–513.

[102] Yasuda, R., Masaike, T., Adachi, K., Noji, H., Itoh, H., and Kinosita, K. The atp-waiting conformation of rotating f-1-atpase revealed by single-pair fluorescence resonance energy transfer. *Proceedings of the National Academy of Sciences of the United States of America 100*, 16 (2003), 9314–9318.

[103] Zhuang, X. A Single-Molecule Study of RNA Catalysis and Folding. *Science 288*, 5473 (June 2000), 2048–2051.